Interfacial tuning

of the

Magnetoresistance

and

Magnetic Coupling

in

Metal/Oxide Thin Films

Trong Phuong Dao

DISS. ETH NO. 27366

DISS. ETH NO. 27366

Interfacial tuning of the magnetoresistance and magnetic coupling in metal / oxide thin films

A thesis submitted to attain the degree of
DOCTOR OF SCIENCES of ETH ZURICH
(Dr. sc. ETH Zurich)

presented by

Trong Phuong Dao

MSc ETH, ETH Zürich

born June 17, 1989,

citizen of Switzerland

Accepted on the recommendation of

Prof. Dr. Pietro Gambardella
Dr. Amalio Fernández-Pacheco
Prof. Dr. Manfred Fiebig

2021

Acknowledgements

This work would not have been possible without the help and support of the many people I met and worked with on the journey to finishing this thesis. First of all, I want thank Pietro Gambardella for giving me the chance to do this work in the first place, and Laura Heyderman, the close collaboration with whom ended up in three successful publications. Speaking of collaborators, I thank Zhaochu Luo and Aleš Hrabec for pushing the work we did on the lateral chiral coupling past what I ever could have imagined. The input of our co-authors was invaluable for the realization work. So I thank Marvin Müller for setting up the MOKE microscope, Manuel Baumgartner for supplementing our micromagnetic simulations with his own, and every other listed author for their help on beamtimes and more. As for the work on the epitaxial samples, Santos F. Alvarado must be lauded for his eternal patience in growing the many samples it took to ensure reproducibility.

I also want to express gratitude to the people that supported me outside of this work, as it is them that pushed me to try, continue, enjoy and finish this work. Among the first people to do so were Can and Kevin, who taught me the naive joy of science, which motivated me to start my doctoral studies. I could not have been any luckier, having Manuel, Johannes, Christoph around throughout my PhD to actually enjoy scientific discussions, as well as to plan botanic endeavors. The constant glue that kept the group together, while students and post-docs were rotated in and out, were Rina and Santos with whom I was always able

to have a good laugh. I also was given the opportunity to work with the Mesoscopic systems group. Here, I met the best people in science there could be. Ania, Nick, Susmita and Claire made every moment in the secluded place that is the PSI the best time one could imagine, making me eagerly await the next day at work and after work.

While the I had an invigorated start to my PhD, the second half of my studies was marred by failures and an onset of depression. In this phase, my family unconditionally provided me with a solid bedrock, giving me enough of a foothold to continue my work. Finally, I thank my partner Claire who has gone above and beyond anything a person in that situation could wish for. Without her presence and support, both emotionally and financially, the pressure to publish before defending and my unemployment would have made me quit without a doubt.

In the end, I count myself lucky, as I was able to work along side some of the most talented and meet some of the most incredible people, who were willing to build a support structure that carried me through my PhD.

For that I thank you all.

Declaration of Originality

I hereby declare that the following submitted thesis is original work which I alone have authored and which is written in my own words.

Title:	Interfacial tuning of the magnetoresistance and magnetic coupling in metal / oxide thin films
Author:	Dao, Trong Phuong
Supervisor:	Prof. Dr. Pietro Gambardella

With my signature I declare that I have been informed regarding normal academic citation rules and that I have read and understood the information on "Citation etiquette". The citation conventions usual to the discipline in question here have been respected.

Furthermore, I declare that I have truthfully documented all methods, data, and operational procedures and not manipulated any data. All persons who have substantially supported me in my work are identified in the acknowledgements.

The above work may be tested electronically for plagiarism.

Zürich, January 1, 2021 

List of Abbreviations

	Explanation
AHE	Anomalous Hall effect
AHMR	Anomalous Hall magnetoresistance
AMR	Anisotropic magnetoresistance
ANE	Anomalous Nernst effect
CMR	Crystalline magnetoresistance
DMI	Dzyaloshinskii-Moriya interaction
DW	Domain wall
FM	Ferromagnet
IP	In-plane
ISHE	Inverse spin Hall effect
HM	Heavy metal
MR	Magnetoresistance
MTP	Magnetothermopower
OOP	Out-of-plane
PHE	Planar Hall effect
PMA	Perpendicular magnetic anisotropy
PNE	Planar Nernst effect
RKKY	Ruderman–Kittel–Kasuya–Yosida
SAHE	Spin anomalous Hall effect
SHE	Spin Hall effect
SMR	Spin Hall magnetoresistance
SOT	Spin-orbit torques
UMR	Unidirectional magnetoresistance

Abstract

We live in a society defined by constant growth. This is exemplified by information technologies which, over a time period of only a few decades, have transformed our way of life. This rapid expansion has relied heavily on there being *"plenty of room at the bottom"*. However, as we are faced with the physical limitations of continuous miniaturization, there is a need for a new paradigm to support the growing computing power requirements of our society.

The field of spintronics provides us with several opportunities to increase the functionality of electronic devices in a sustainable way. After the discovery of the giant magnetoresistance and the tunneling magnetoresistance, which have revolutionized data storage technologies, scientists have continued to unravel novel effects and propose new applications that exploit the interplay of charge and spin degrees of freedom in electronic devices. In the last decade, a growing number of ways to measure and manipulate the magnetic state, which is used to store data, have arisen. One common thread in modern spintronics is the importance of interfaces.

In this thesis, we deal with a specific type of interface, that is both well-known, and often overlooked: ferromagnet/oxide interfaces. Specifically, we explore two main areas: firstly, magnetotransport and current-induced SOTs, and secondly, the tuning of magnetic anisotropies to induce chiral effects. To investigate the resulting physical phenomena, both parts of this work have involved the development of new fabrication techniques as well

as data acquisition and analysis methodologies.

To investigate the magnetotransport of ferromagnet/oxide interfaces, we study model systems consisting of Fe/oxide heterostructures epitaxially grown on MgO(001). Our investigation reveals that current-induced effects that are typical of heavy metal/ ferromagnet bilayers, such as spin-orbit torques and unidirectional magnetoresistance, also exist in Fe/oxide systems. In addition, the crystallinity of the Fe is imprinted onto these effects, resulting in a dependence on the orientation of the current relative to the crystal lattice. Our results show that charge-spin conversion effects do not require the presence of heavy metals as the source of spin currents. Moreover, they show that subtle differences in the morphology and chemical composition of the interfaces can produce sizable changes of the spin-orbit torques and unidirectional magnetoresistance.

Besides playing a role in the magnetotransport properties, oxide interfaces can also influence the magnetic anisotropy of ferromagnets. In this thesis, we exploit the interface-mediated anisotropy in Pt/Co/AlO_x to induce what we coined "lateral chiral coupling". This coupling requires nanoscale control over the magnetic anisotropy as it makes use of the Dzyaloshinskii–Moriya interaction, which has a very short range. For this purpose, we combined state-of-the-art fabrication techniques to develop a new process, which opened the door to the fabrication of laterally coupled in-plane and out-of-plane magnetized regions of the same layer. The effect of the lateral chiral coupling is manifold, leading to the exchange bias of adjacent in-plane and out-of-plane magnetized regions and the antiferromagnetic coupling of out-of-plane nanomagnets mediated by an in-plane spacer region. Moreover, the lateral coupling enables field-free magnetization switching using spin-orbit torques, as well as domain nucleation sites with reconfigurable energy barriers.

The results of this thesis highlight the potential of ferromag-

net/oxide interfaces to tune the magnetic ground state of single-layer ferromagnets as well as their magnetotransport properties and current-induced spin-orbit torques.

Zusammenfassung

Wir leben in einer Gesellschaft, die von ständigem Wachstum geprägt ist. Dies wird durch Informationstechnologien veranschaulicht, die, über einen Zeitraum von nur wenigen Jahrzehnten, unsere Lebensweise verändert haben. Diese rasche Expansion hat sich stark darauf verlassen, dass höhere Speicherdichten rein durch das Schrumpfen von Komponenten erreicht werden kann. Da wir jedoch mit den physischen Einschränkungen einer kontinuierlichen Miniaturisierung konfrontiert sind, ist ein neues Paradigma erforderlich, um den wachsenden Rechenleistungsbedarf unserer Gesellschaft zu decken.

Das Gebiet der Spintronik bietet uns mehrere Möglichkeiten, die Funktionalität elektronischer Geräte nachhaltig zu verbessern. Nach der Entdeckung des Riesenmagnetowiderstands und des Magnetischen Tunnelwiderstands, die die Datenspeichertechnologien revolutioniert haben, haben Wissenschaftler weiterhin neue Effekte aufgedeckt und neue Anwendungen vorgeschlagen, die das Zusammenspiel von Ladungs- und Spin-Freiheitsgraden in elektronischen Geräten ausnutzen. In den letzten zehn Jahren wurde eine wachsende Anzahl von Möglichkeiten zur Messung und Manipulation des magnetischen Zustands gefunden, die zum Speichern von Daten verwendet werden können. Ein roter Faden in der modernen Spintronik ist der Fokus auf Grenzflächen.

In dieser Arbeit beschäftigen wir uns mit einer bestimmten Grenzfläche, die sehr bekannt ist aber auch oft übersehen wird: Ferromagnet/Oxid-Grenzflächen. Insbesondere untersuchen wir

zwei Effekte: erstens Magneto-transport- und strominduzierte Spin-Bahn-Drehmomente und zweitens die Mischung magnetischer Anisotropien, um chirale Effekte zu induzieren.

Um die resultierenden physikalischen Phänomene zu untersuchen, umfassten beide Teile dieser Arbeit die Entwicklung neuer Herstellungstechniken sowie Methoden zur Datenerfassung und -analyse. Um den Magnetotransport von Ferromagnet/Oxid-Grenzflächen zu testen, untersuchen wir Modellsysteme, die aus epitaktischen MgO(001)/Fe/Oxid-Heterostrukturen bestehen. Unsere Untersuchung zeigt, dass strominduzierte Effekte wie Spin-Bahn-Drehmomente und unidirektionaler Magnetowiderstand, die in Schwermetall/Ferromagnet-Doppelschichten typisch sind, auch in Fe/Oxid-Systemen vorhanden sind. Zusätzlich wird diesen Effekten die Kristallinität des Fe eingeprägt, was zu einer Abhängigkeit von der Richtung des Stroms relativ zur Kristallstruktur führt. Unsere Ergebnisse zeigen, dass Ladung-Spin-Umwandlungseffekte nicht Schwermetalle als Quelle für Spinströme erfordern. Darüber hinaus zeigen sie, dass subtile Unterschiede in der Morphologie und chemischen Zusammensetzung der Grenzflächen beträchtliche Änderungen der Spin-Bahn-Drehmomente und des unidirektionalen Magnetowiderstands hervorrufen können.

Oxidgrenzflächen spielen nicht nur eine Rolle bei den Magnetotransporteigenschaften, sondern können auch die magnetische Anisotropie von Ferromagneten beeinflussen. In dieser Arbeit nutzen wir die Grenzflächenanisotropie in Pt/Co/AlO_x , um die laterale chirale Kopplung zu induzieren. Diese Kopplung erfordert eine lokale Kontrolle der magnetischen Anisotropie, da die Dzyaloshinskii-Moriya-Interaktion genutzt wird, die eine sehr kurze Reichweite hat. Zu diesem Zweck haben wir modernste Herstellungstechniken kombiniert, um ein neues Verfahren zu entwickeln das die Herstellung von seitlich gekoppelten magnete ermöglicht. Der Effekt der lateralen chiralen Kopplung

ist vielfältig und führt zu einem Exchange Bias benachbarter Magneten und zur antiferromagnetischen Kopplung von aneinander gereihten Nanomagneten. Darüber hinaus ermöglicht die laterale Kopplung ein feldfreies Umschalten der Magnetisierung mit Spin-Bahn-Drehmomenten.

Die Ergebnisse dieser Arbeit zeigen das Potenzial von Ferromagnet / Oxid-Grenzflächen für statische und dynamische Applikationen.

Contents

Acknowledgements 3

Abstract 9

Zusammenfassung 13

1. Introduction 21
   1.1. Motivation 21
   1.2. Background and Context 23
   1.3. Chapter Overview 30

2. Magnetic interactions 33
   2.1. Fundamental Interactions 33
      2.1.1. Exchange Interaction 33
      2.1.2. Dzyaloshinskii-Moriya Interaction 35
      2.1.3. Magnetostatic Energy 36
   2.2. Magnetic Anisotropy 37
      2.2.1. Shape anisotropy 38
      2.2.2. Magnetocrystalline Anisotropy 39
      2.2.3. Interface Anisotropy 40
   2.3. Magnetic Domains and Domain Walls 40
   2.4. External Influences 42
      2.4.1. Zeeman Energy 42
      2.4.2. Spin-orbit Torques 43
   2.5. Magnetization Dynamics 44

3. Magnetotransport 47
3.1. Magnetoresistance 47
3.1.1. Anisotropic Magnetoresistance 48
3.1.2. Planar Hall Effect 49
3.1.3. Anomalous Hall Effect 50
3.2. Crystalline Magnetoresistance 50
3.3. Interfacial Crystalline Magnetoresistance 52
3.4. Current-induced Effects 53
3.4.1. Thermoelectric Effects 53
3.4.2. Origin of Spin Currents 54
3.4.3. Spin-current-induced Effects 59

4. Measurement Technique & Data Analysis 67
4.1. Hall Bar Geometry 67
4.2. Harmonic Voltage Analysis 70
4.2.1. First Harmonic Resistance Analysis 72
4.2.2. Second Harmonic Resistance 80
4.3. Macrospin Simulations 83
4.4. Data Analysis 86
4.5. Magnetic Microscopy 88
4.5.1. X-ray Photoemission Electron Microscopy 88
4.5.2. Magnetic Force Microscopy 90
4.5.3. Wide-Field Magneto-optic Kerr Effect . . . 91

5. Sample Fabrication 93
5.1. Fabrication Methods 93
5.1.1. Film growth 93
5.1.2. Electron Beam Lithography 95

6. Magnetotransport in Epitaxial Fe Single Layers 103
6.1. Magnetoresistance and Current-induced Effects . 104
6.2. Sample Fabrication 107

6.3. Magnetoresistance Measurements 110
6.3.1. Magnetization Dependence of the Magnetoresistance 110
6.3.2. α-dependence of the CMR 112
6.4. Current-induced Effects 114
6.4.1. Spin-orbit Torques 114
6.4.2. Unidirectional Magnetoresistance 117
6.5. Discussion 119
6.6. Conclusions 126

7. Chiral Coupling: From Nanomagnets to Domain Wall Conduits 129
7.1. Chiral Coupling in Nanomagnets 130
7.1.1. In-plane/Out-of-plane Nanomagnets 131
7.1.2. Lateral Exchange Bias 133
7.1.3. Lateral Antiferromagnetic Coupling 134
7.1.4. Current-induced Switching 138
7.1.5. Size Limitations of the Chiral Coupling . . 138
7.2. Chiral Domain Wall Injectors 140
7.2.1. Structure of Chiral Domain Wall Injectors . 143
7.2.2. Magnetic Anisotropy Characterization . . 144
7.2.3. Asymmetric Domain Nucleation 146
7.2.4. DMI-driven Domain Nucleation 151
7.2.5. Driving Domain Wall Conduits 153
7.3. Summary 156

8. Summary and Outlook 159

Curriculum Vitae 165
Education 165
Teaching experience 165
Publications 166
Conference Contributions 167

A. Device Fabrication 169
A.1. Fabrication of MgO(001)/Fe/Ox Hall bars 169
A.2. Fabrication of Pt/Co/AlO_x domain wall injectors . 177

Bibliography 185

1. Introduction

1.1. Motivation

The information age has left its mark on society, with digital devices having found a purpose in every aspect of our lives. With an estimated 50 Billion devices connected to the internet, ranging from smart phones to the often ridiculed smart refrigerator, the all so frequently reported "ubiquity of smart devices" is far from an exaggeration. By now we live in a permanently connected society, where each personal device requires a constant drip feed of information from the "cloud" to function properly. The backbone of the infrastructure, which is able to serve our needs in a blink of an eye, are data centers, for which demand has rapidly grown.

To meet this demand, data centers have massively expanded in the last ten years, increasing their storage capacity more than 25-fold, network traffic 10-fold and workload 5-fold [1]. There are no signs of this expansion slowing down anytime soon, as the push towards increasingly higher fidelity and on demand entertainment is in full force. This problem was exacerbated in this year's COVID-19 pandemic, which has turned the average office worker into amateur streamers, forcing them to send pixelated videos of their backlit faces across the globe. In addition, the emergence of artificial intelligence, which is on the cusp of permeating every part of technology, is continuing our increasingly computing-intensive status quo. History indicates that this ever growing consumption is deep-rooted in our modern society,

ruling out restraint as a way forward, even in the face of a wilting planet.

Thanks to the concerted effort of engineers and scientists, however, the total energy usage of data centers has barely been affected by this expansion. Reductions in idle power, improved processor and storage efficiency and increased storage density have contributed to keep the increase of the total energy usage to a few percent [1], despite the massive increase in storage capacity, traffic and workload. To persevere in this constant battle, we need a breakthrough, as traditional data handling architectures, which have scaled incredibly well as advertised by Moore's law, are expected to reach their limits soon.

However, instead of waiting with baited breath for a panacea, recent developments demonstrate how a move towards specialized technologies that solve *specific* problems can lead to faster progress. A prime example is the tensor core, which can be thought of a stripped down computing core that has been optimized to significantly speed up artificial intelligence network computations, but lacks the flexibility of a traditional core. Since its first implementation into Google's data centers in 2015, it has made its way into enthusiast products a few years later and arrived in mainstream consumer products in 2020. The same principle, of developing solutions specific to the problem at hand, is pursued in quantum computers and neuromorphic computing, though these technologies have yet to reach maturity.

The development of new technologies is a never-ending endeavor, which requires strong interfacing between science and technology. A field that has excelled in this respect is the field of spintronics, which through the discovery of a vast assortment of physical phenomena, involving the interaction of electric charge and spin, has produced the building blocks of current smart devices [2]. In this thesis, we aim to expand the existing tool set used to conduct spintronic studies and develop future

technologies. For this we investigate the rich physics emerging from what might be considered the most underappreciated, yet very commonly occurring, component of the spintronic devices, namely ferromagnet (FM)/oxide interfaces. But before we can properly highlight the role of these interfaces and in which direction we can take them, we will first set the stage by covering the achievements that have led us here.

1.2. Background and Context

The poster child of spintronics is the giant magnetoresistance (GMR) , which introduces an electrical resistance in multilayer thin films depending on the relative orientation of two or more ferromagnetic layers that are separated by non magnetic metal layers [3, 4]. While magnetoresistive effects were not novel at the time of the discovery of the GMR [5, 6], what set it apart was the strength of its effect, causing resistance changes that were orders of magnitude larger than the other magnetoresistance (MR) effects at the time. The fact that the GMR causes large signals for small changes in the magnetization, quickly led to its implementation into magnetic hard disk drives, where it was used in the read head to sense the magnetic areas, i.e. bits, of the hard disk, which encode the stored information. The high sensitivity of the GMR allowed for the miniaturization of hard disk drive components down to the nano-scale, and subsequently led to an unprecedented increase in storage density. Remarkable is, how fast this development happened, starting with the experimental discovery of the GMR in parallel by Grünberg and Fert [3, 4], followed by first commercial products a decade later and culminating with the Nobel prize in 2007.

Not only was the Nobel prize awarded for the technological impact the GMR had but also for it being the first real application

of nanotechnology, as the GMR can only be observed in multilayer thin films. Thus, the implementation of the GMR into HDDs hinged on thin film fabrication techniques, which were only developed slightly over a decade before the discovery of the GMR , and includes several other phenomena exclusive to thin films, some of which we will discuss later on. The feature that lets thin film multilayers stand out, is the high interface to volume ratio, which amplifies interface-induced effects. These effects, some of which rely on the intrinsic broken inversion symmetry at the interface, often decay over a short distance, making them only observable at the nanoscale.

One of the earlier discovered interface effects was the perpendicular magnetic anisotropy (PMA) in Pd/Co multilayers [7], which aligns the magnetization of the FM to be perpendicular to the film plane, instead of parallel to the film, which is normally the case. PMA, in addition to the GMR, was essential in driving up the storage density of HDDs, as it offered a solution to a problem that plagued the miniaturization of magnetic storage until then. When magnetic bits are made smaller, the average lifetime of the stored information is reduced, since the energy to flip the bit decreases. To compensate for this, we would need to increase this energy through other means, which the PMA makes possible, as the strength of the induced uniaxial anisotropy is potentially very large. This potential was confirmed as time went on, as more heavy metal (HM)/FM combinations were found to exhibit PMA with increasing strength. While HM/FM interfaces undoubtedly induce strong PMA, owing to the strong spin orbit coupling of the HM, spin orbit coupling was soon found not to be the only mechanism behind PMA. Particularly, PMA was frequently observed in FM/oxide interfaces such as in the CoFe/AlO_x interface [8]. In this specific system, a study in the early 2000s showed that the strength of the PMA is determined by the oxidation level of the interface, transitioning from in-plane

magnetization for underoxized interfaces, to a peak PMA for a perfectly oxidized CoFe/AlO_x interface and subsequent degradation for overoxidized interfaces. Consequently, the origin of the PMA in FM/oxide cases was traced back to orbital hybridization, which is very sensitive to the oxygen level at the interface.

Not only can we induce anisotropies into single FM layers, in thin film multilayers, it is also possible to couple separate magnetic layers to each other using the so-called Ruderman–Kittel–Kasuya–Yosida (RKKY) coupling. The RKKY coupling is observed in structures where FM layers are separated by thin conducting non-magnetic metals, which causes the magnetization of the separated FM layers to align either ferromagnetically (parallel) or antiferromagnetically (anti-parallel). Whether ferromagnetic or antiferromagnetic coupling prevails for a specific separation layer, depends entirely on the thickness of the separation layer and can change within a few atomic monolayers.

Another phenomenon often used in conjunction with the RKKY coupling, in order fix the orientation of one of the FM layers, is the exchange bias emerging at FM/antiferromagnet interfaces. Here, the surface magnetization of the antiferromagnet, which for all practical purposes can be considered fixed in one direction, couples to the magnetization of the FM. This causes the FM to favor one specific direction and if overlapped with a uniaxial magnetic anisotropy, stiffens the magnetization to the point where, in the absence of external magnetic fields, the magnetization will automatically revert to that preferred orientation.

These examples were brought up to highlight the variety of phenomena that emerge exclusively in thin film structures, but at the same time, this reveals the limitations of these effects in that they *only* occur in thin film multilayers. This is the entry point of Chapter 7 of this thesis, where we aim to combine the control over the PMA in HM/FM/oxide structures with an interfacial effect,

namely the Dzyaloshinskii-Moriya interaction (DMI), to develop a technique to strongly couple laterally arranged nanomagnets.

The aforementioned DMI [9, 10] is an effect that occurs in structures that lack inversion symmetry, which in our systems is the case at the interface. The DMI is a local interaction between magnetic moments similar to the exchange coupling. The exchange coupling forces neighboring magnetic moments to be parallel or anti-parallel, giving rise to ferromagnetism and antiferromagnetism in the first place. The DMI on the other hand, promotes orthogonal arrangement of magnetic moments, resulting in spin spirals [11] and other non-trivial spin structures [12, 13]. Furthermore, the DMI imposes a handedness or chirality on the system. In systems with PMA, this chirality manifests largely in domain walls, which are the transitional regions between anti-parallel aligned regions with uniform magnetization, causing the magnetization in all domain walls to rotate with the same handedness [11, 14–16]. More specifically, the domain walls always chiral Néel wall configurations, which one, depends on the sign of the DMI. Effectively, this couples the in-plane (IP) component of a magnetic moment to the out-of-plane (OOP) component of its neighbors.

Here, we investigate coupled IP-OOP magnetized nanomagnets, in which the magnetization mimics the chiral Néel wall configuration that naturally occurs in DWs. For the fabrication of these devices, we leverage the nano-resolution of electron beam lithography to pattern the nanomagnet and selectively oxidize Pt/Co/AlO_x structures. The selective oxidation allow us to induce the PMA only in the desired regions while maintaining IP magnetization in the rest of the device. Using these nanomagnets we demonstrate, that the DMI can be used to achieve lateral and antiferromagnetic coupling of magnetic regions. With the lateral coupling, it is possible to generate large and complex networks of coupled magnetic regions, which has the potential to be used

in logic and non-Boolean devices [17, 18].

While the chiral coupling has a tremendous influence on the static behavior of the magnetization, its true value lies in the impact it has on the DW dynamics when combined with spin-orbit torques (SOTs), which is the focus of the second half of Chapter 7. The initial discovery of SOTs, in which unusually fast domain wall propagation induced by electrical currents was demonstrated [19], launched some of the most exciting investigations in the recent years in spintronics [20]. The massive body of work that has been generated since then has unravelled many mysteries surrounding SOTs, resulting in a deep understanding of the domain nucleation and domain wall propagation using SOTs [21, 22]. One of the revelations was that SOTs allow for ultra-fast switching of magnetic nano-islands. This is largely owing to very high DW velocities and the possibility of eliminating the incubation time, which otherwise would delay the nucleation processs [23, 24]. The high DW velocities make SOTs especially suitable to drive domain wall conduits or racetracks, a technology that, if realized to its full potential, promises a massive boost to our data storage capacity. Nevertheless, SOTs come with their own set of issues. One is the requirement of an external field parallel/anti-parallel to the injected current to deterministically switch the magnetization [21]. For the DW propagation, this field must either be maintained to prevent unwanted nucleation, or the current must be decreased, which prevents further nucleation but also decreases the DW velocity.

Here, we propose an alternative nucleation scheme, namely the use of lateral IP-OOP boundaries as chiral domain injectors [25]. At these boundaries, the chiral coupling stabilizes DMI-favored magnetization configurations, prohibiting the nucleation of new domains. Configurations unfavored by the DMI, on the other hand, are metastable, and domain nucleation using SOTs

is facilitated. Thus, in these chiral injectors the nucleation can be controlled by the magnetization direction of the IP region alone. Furthermore, once a domain was nucleated from a metastable state, it automatically reverts to a stable one, preventing any additional unwanted domain nucleation. The whole nucleation and propagation process can be done without external magnetic fields, using a stream of unipolar current pulses with constant amplitude. However we do not get rid of external fields completely, as the nucleation still has to be primed by flipping the IP region, for which we use external fields, though we do propose all electrical chiral injector designs.

A significant portion of SOT studies were conducted on HM/FM bilayers, which have proven to be an excellent model system, owing to the large spin Hall effect (SHE) associated with HMs [26]. The SHE is capable of converting an electrical current into a spin current, which subsequently affects the FM resulting in SOTs. The study of SOTs in HM/FM bilayers did not only reveal the inner workings of the SHE and the SOTs. The development of SOT characterization techniques inevitably advanced measurements capabilities and our understanding of the interplay between electrical, spin and heat currents, which shapes the transport properties of thin films. These advances are built on a thriving subset of MR studies, which have led to the discovery of a vast array of new MR effects.

The foundation of the MR in these bilayers are the famed anisotropic magnetoresistance (AMR) [5] and the anomalous Hall effect (AHE) [6], which are intrinsic to FMs. However, in these thin film bilayers the MR often deviates from the traditional models. Many of the additional contributions were traced back to the generation of different fluxes, i.e. heat and spin, by the electric current, which subsequently produce their own electric signal. Among the additional MR contributions are the unidirectional MR (UMR) [27] and the the spin Hall MR (SMR) [28], which have

typically been attributed to the spin current generated by the SHE.

Although the SMR was first demonstrated in HM/insulating FM bilayers, based on a mechanism that is tied to the fact that the FM does not conduct, other effects resembling the SMR emerged soon thereafter. However, before long, other possible mechanisms were brought into the picture, such as magnetic proximity effects in HMs, which can generate a MR in the HM itself [29], and the anisotropic interface MR [30]. As studies went on to include a more diverse set of systems, SMR-like signals were also found in systems with no HMs [31–33], therefore lacking the obvious provider of the SHE, which is essential to the manifestation of the SMR. Thus, for single layer FM thin films several new mechanisms were proposed, one of which is based on the AHE in structures with high aspect ratio [34]. For thicker textured layers, the geometrical size effect was suggested to be the source of the SMR-like magnetization dependence [35]. Finally, a recent investigation [36] went back to one of the original MR studies [37] and found that in partially crystalline materials, the presence of an SMR-like magnetization dependence of the MR is actually allowed by symmetry and thus could be much more common that previously thought.

This barrage of phenomena, which all describe the same manifestation of the MR from a different perspective, shows how difficult the determination of microscopic origin of these effects can be. This is not exclusive for the SMR-like signal, which we only used as an example, but applies to every MR and current-induced effect that was discovered in recent years. On top of that, the models used to explain one effect should also be relevant for the rest of the transport properties, complicating the process even further. Understanding the magnetization sensing capabilities that are available to us, is paramount to maximize their potential. In the last part of this thesis, we aim to unify the library of MR and

current-induced effects, which are relevant to magnetic thin films. Building on prior MR studies, we investigate a large variety of transport properties of epitaxial MgO/Fe/oxide structures using a single measurement technique, with the goal of correlating cause and effect across all transport properties measured. For this, we develop a characterization methodology specifically for anisotropic systems, which allows for the consistent and precise quantification of the MR and current-induced effects.

1.3. Chapter Overview

The content of this this thesis has already been weaved into the previous section but to repeat, two main projects form the foundation of this thesis. One focuses on the lateral chiral coupling of IP-OOP boundaries and in the other we investigate the transport properties of epitaxial single layer iron. The underlying fundamental physics and characterization methods applied in the two projects have a lot of overlap. Thus this thesis is structured to front load these commonalities, which are then adapted to the specific cases in the project Chapters.

In Chapter 2, we lay the groundwork of the fundamental magnetic interactions, which play a role in our thin films. This encompasses the direct interaction between magnetic moments, magnetic anisotropies and the various methods to manipulate the magnetization.

Chapter 3 introduces the magnetotransport phenomena studied in this work, which manifest through the interaction between external magnetic fields, magnetization of solids, electric currents and other fluxes. Specifically, we describe the traditional MR model, which includes the AMR and AHE. This model is then adapted for crystalline ferromagnetic thin films. In addition to the MR, we also discuss the origin of current-induced

effects, such as the thermo-electric effects and spin current related phenomena.

In Chapter 4, we dive into the measurements and analysis techniques that were developed for this work. We start with the description of the harmonic voltage analysis, which forms the backbone of the transport measurements, followed by the specific manifestations of the transport phenomena in this measurement technique, listed in the previous chapter. To quantify these phenomena in systems with magnetocrystalline anisotropy, I developed an iterative fit procedure that requires no assumptions or input other than the independent and dependent variables from the measurement itself, which is covered in its entirety in this chapter.

Chapter 5 contains a detailed description of the growth and pattering of the FM/Ox systems studied in this work, which entails the deposition methods, techniques to control the oxidation and lithography procedures. In addition to a description of the fabrication techniques used, we provide general considerations that need to be taken into account to optimize the device quality.

In Chapter 6, we report on our investigation of the MR and current-induced effects in epitaxial MgO(001)/Fe/oxide structures. As mentioned above, we measure and separate the abundance of magnetotransport phenomena in a singular study using a single measurement technique designed to map the angular dependence of crystalline magnetotransport effects. In this way, we obtain insight into the complex physics of crystalline magnetotransport devices, opening the door to the future harnessing of these rich materials.

In Chapter 7, we present the work, consisting of two projects, that led to the discovery of the lateral chiral coupling [25] and we propose functional designs based on this new phenomenon [25]. The first half covers the chiral coupling as it was discovered in IP-OOP nanomagnets. We show that the magnetization of the IP

and OOP regions are strongly coupled to each other through the DMI, for which we provide proof using imaging techniques and transport measurements. The complexity and size of chirally coupled structures is also shown to be scalable as the coupling can propagate changes in the magnetization over multiple IP-OOP boundaries. Due to the local nature of the chiral coupling, the boundary density must be kept high though for the chiral coupling to fully determine the magnetic configuration.

From a magnetization dynamics point of view, the IP-OOP boundary can be considered as a configurable nucleation site. This is demonstrated in the second half of the chapter, where we explore the usage of IP-OOP in domain wall conduits as injectors. Using SOTs, we show that the domain nucleation probability strongly depends on the chirality of the magnetic configuration at the IP-OOP boundary. By exploiting this property we devise a switching protocol with which any arbitrary sequence of domains with alternating magnetization can be injected into domain wall conduits, using a stream of unipolar current pulses with constant amplitude.

Finally, in Chapter 8, we summarize the achievements of this thesis and give an outlook of interesting directions to follow in coming years.

2. Magnetic interactions

The study of the magnetoresistance, current-induced effects, and magnetization dynamics in thin film heterostructures, which form the goal of this work, is underpinned by the fundamental understanding of the interactions that govern the behavior of the magnetization of a ferromagnet. This chapter contains a general introduction to the relevant interactions, some of which are intrinsic to magnetic materials and some that we have control over. For the specific implementation of these interactions into macrospin simulations we refer to Chapter 4.

2.1. Fundamental Interactions

2.1.1. Exchange Interaction

The first question we need to answer when talking about magnets is what is the interaction that enables a collection of atomic magnetic moments, to spontaneously align and form a net magnetization $\boldsymbol{M} = M_s \boldsymbol{m}$ and give rise to ferromagnetism, instead of randomly pointing in all directions. The answer is the direct interaction between individual magnetic moments, specifically the exchange interaction. The exchange interaction is a quantum mechanical effect thar originates from the exchange symmetry of indistinguishable particles, in this case electrons. Thus, it is a short-ranged interaction, governing only the interaction between

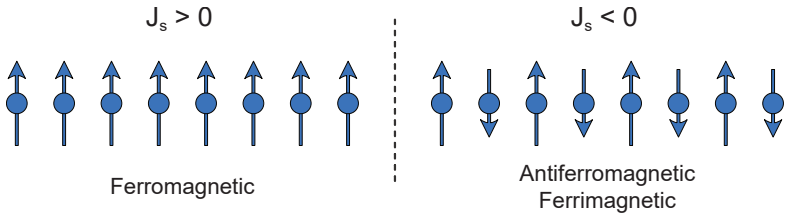

Figure 2.1.: The exchange interaction forces the magnetic moments to align with each other giving rise to ferromagnetism or antiferromagnetism/ferrimagnetism. The sign of the exchange constant A^{exc} determines whether parallel or anti-parallel alignment is preferred. For positive values of A^{exc} all moments align in the same direction, resulting in a ferromagnet. For negative values of A^{exc} the moments alternate resulting in an antiferromagnet if all moments are equal, or ferrimagnet if the two sublattices, one with the moments pointing up and the other with moments pointing down, do not have the same magnetization.

neighboring spins $\boldsymbol{S}$, leading to an energy term [38]

$$E^{exc} = -\frac{2A^{\mathrm{exc}}}{a} \sum_{i \neq j} \left(\boldsymbol{S}_i \cdot \boldsymbol{S}_j \right), \tag{2.1}$$

where A^{exc} is the exchange stiffness constant and a is the lattice constant of the FM. As can be seen from this expression, the exchange interaction describes the parallel ($A^{\mathrm{exc}} > 0$) or anti-parallel ($A^{\mathrm{exc}} < 0$) alignment of neighboring spins, which leads to either ferromagnetism or antiferromagnetism, respectively. For Co and Fe thin films the exchange stiffness constant depends on the thickness and the interfaces leading to values ranging from 5–30 pJ m^{-1} [39].

In the absence of the exchange interaction, we observe para-

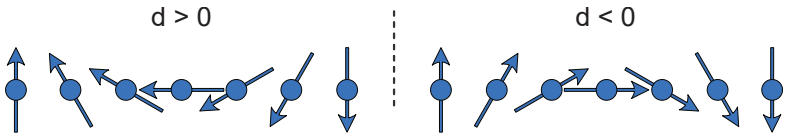

Figure 2.2.: The DMI forces perpendicular alignment of neighboring spins, which is in competition with the exchange interaction. The result of strong DMI are spiraling magnetic microstructures as shown, where the rotational sense, or chirality, of these structures depends on the sign.

magnetism and diamagnetism, where the magnetic moments can be aligned with an external magnetic field but do not align spontaneously.

2.1.2. Dzyaloshinskii-Moriya Interaction

Like the exchange interaction, the DMI describes the coupling between neighboring spins, with the difference that the DMI promotes perpendicular alignment of spins. The DMI was first observed in antiferromagnetic α-Fe_2O_3, where it induced weak ferromagnetism [40]. Although the original groundwork was layed decades ago, a working theory that is able to predict both the sign and strength of the DMI in HM/FM bilayer thin films, was only developed recently [41]. There, two factors were found to impact the DMI. The first is the orbital HM-FM hybridization, which increases the more the electron bands overlap at the interface, and consequently increases the strength of the DMI. The sign of the DMI depend on the spin-orbit coupling, which results in spin mixing-orbital transitions at the interface. In other words, the spin-orbit coupling only allows for specific spin transitions from a d-orbital in the FM to a d-orbital in the HM and

these transition cause the spin to rotate slightly with a chirality set by the spin-orbit coupling. The rotated spin interact with the magnetization in the FM as they transition back, causing the magnetization to rotate in a chiral manner as well.

The effect of the DMI on the magnetic moments is highlighted in the energy contribution

$$E^{\mathrm{dmi}} = -\sum_{i \neq j} \boldsymbol{d}\left(\boldsymbol{u}_{\mathbf{ij}}\right) \cdot \left(\boldsymbol{S}_i \times \boldsymbol{S}_j\right) \tag{2.2}$$

where d is the DMI vector that defines the strength and rotational sense or chirality of the DMI. d is determined by the vector $\boldsymbol{u}_{\mathbf{ij}}$ that connects the location of $\boldsymbol{S}_i$ to the location of $\boldsymbol{S}_j$. This expression shows that the DMI by itself will promote the formation of magnetic spirals, where the magnetization rotates around $\boldsymbol{d}$ as we travel along $\boldsymbol{u}_{\mathbf{ij}}$ [42]. For the Pt/Co/AlO_x bilayers studied here $d \approx -1\,\mathrm{mJm}^{-2}$ [17, 43], resulting in what is referred to as left-handed chiral spin structures.

2.1.3. Magnetostatic Energy

In addition to these short range but strong interactions, magnetic moments also interact on a longer range, though more weakly, through the magnetostatic energy[38]. This energy can be thought of as the cost involved in maintaining a magnetic field generated by the magnetization outside of the body of the magnet. Minimizing this field entails the reduction of the density of surface pole charges $\boldsymbol{M} \cdot \boldsymbol{n}$, where $\boldsymbol{n}$ is the surface normal. This can be achieved either by pairing opposite surface pole charges, resulting in an altered magnetization configuration, or by aligning the magnetization parallel to as much of the surface as possible.

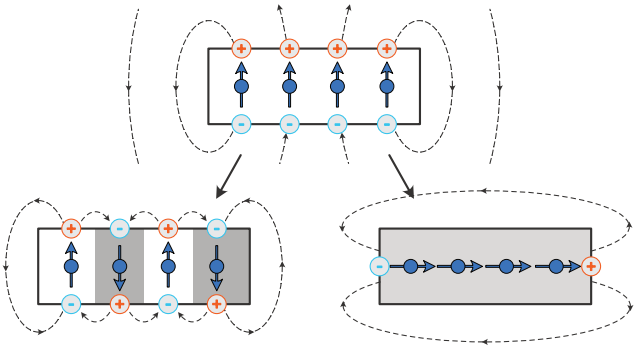

Figure 2.3.: The magnetostatic energy describes the the cost of maintaining magnetic fields outside of the magnet, which scales with the density of surface pole charges. These so-called magnetic charges are generated by the surface magnetization itself when aligned perpendicular to the surface. The magnetostatic energy can be minimized by pairing opposite charges or by aligning the magnetization parallel to the surface.

2.2. Magnetic Anisotropy

For now we have mostly addressed how magnetic moments align relative to each other, however, a major factor in determining the direction of the magnetization $\boldsymbol{m}$ is the magnetic anisotropy. As the name implies, here, the symmetry of magnets, or in our case more specifically magnetic thin films, changes the energy associated with certain magnetization directions, resulting in preferred axes to align with, also called easy axes, or axes to avoid, called the hard axes. Magnetic anisotropies can be caused by a variety of factors and in any given magnetic system a number of these anisotropy axes may exist and overlap, generating a complex energy landscape for the magnetization. Here, we will

discuss the sources of the anisotropies in the epitaxial Fe system and the Pt/Co/AlO_x system studied in Chapter 6 and Chapter 7, respectively, starting with the shape anisotropy.

2.2.1. Shape anisotropy

Shape anisotropy is one of the consequences of trying to minimize the magnetostatic energy. If we treat the magnetization as a single uniform vector that cannot minimize the magnetostatic energy by breaking into domains, the remaining option to lower the energy is to minimize the surface poles. As a result, $\boldsymbol{m}$ will typically prefer to align parallel to surfaces, and minimize the area with the magnetization pointing perpendicular to the surface. The energy associated with the shape anisotropy is given by[38].

$$E^{\text{dem}}/V = \frac{\mu_0 M_s}{2} \sum_{i=x,y,z} N_i m_i^2, \tag{2.3}$$

where μ_0 is the vacuum permeability and $\boldsymbol{N_i}$ are the components of the demagnetizing factor, which depends on the shape of the magnet. For a system with only one elongated or constricted dimension the shape anisotropy introduces a uniaxial anisotropy, such that

$$E^{\text{uni}}/V = K^{\text{uni}}\left(1 - (\boldsymbol{m} \cdot \boldsymbol{u})^2\right) \tag{2.4}$$

where K^{uni} is a uniaxial anisotropy constant and $\boldsymbol{u}$ is the direction of the axis that coincides with the longest dimension of the shape. For flat shapes K^{uni} is negative, while for elongated shapes K^{uni} is positive. Notable examples of systems with significant shape anisotropy are magnetic thin films, in which it generates a hard axis perpendicular to the film, and magnetic micro-/nanowires, in which the high elongation creates an easy axis along the wire. In these two examples the shape anisotropy exists by virtue of the design of the overall shape of the system, however it can also manifest more subtly as a result of textured roughness [44–47].

2.2.2. Magnetocrystalline Anisotropy

Magnetocrystalline anisotropy arises from the interplay of the spin-orbit interaction and the energy splitting of the d-orbitals induced by the crystal field. This results in systems, where the anisotropy is tied to the crystal structure of the ferromagnet. An example of this are the epitaxial Fe layers studied in this work (see Chapter 6), where the cubic symmetry of the crystal produces a cubic magnetocrystalline anisotropy with three perpendicular easy axes. If we set the <100> directions of the cubic crystals to correspond to $\boldsymbol{x}$, $\boldsymbol{y}$, and $\boldsymbol{z}$, the energy density for a cubic crystal is [38]

$$E^{\text{cub}}/V = K^1 \left(m_x^2 m_y^2 + m_x^2 m_z^2 + m_y^2 m_z^2\right) + K^2\, m_x^2\, m_y^2\, m_z^2 \qquad (2.5)$$

where K^1 and K^2 are anisotropy constants that dictate the direction of the easy axes. In the epitaxial MgO(001)/Fe systems studied here, the easy axes coincide with the three main axes of the crystal, which is described by a large value for $K_1 \approx 50\,\text{Jm}^{-3}$ and a small one for $K_2 \approx \pm 5\,\text{Jm}^{-3}$ [48]. As the magnetocrystalline anisotropy is so closely related to the crystal structure, straining the structure will change the anisotropy. This phenomenon is called magnetostriction, which in strained epitaxial Fe films can introduce a uniaxial anisotropy along the strain direction.

In polycrystalline systems, such as Pt/Co/AlO_x on which we will focus in Chapter 7, the individual contributions to the anisotropy of the randomly oriented crystal grains usually end up cancelling each other and therefore suppress the manifestation of an magnetocrystalline easy axis. If the orientations of the crystals are not random and not evenly distributed, this can result in a texture of the film, which can induce magnetic anisotropy even in non-epitaxial films.

2.2.3. Interface Anisotropy

The magnetic anisotropy is not only determined by the crystalline structure of the ferromagnet and its shape, but also by the materials that the ferromagnet is in contact with. At the interface between the ferromagnet and its neighboring materials, orbital hybridization can be the source of strong magnetic anisotropies, which introduces a uniaxial anisotropy perpendicular to the interface

$$E^{\text{int}}/V = K^{\text{int}}\Big(1 - (\boldsymbol{m} \cdot \boldsymbol{n})^2\Big). \tag{2.6}$$

where K^{int} is the interface-induced anisotropy term and $\boldsymbol{n}$ is the normal of the interface. In the prominent case of Pt/Co/AlO_x this anisotropy can be used to overcome the shape anisotropy of a thin film and induce a PMA [49]. Furthermore, as the interface anisotropy is induced by orbital hybridization, the Co/AlO_x interface is a prime example of the impact the oxidation state can have on the interface anisotropy. Here, both slight underoxidation or overoxidation will greatly diminish the induced anisotropy, weakening it enough for the system not to exhibit a PMA.

2.3. Magnetic Domains and Domain Walls

As described above, the magnetic configuration and behavior are determined by a number of competing interactions, not all of which favour a single domain state. While the exchange interaction promotes the alignment of all magnetic moments, the DMI and magnetostatic interactions promote non-collinear alignment of magnetic moments. The combination of these competing interactions can lead to a multi-domain state, made up of different domains that individually consist of a uniform magnetization direction, but are not aligned with one another. In the regions separating different domains, aptly named DWs,

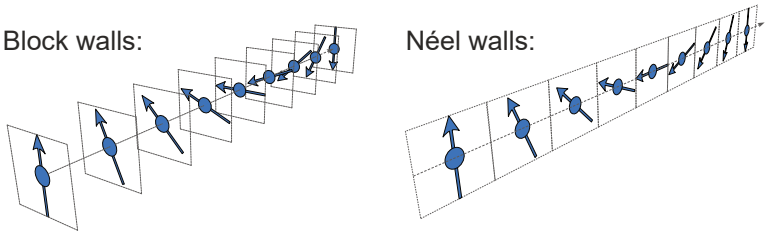

Figure 2.4.: The structure of 180° DWs in thin films can be categorized into two types. In Bloch walls the magnetization rotates around the normal $\boldsymbol{n}$ of the DW. In Néel walls the magnetization rotates around $\boldsymbol{m} \times \boldsymbol{n}$. In the presence of the DMI, chiral Néel walls prevail, which has been exploited with great success for DW propagation with SOTs.

the magnetization smoothly transitions from one domain to the other[38].

A lot of effort has been put into resolving the configuration of the magnetization inside the DWs, as their internal structure governs many dynamic properties of a magnet. Of special interest to our work presented in Chapter 7 are 180° DWs. In these cases, we can identify two types of DWs, namely Bloch walls where the magnetization rotates around the normal $\boldsymbol{n}$ of the DW and Néel walls where it rotates around $\boldsymbol{m} \times \boldsymbol{n}$ in either direction [50].

In thin films with PMA, Bloch walls are generally energetically favored due to their lower magnetostatic energy. Constricting the DW, for example in a nano wire, pushes the preference towards Néel walls, since the rotation of $\boldsymbol{m}$ towards the axis of the wire reduces the magnetostatic energy compared to the Bloch configuration. The transition between the two DW types is gradual as the wire becomes more narrow, leading to DWs with

hybrid structures that have characteristics of both Bloch and Néel walls [51]. While this mechanism plays a role in determining the DW type, it does not explain why in the Pt/Co/AlO_x system, we exclusively observe Néel walls [11, 14]. The main determining factor of the DW configuration in these systems is the DMI, which in addition to forcing Néel walls, also lifts the degeneracy of different rotation directions or chiralities [14, 15], which is a prerequisite for the deterministic manipulation of these DWs using electric currents [52].

2.4. External Influences

While the various interactions and anisotropies listed above are leading factors in determining the magnetization and its microstructure, as material parameters, they offer us little *active* control over the magnetization during a measurement. Here, we will cover what options are available to us to precisely manipulate the magnetization using external influences.

2.4.1. Zeeman Energy

We start with the interaction of $\boldsymbol{M}$ with an external magnetic field $\boldsymbol{H}^{\mathbf{ext}}$, which is described by the potential energy [38]

$$E^{\mathrm{zee}} = -\boldsymbol{M} \cdot \boldsymbol{H}^{\mathbf{ext}} = -M_{\mathrm{s}} H^{\mathrm{ext}} \cos\theta^{\mathrm{ext}} \tag{2.7}$$

also known as the Zeeman energy. Here, θ^{ext} is angle spanned by $\boldsymbol{M}$ and $\boldsymbol{H}^{\mathbf{ext}}$. As stated in Eq. 2.7, the Zeeman energy is minimized when the magnetization and the external field are parallel and increases as the misalignment θ^{ext} increases.

The external magnetic field $\boldsymbol{H}^{\mathbf{ext}}$, produced by an electromagnet in our case, is not the only contribution to the Zeeman energy, as the electric currents sent through our samples for the magnetotransport measurements also generate an Oersted field. In the

most well-known case - that of a cylindrical wire - the Oersted field circulates around the wire, with a magnitude of the field inversely proportional to the distance from the centre of the wire. For thin films, the Oersted field outside of the film can be approximated using an infinitely extended sheet model by

$$H^{\mathrm{oe}} = \frac{\mu_0 J}{2}, \tag{2.8}$$

where μ_0 is the vacuum permeability, J_0 is the current density. The resulting H^{oe} is a field parallel to the film plane and perpendicular to the current. Because H^{oe} is only generated outside of the layer, a uniform current flowing through the ferromagnet will not generate an Oersted field that affects the ferromagnet itself. However, any current running through neighboring layers will generate an Oersted field, which will affect the ferromagnet.

2.4.2. Spin-orbit Torques

In addition to the Oersted field, the electrical current can exert a torque on the magnetization by producing a spin current, i.e. a flow of electrons with aligned spins. The alignment of the spin results in a spin polarization $\boldsymbol{\sigma}$ that can interact with the magnetization. This process naturally occurs in ferromagnets in a variety of ways and can be artificially enhanced by inversion symmetry breaking, such as through the interface engineering in heavy metal/ferromagnet bilayers [20, 53]. The mechanisms behind the spin polarization of electrical currents are covered in more detail in Section 3.4.2. SOTs then arise through the exchange interaction between the magnetization and the spin polarization. The torques exerted by the spin polarization can be decomposed into two components, in particular, the field-like ($\propto \boldsymbol{m} \times \boldsymbol{\sigma}$) and the damping-like SOT ($\propto \boldsymbol{m} \times (\boldsymbol{m} \times \boldsymbol{\sigma})$) [54]. The field-like and damping-like SOTs have been named for their symmetry, which

mimic the precession and damping torque, respectively, of a magnetic field parallel to $\boldsymbol{\sigma}$. Nevertheless, they are not just two components of a single field, but instead are more accurately described via the two effective fields $\boldsymbol{H}^{\mathbf{fl}}$ and $\boldsymbol{H}^{\mathbf{dl}}$ that can scale independently. The direction of these effective fields are defined by

$$\boldsymbol{H}^{\mathbf{fl}} \propto \boldsymbol{\sigma} \tag{2.9}$$

resulting in a field-like torque $\propto \boldsymbol{m} \times \boldsymbol{\sigma}$ and

$$\boldsymbol{H}^{\mathbf{dl}} \propto \boldsymbol{m} \times \boldsymbol{\sigma} \tag{2.10}$$

giving us the damping-like torque $\propto \boldsymbol{m} \times (\boldsymbol{m} \times \boldsymbol{\sigma})$. SOTs have been used to great effect for magnetization manipulation in HM/FM systems, ranging from chiral DW propagation in magnetic wires to full magnetization reversal of magnetic dots and Hall bar structures [20].

2.5. Magnetization Dynamics

As was discussed in this chapter so far, a multitude of effects are acting on the magnetization at any time, each leaving its unique footprint on the energy landscape experienced by $\boldsymbol{M}$. For a single magnetic moment, the manner with which $\boldsymbol{m}$ navigates through this landscape is governed by the Landau-Lifshitz-Gilbert equation [38]

$$\frac{\partial \boldsymbol{m}}{\partial t} = -\frac{\gamma}{1+\alpha^2}\, \boldsymbol{m} \times \boldsymbol{H}^{\mathbf{eff}} - \frac{\gamma\alpha}{1+\alpha^2}\, \boldsymbol{m} \times \left(\boldsymbol{m} \times \boldsymbol{H}^{\mathbf{eff}}\right), \tag{2.11}$$

where $\gamma = \frac{2\mu_B}{\hbar}$ is the gyromagnetic ratio, α is a phenomenological damping parameter and $\boldsymbol{H}^{\mathbf{eff}}$ is the effective field, containing all the aforementioned effects ranging from direct interactions, anisotropies to external influences. The motion described by

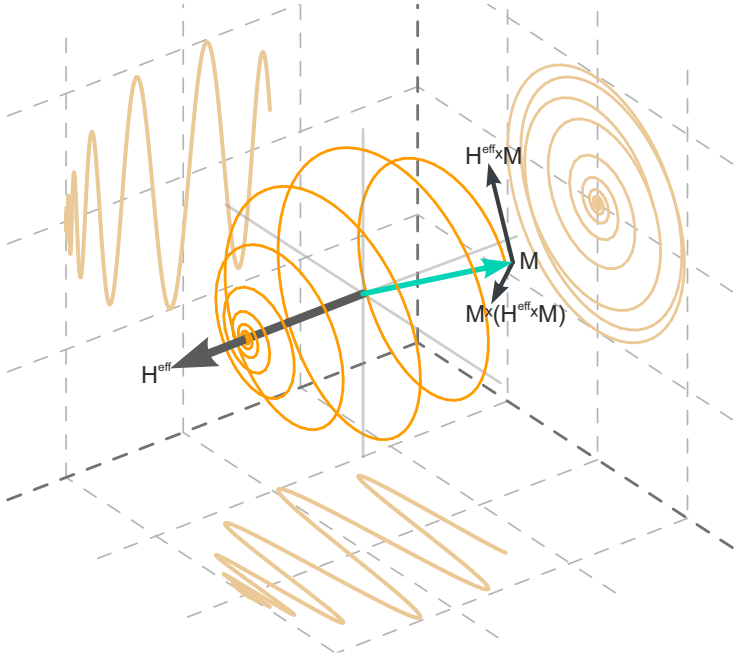

Figure 2.5.: The interaction between the magnetization and an effective field $\boldsymbol{H}^{\mathbf{eff}}$ is governed by the LLG equation. The LLG equation describes the trajectory of the magnetization as a combination of a precession $\left(\boldsymbol{H}^{\mathbf{eff}} \times \boldsymbol{m}\right)$ around $\boldsymbol{H}^{\mathbf{eff}}$ and a motion towards the field $\left(\boldsymbol{m} \times \left(\boldsymbol{H}^{\mathbf{eff}} \times \boldsymbol{m}\right)\right)$. Here we show the trajectory of the magnetization as it aligns with the effective field

the LLG equation is a damped oscillation of $\boldsymbol{m}$ around $\boldsymbol{H}^{\mathbf{eff}}$ (Figure 2.5). The first term describes the magnetic torque $\boldsymbol{H}^{\mathbf{eff}} \times \boldsymbol{M}$, which results in a precession of $\boldsymbol{M}$ around $\boldsymbol{H}^{\mathbf{eff}}$. The second term on the other hand, represents the damping in the system, which pulls $\boldsymbol{M}$ towards $\boldsymbol{H}^{\mathbf{eff}}$ and eventually aligns the two, resulting in

the equilibrium configuration of $\boldsymbol{M} \parallel \boldsymbol{H}^{\mathbf{eff}}$.

The LLG equation applied to a single magnetization accurately describes its evolution, but to grasp the full extent of the reversal process of a magnet one can do the same on a large array of coupled moments, as is done in micromagnetic simulations. If we only look at a single magnetic moment reversing as a result of $\boldsymbol{H}^{\mathbf{ext}}$, the LLG equation indicates thereafter a magnet reverses simply by each moment precessing around the field until the magnetization settles due to the damping.

While such a simultaneous, uniform reversal from a single domain state to another single domain state might be observed in small systems with strong exchange coupling, it is energetically inefficient. Thus, instead of all magnetic moments reversing in unison, it can be more efficient to pay the cost of introducing a DW, which mediates the reversal. As $\boldsymbol{H}^{\mathbf{eff}}$ is applied, domains with opposite magnetization start to nucleate, typically around inhomogeneities in the material such as the edge of the sample. As these domains grow, the DWs are pushed out, merging and expanding until the magnetization completely reverses.

The same process can be seen when SOTs are applied to reverse the magnetization in heavy metal/ferromagnet bilayers. These systems stand out not only for their high conversion of electrical current to SOTs but also for their strong DMI. In this case the DMI leads to a tilt of the magnetization at the edges of the magnet even in a single domain state. This tilt is the weak point that is exploited to very efficiently nucleate new domains [21]. Moreover, the fixed chirality of the Néel walls allows for very efficient conversion of SOTs into deterministic and fast motion of the DWs, which rapidly expands the domains.

From the interactions and anisotropies to magnetic fields and SOTs, each component can be an essential ingredient in building a magnetic device that fits our exact use case.

3. Magnetotransport

Magnetotransport, as it pertains to this work, encompasses phenomena which manifest through the interaction between external magnetic fields, magnetization of solids, electric currents, spin currents and heat currents. The growing understanding of the intricacies of these phenomena has led to the realization of electric generators, magnetic sensors and magnetic storage among others, which to this date have become ubiquitous, affecting many aspects of modern society. Despite these great achievements, the constant effort towards further innovations has not stopped and great strides have been made towards the implementation of faster, denser and non-volatile magnetic memory and the mimicking of neural networks. Here, we will explore the phenomena that lay the base of magnetic sensing and writing, starting with the magnetoresistance.

3.1. Magnetoresistance

The resistivity $\boldsymbol{\rho}$ relates the electric field $\boldsymbol{E}$ to the injected current density $\boldsymbol{J_c}$ such that

$$E_\mathrm{i} = J\, j_\mathrm{c}^j\, \rho_{\mathrm{i}j} \tag{3.1}$$

where summation is performed over repeated indices. Here, J is the amplitude and $\boldsymbol{j_c}$ is the direction of the current density. For magnetotransport, the elements of the resistivity matrix ρ_ij depend on the direction of the magnetization $\boldsymbol{m} = (m_\mathrm{x}, m_\mathrm{y}, m_z)$,

namely

$$\rho_{ij} = \rho^0_{ij} + \rho_{ijk} m_k + \rho_{ijkl} m_k m_l + \dots . \tag{3.2}$$

where summation is performed over repeated indices for x, y and z The coefficients of this series expansion can be restricted with symmetry considerations.

For up to second order terms and isotropic, i.e. polycrystalline, systems, the general expression of $\boldsymbol{\rho}$ for an arbitrary magnetization direction can be written as [55]

$$\boldsymbol{\rho} = \rho^{\parallel} \boldsymbol{j_c} + (\rho^{\parallel} - \rho^{\perp}) (\boldsymbol{m} \cdot \boldsymbol{j_c}) \boldsymbol{m} + \rho^{\text{ahe}} (\boldsymbol{m} \times \boldsymbol{j_c}), \tag{3.3}$$

where $\rho^{\parallel}$ is the longitudinal resistivity we measure for $\boldsymbol{j_c} \parallel \boldsymbol{m}$. On the other hand, $\rho^{\perp}$ corresponds to the longitudinal resistivity in the case where $\boldsymbol{j_c} \perp \boldsymbol{m}$. Lastly, ρ^{ahe} corresponds to a Hall resistivity, or transverse resistivity, which is measured perpendicular to the current and the magnetization.

The terms here were grouped to reflect the various effects that drive them. The first term on the right side corresponds to the magnetization-independent ohmic resistivity. The second term corresponds to the AMR and generates an electric field ($\boldsymbol{E^{amr}}$) in the direction of the magnetization, which is proportional to the alignment of $\boldsymbol{j_c}$ and $\boldsymbol{m}$. The contribution of the last term is related to the AHE, which produces an electric field ($\boldsymbol{E^{ahe}}$) perpendicular to $\boldsymbol{j_c}$ and is strongest when $\boldsymbol{j_c}$ and $\boldsymbol{m}$ are perpendicular to each other.

3.1.1. Anisotropic Magnetoresistance

The longitudinal component of Eq. 3.3 ($E^{\text{amr}}_{\text{L}} = \boldsymbol{E^{amr}} \cdot \boldsymbol{j_c}$) describes the AMR as it was first discovered [5], particularly

$$\begin{aligned} E^{\text{amr}}_{\text{L}} &= J \left(\rho^{\parallel} - \rho^{\perp}\right) (\boldsymbol{m} \cdot \boldsymbol{j_c})^2 \\ \rho^{\text{amr}}_{\text{L}} &= \left(\rho^{\parallel} - \rho^{\perp}\right) \cos^2 \phi \end{aligned} \tag{3.4}$$

where ϕ is the angle between $\boldsymbol{j_c}$ and $\boldsymbol{m}$ and $\rho^{\mathrm{amr}} = \rho^{\parallel} - \rho^{\perp}$ is the amplitude of the AMR. The origin of the AMR is thought to be the spin-orbit coupling, which causes the scattering cross section of conduction electrons to depend on the direction of the magnetization. The characteristic magnetization dependence of the AMR is embodied by the $\cos^2\phi$ term. Thus, the AMR is symmetric upon magnetization reversal and exhibits maxima for $\boldsymbol{m}$ parallel or antiparallel to $\boldsymbol{j_c}$ and minima for perpendicular alignment. Furthermore, as the signal of the AMR only depends on the angle ϕ, it is insensitive to rotations of $\boldsymbol{m}$ around $\boldsymbol{j_c}$ which do not change the angle between them.

3.1.2. Planar Hall Effect

In conjunction with the AMR, the PHE will always appear in MR measurements. The PHE is not a unique effect by itself but is simply the transverse manifestation of the AMR. More specifically, whereas the AMR corresponds to the longitudinal component of $\boldsymbol{E}^{\mathbf{amr}}$, the PHE is its transverse component

$$\begin{aligned} \boldsymbol{E}_{\mathbf{H}}^{\mathbf{amr}} &= \left[\boldsymbol{E}^{\mathbf{amr}} - \boldsymbol{E}_{\mathbf{L}}\boldsymbol{j_c}\right] \\ &= J(\rho^{\parallel} - \rho^{\perp})\,(\boldsymbol{m}\cdot\boldsymbol{j_c})\left[\boldsymbol{m} - (\boldsymbol{m}\cdot\boldsymbol{j_c})\boldsymbol{j_c}\right]. \end{aligned} \tag{3.5}$$

The name of this effect comes from the fact that is observed as a transverse signal in the plane spanned by $\boldsymbol{m}$ and $\boldsymbol{j_c}$, with a strength of

$$\begin{aligned} E_{\mathrm{H}}^{\mathrm{amr}} &= \sqrt{\|E^{\mathrm{amr}}\|^2 - \|E_{\mathrm{L}}\|^2} \\ \rho_{\mathrm{H}}^{\mathrm{amr}} &= \frac{(\rho^{\parallel} - \rho^{\perp})}{2}\sin 2\phi. \end{aligned} \tag{3.6}$$

Thus to reiterate, whenever there is a resistivity difference between the parallel and perpendicular configurations of $\boldsymbol{j_c}$ and $\boldsymbol{m}$, both the AMR and PHE will be present with the same amplitude

$\rho^{\mathrm{phe}} = \rho^{\mathrm{amr}}$. Consequently, the PHE shares symmetry characteristics with the AMR, such as the insensitivity to magnetization reversal.

3.1.3. Anomalous Hall Effect

Lastly, we want to discuss the AHE, which is associated with the last term, $\boldsymbol{E}^{\mathbf{ahe}}$, in Eq. 3.3. For this purpose, we first need to introduce the ordinary Hall effect, which produces an electric field perpendicular to the current $\boldsymbol{j}_{\mathbf{c}}$ and an magnetic flux density in the material $\boldsymbol{B}$, such that $\boldsymbol{E}^{\mathbf{ohe}} = R_{\mathrm{H}}\,(\boldsymbol{B} \times \boldsymbol{J}_{\mathbf{c}})$, where R_{H} describes the strength of the linear scaling of this transverse field with the magnetic flux density $\boldsymbol{B}$.

In magnetic materials, however, non-linear scaling was observed at a certain H^{ext} and also, the signal persisted even after $\boldsymbol{H}^{\mathbf{ext}}$ had been removed. This behavior, named anomalous Hall effect for its deviation from the OHE, was traced back to an additional contribution, which does not depend on $\boldsymbol{H}^{\mathbf{ext}}$ but instead depends on the magnetization. In particular, the expression of the AHE was found to be [56]

$$\boldsymbol{\rho}^{\mathbf{ahe}} = \rho^{\mathrm{ahe}}(\boldsymbol{m} \times \boldsymbol{j}_{\mathbf{c}}) \tag{3.7}$$

which corresponds to the last term in Eq. 3.3. From this expression we can see that the AHE does not have a longitudinal component and is maximal for perpendicular arrangement of $\boldsymbol{m}$ and $\boldsymbol{j}_{\mathbf{c}}$. Unlike the AMR, this effect scales linearly with $\boldsymbol{m}$ and as such reverses upon magnetization inversion.

3.2. Crystalline Magnetoresistance

In many MR studies the observations have veered from this traditional model of the AMR, with observed changes in the

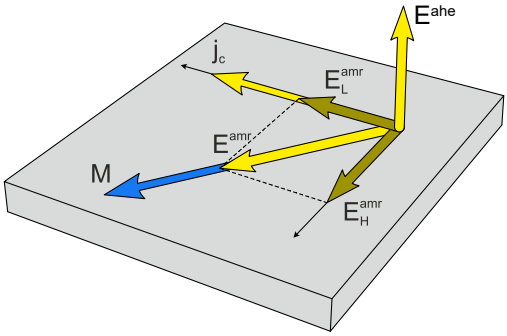

Figure 3.1.: In the classical magnetotransport model for polycrystalline systems, the application of a current to a ferromagnet results in two responses. The first generates the $\boldsymbol{E}^{\mathbf{amr}}$-field parallel to the magnetization that scales with $(\boldsymbol{m} \cdot \boldsymbol{j}_\mathbf{c})$. This response is associated with the AMR and the PHE, which correspond to its longitudinal and transverse component, respectively. The second response is related to the AHE, which produces a field perpendicular to both $\boldsymbol{m}$ and $\boldsymbol{j}_\mathbf{c}$.

longitudinal resistance upon rotations of the direction of the magnetization $\boldsymbol{m}$ around the direction of the current $\boldsymbol{j}_\mathbf{c}$ and a dependence on the direction of the current with respect to the crystal structure of the ferromagnet [36, 37, 57–62]. As was prefaced above, the resistivity matrix given in Eq. 3.3 holds for isotropic materials in the presence of a current density $\boldsymbol{J}_\mathbf{c}$ and the magnetization $\boldsymbol{M}$. However, as more symmetries are broken, less restrictions are put on the resistivity coefficients, allowing for a more varied set of effects to occur. Replacing the isotropic FM with a crystalline FM is the obvious route to further limit the symmetry, which leads to the manifestation of the bulk crystalline MR (CMR). Whereas before, $\rho_{\mathbf{ij}}$ in Eq.3.2 only depends on the relative orientation of $\boldsymbol{j}_\mathbf{c}$ and $\boldsymbol{m}$, in crystalline systems the

resistivity is also sensitive to their orientation with respect to the crystal axes, which was demonstrated by Döring for cubic Ni crystals early on [37].

More recent work confirms that these early observations hold even in crystalline thin film systems leading to higher order coefficients of the series expansion shown in Eq. 3.2. Thus higher order ϕ-dependencies, as in $\cos^n \phi$ terms for even integer values of n, show up in the AMR [36, 57–62].

The CMR is also relevant in textured polycrystalline system. The texture in these systems prevents the CMR to be completely suppressed. Not only can such textures introduce higher order ϕ-dependencies, they can also break a property that is intrinsic to the classical AMR, namely its insensitivity to rotations of $\boldsymbol{m}$ around $\boldsymbol{j_c}$ [36, 37].

3.3. Interfacial Crystalline Magnetoresistance

Inherent to thin film systems is the large surface to volume ratio, which increases the influence of interface related effects on the system. Among these are spin-orbit fields, which can be generated at the interface through various effects as explored later on in Section 3.4.2. These current-induced spin-orbit fields will subsequently influence the electric transport properties of the system [63]. To evaluate their effect on the resistivity, we include them in the series expansion as we did with the magnetization in Eq. 3.2. As shown in the work of Hupfauer *et al.* [63], the symmetry of the additional signal generated by the spin-orbit fields is very system specific, as it mimics the symmetry of the interface, which itself depends on the crystal structure and the strain caused by the heteroepitaxy at the interface.

3.4. Current-induced Effects

So far we have established the magnetoresistance effects that are generated in a magnetic thin film as a response to an applied electric current $\boldsymbol{J_c}$. However, in addition to this direct response, electric currents in magnetic thin films also induce a host of other effects. For this work, the current-induced effects we focus on are the ones that can change the direction of the magnetization $\boldsymbol{m}$, which indirectly influences the magnetoresistance, and the ones that generate new fluxes, which subsequently are able produce a signal and add to $\boldsymbol{E}$. We will discuss two effects that fall into this category, namely, thermoelectric effects and spin-current related effects.

3.4.1. Thermoelectric Effects

As we have seen with the magnetoresistance, the injection of an electric current in a magnetized material will generate an electric field depending on the relative configuration of $\boldsymbol{j_c}$ and $\boldsymbol{m}$. However, a heat flux $\boldsymbol{j_q}$ can in principle also produce similar electric fields. This results in an expression for the thermoelectric resistivity $\boldsymbol{rho_q}$ analogous to Eq. 3.3

$$\boldsymbol{\rho_q} = \rho_q^{\perp} \boldsymbol{j_q} + (\rho_q^{\parallel} - \rho_q^{\perp})\,(\boldsymbol{m} \cdot \boldsymbol{j_q})\,\boldsymbol{m} + \rho_q^{\mathrm{ane}}\,(\boldsymbol{m} \times \boldsymbol{j_q}). \tag{3.8}$$

Similarly to the MR, which was split into a AMR, PHE and AHE, the thermal effect can be decomposed into the magnetothermopower (MTP), planar Nernst effect (PNE) and anomalous Nernst effect (ANE). The source of the heat flux j_q in our patterned magnetic thin films is the Joule heating caused by the injected current in conjunction with the asymmetric heat dissipation, which is prevalent in these films. Since Joule heating is the source of the thermal flux, the thermoelectric effect shown here

does not scale linearly with the injected current like the MR, but instead scales with J^2, which can be used to separate the two.

3.4.2. Origin of Spin Currents

Analogous to how we make use of the charge of electrons to create electrical currents, we can exploit their spin to create spin currents $\boldsymbol{j_s}$. A spin current represents the flow of angular momentum associated with the spin of the electrons. Instead of directly injecting a spin current, we generate a finite spin current by either have to be filtering or separating spins according to their orientation. The resulting spin current is characterized via the vectors $\boldsymbol{j_s}$, which describes the direction of the flow of majority or up spins, and $\boldsymbol{\sigma}$, which corresponds to the spin polarization, i.e. the direction of the dominant angular momentum.

Spin-polarized Currents in Ferromagnets

Electrical currents are naturally spin-polarized in FMs owing to the different conductivity of majority and minority spin electrons in the transition metals considered here [55]. This can be better understood by adopting a two current model, where the electrical current consists of two sub currents, namely $j_\uparrow$ and $j_\downarrow$, which are only comprised of majority and minority spins, respectively. In other words, the electrical current can be written as

$$j_c = j_\uparrow + j_\downarrow. \tag{3.9}$$

In the conduction band, generally, there is no imbalance between the two spin directions and thus $j_\uparrow = j_\downarrow$. This can change however, if we consider the scattering of electrons from the conduction band into the d-band. The imbalanced occupation of the d-band makes it less likely for majority spins to scatter simply because there are fewer free states to scatter into, which increases the

conductivity of majority spins. As a consequence, a portion of the current becomes spin polarized, which is given by

$$j_s = j_\uparrow - j_\downarrow. \tag{3.10}$$

The spin-dependent conductivity is ultimately the source of the spin-polarization of electrical currents in FMs and has been exploited with great success through the GMR [3, 4]. One example are GMR spin valves, which consist at least of two stacked FM layers separated by an non-magnetic layer, $\boldsymbol{j_c}$ is pushed from one FM layer (FM1), through the oxide, into the second FM layer (FM2) for the purpose of sensing the magnetization direction $\boldsymbol{m_2}$ of FM2 with respect to the one of the first layer $\boldsymbol{m_1}$, which has to be fixed and known. In this process, after passing through FM1, the injected current is spin-polarized, such that $\boldsymbol{j_s}$ is parallel to $\boldsymbol{j_c}$ and $\boldsymbol{\sigma}$ is parallel to $\boldsymbol{m_1}$. This spin current then flows into FM2, where, as a consequence of the spin dependent conductivity of FM2, the resistance it experiences can vary massively depending on the relative orientation of $\boldsymbol{\sigma}$ and $\boldsymbol{m_2}$. Particularly, if the magnetization of the two layers are parallel, the spin-polarized current flowing into the second layer will experience a lower resistance as a result of the spin-dependent conductivity. On the other hand, for opposite magnetization configurations, the resistance will be higher. The resistance difference between the two configurations allows us to determine the direction of the magnetization in FM2 with respect to the reference, which is FM1.

Moreover, using the same spin current injection principle, it was later demonstrated that the spin current cannot only be used to sense the magnetization of the second layer, but that it is actually capable of writing, or manipulating, $\boldsymbol{m_2}$ [64, 65]. The writing occurs as a consequence of spin transfer torques, where angular momentum of the spin-polarized current from the first FM is transferred to the second FM.

The requirement of a fixed reference layer to spin polarize the current was soon overcome with the demonstration of the Spin Hall effect in HM/FM bilayer thin films.

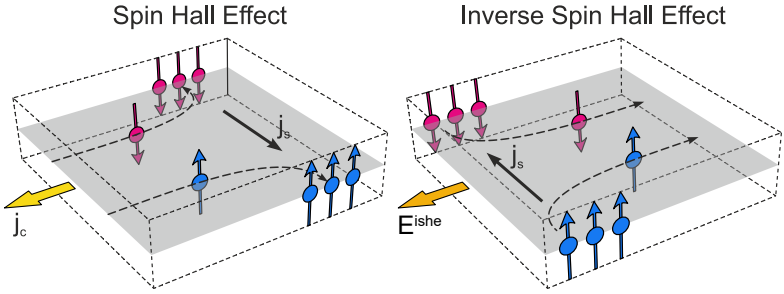

Figure 3.2.: The SHE produces a spin current $\boldsymbol{j_s}$ in all directions perpendicular to an electric current j_c, leading to spin accumulation on all surfaces parallel to the current. Onsager reciprocal relations demand that there is an inverse effect of the SHE, namely the ISHE, that will produce an electrical current from a spin current.

Spin Hall Effect

The main feature of the SHE, which we make use of for the purpose of this work, is the generation of spin currents $\boldsymbol{j_s}$ that are *transverse* to $\boldsymbol{j_c}$ with $\boldsymbol{\sigma}$ perpendicular to both $\boldsymbol{j_c}$ and $\boldsymbol{j_s}$ [20, 26]. The perpendicular spin-current allows for $\boldsymbol{j_s}$ to be injected into the FM from a neighboring conducting layer, while the electric current can be pushed in the film plane instead of perpendicular to it, reducing the total current required to reach the same current densities. As microscopic reversibility must be respected, as per the Onsager reciprocal relations [66], an inverse process must exist, where a spin current injected into the material generates a perpendicular electric current, which is called the inverse SHE

(ISHE). The combination of SHE and ISHE has been found to be the origin of a large collection of current induced effects.

Among the most studied materials that exhibit a strong SHE, are heavy metals, such as Pt, W and Ta, owing to their intrinsically high spin orbit coupling [20, 26]. The study of these materials has greatly advanced the field of spintronics and led the discovery of many spin-current induced effects, paving the way to novel magnetization manipulation and sensing capabilities. While HMs are on the top of the list in terms of SHE efficiency, they are by far not the only option. Particularly relevant for this work is the possibility of inducing spin currents in partially oxidized normal metals, with efficiencies claimed to compete with HMs. More specifically, in Cu thin films with perpendicular oxidation gradients, the asymmetric distribution of scattering centers can generate perpendicular spin currents, which exhibit the same symmetry as the SHE [67–69].

In the examples mentioned, the SHE has always been generated externally and injected into the FM. However, like HMs, FMs have appreciable spin orbit coupling, allowing for the SHE to generate a spin current in the FM itself. Until recently, spin currents with a transverse spin polarization, i.e. a component of σ perpendicular to the magnetization, have been thought to been very short lived in FMs due to their strong interaction with the magnetization, leading to rapid dephasing of the transverse component.

For transverse spin currents generated by the intrinsic SHE, this is to not necessarily the case though, as the spin orbit coupling can allow for the majority and minority eigenstates, which the transverse spin polarization is comprised of, to possess the same phase, removing the possibility of dephasing until spin scattering events change the states [70]. In thin film FMs this means that the spin current can travel far enough to accumulate at the interfaces, leading to the manifestation different effects on the magnetization

that will discuss later on in this chapter.

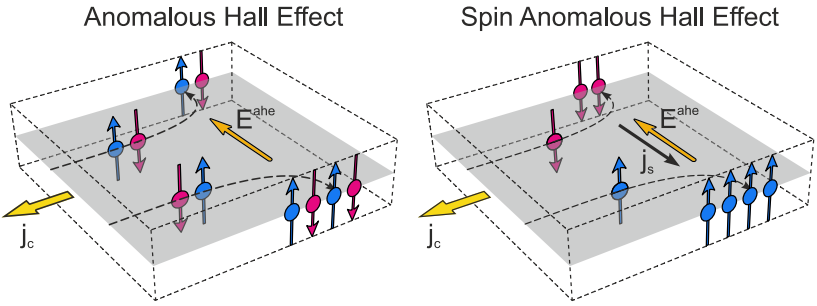

Figure 3.3.: AHE and SAHE geometry for out-of-plane magnetization. The classical AHE produces an electric field $\boldsymbol{E}^{\mathbf{ahe}}$ perpendicular to both $\boldsymbol{j}_{\mathbf{c}}$ and the magnetization. Electrons accumulate at the edges with no net spin polarization. Since electric currents are naturally spin-polarized in ferromagnets, the transverse current generated by $\boldsymbol{E}^{\mathbf{ahe}}$ will also be spin-polarized, leading to a spin current perpendicular to the injected current. This phenomenon is referred to as SAHE

Spin Anomalous Hall Effect

Another spin current source intrinsic to FMs is the spin polarized version of the previously discussed AHE [71, 72]. The spin AHE (SAHE), is a consequence of spin-dependent conductivity of FMs, which as described above, spin polarizes the injected current. However, the spin polarization is not exclusive to any direction of the current, meaning that the transverse current generated by the AHE will also be spin polarized [70]. By itself, the SAHE will not manifest the same phenomena as the SHE, since the spin polarization of the current produced by the SAHE is collinear with the magnetization of the FM. But scattering at interfaces

with strong spin orbit fields can change this and introduce a component of σ that is transverse to the magnetization, allowing for spin-current-induced effects to manifest [72]. The scattering processes that allow for such a reorientation of σ are the spin filtering and spin precession scattering. In the case of spin filtering, the component of σ parallel to the spin orbit field will selectively reflect or transmit through the interface, while during the spin precession scattering the component perpendicular to the spin orbit field will precess around the field changing the direction of σ.

Rashba-Edelstein Effect

Interfaces do not only act on existing spin currents but can themselves be the origin of localized spin currents. The naturally broken inversion symmetry at any interface will lead to an asymmetric potential perpendicular to that interface, which in addition to spin-orbit coupling manifests in the Rashba effect [73]. This effect lifts the degeneracy of the spin bands and couple the spin of an electron to its momentum. As a result, a current flowing parallel to the interface will spin polarize perpendicular to the direction of the current and the interface normal, and generate an accumulation of spins at the interface, the process of which is called the Rashba-Edelstein effect [74, 75].

3.4.3. Spin-current-induced Effects

Up to this point we have introduced three spin current sources, namely the SHE, the SAHE and the Rashba-Edelstein effect, which take effect in the FM itself, at its interfaces and in neighboring HM layers. Now we will explore the magnetoresistance effects that these spin currents can give rise to in thin film systems.

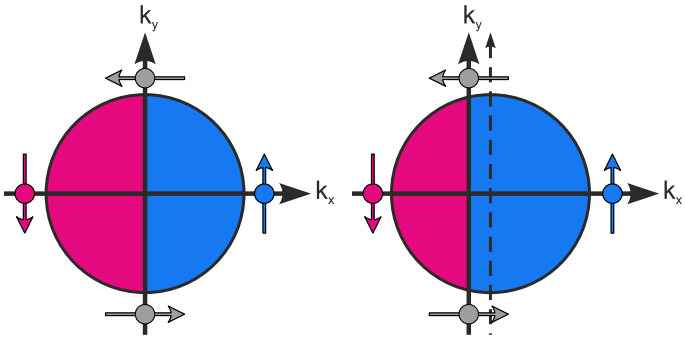

Figure 3.4.: Schematic representation of the Fermi surface of a conduction electron band with spin-momentum coupling. The Rashba effect couples the spin of an electron to its momentum as shown on the left, where electrons moving along x or $-x$ are spin polarized along y or $-y$, respectively. The polarization of the total current is proportional to the difference between the colored areas, which for no applied current is zero. However, applying a current corresponds to a shift of the circle, resulting in a finite spin polarization of the current.

Spin Hall Magnetoresistance

The SMR is an effect unique to thin films, first observed in HM/insulating FM systems [28]. In these systems, a significant MR was found despite the fact that no current passes through the FM. The fundamental basis of the SMR is the SHE, which generates a spin current perpendicular to the electric current injected into the HM. This spin current is then assumed to build up a spin accumulation, or an increasingly unbalanced electrochemical potential for opposite spins as we approach the interface. The accumulating spins can then transfer their angular momentum

to the magnetization, which is most efficient for perpendicular arrangement of $\boldsymbol{\sigma}$ and $\boldsymbol{m}$, reducing the spin accumulation compared to collinear arrangements. Simultaneously, the gradient in the potential forces the accumulated spins to diffuse away from the interface, generating a diffusive spin current. This diffusive spin current in exchange produces its own electric field via the ISHE. The magnetization dependence of the ISHE is what is then picked up as the SMR. The change in the resistance caused by this phenomenon reflects the strength of the spin accumulation and consequently is largest for collinear $\boldsymbol{m}$-$\boldsymbol{\sigma}$ configurations, such that

$$\rho^{\mathrm{smr}} \propto (\boldsymbol{m} \cdot \boldsymbol{\sigma})^2 \tag{3.11}$$

Anomalous Hall Magnetoresistance

Similar to the SHE, the SAHE will also produce to a spin accumulation that can add to the magnetoresistance via the ISHE, resulting in the anomalous Hall MR (AHMR) [34]. Since the driving force of the AHMR is the SAHE, it can be observed even in single layer FMs. The symmetry of the AHMR is defined by two phenomena.

First is the magnetization dependence of the spin accumulation in the FM, which is caused by the SAHE. As the spin current generated by the SAHE is proportional to $\boldsymbol{m} \times \boldsymbol{j}_{\mathbf{c}}$, there will not be any spin accumulation at any interface if $\boldsymbol{m} \parallel \boldsymbol{j}_{\mathbf{c}}$. If $\boldsymbol{m} \perp \boldsymbol{j}_{\mathbf{c}}$ on the other hand, the spin accumulation is maximized and accordingly the electric field produced by the ISHE will be larger. However, unlike the SHE, the SAHE does not evenly accumulate spin on all interfaces parallel to the current. Instead, the spin accumulation will be the largest on the interfaces that are perpendicular to $\boldsymbol{m} \perp \boldsymbol{j}_{\mathbf{c}}$. Because of the constricted geometry of thin films, however, not all interfaces are equal, resulting in

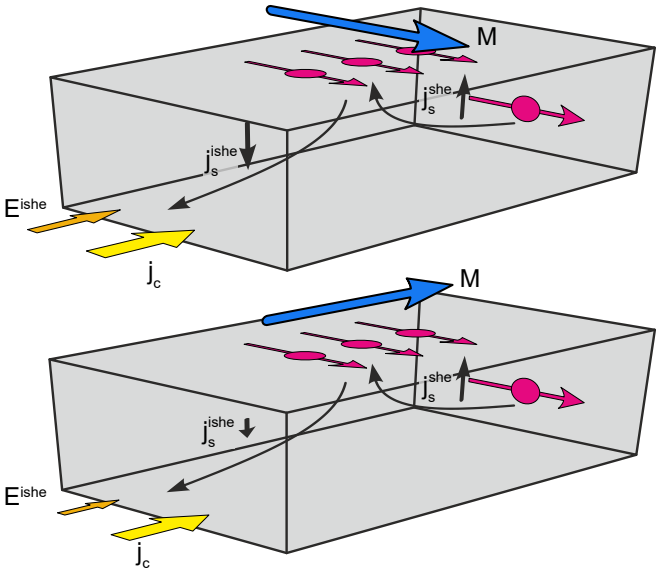

Figure 3.5.: Schematic illustration of the SMR. The SHE produces a spin accumulation, which subsequently generates a back-flowing diffusive spin current $\boldsymbol{j}_{\mathbf{s}}^{\mathbf{she}}$. This diffusive spin current generates a charge current due to the ISHE, which adds to the injected current, thus lowering the resistance. While the spin current generated by the SHE is constant, the spin accumulation at the interface can vary as it interacts with the magnetization at the interface. For perpendicular configuration of $\boldsymbol{m}$ and $\boldsymbol{\sigma}$, the spins can transfer their momentum to the magnetization very efficiently, weakening the accumulation in the process, while for collinear arrangement this is not the case. This results in a magnetization dependence of the ISHE generated signal, which corresponds to the SMR.

larger spin accumulations on the interfaces perpendicular to the film plane, namely the edges.

To understand this difference we have to take into account the second phenomenon that defines the AHMR, which is the cancellation of spin accumulations on opposite interfaces. For this, it helps to think of a spin accumulation as a build up of chemical potential $\mu^{\uparrow/\downarrow}$. If the potentials $\mu^{\uparrow}$ and $\mu^{\downarrow}$, building up on opposite interfaces, would completely overlap, they would neutralize each other, cancelling the effects of the SAHE. Normally, this is not the case though, as the distance over which electrons can diffuse before they lose their spin information is limited by spin-flip scattering events. This distance is characterized by the spin diffusion length λ, which applied to this case describes how quickly the spin accumulation decays as we leave the interface. In materials with strong spin orbit coupling, λ is typically in the range of a few nanometers [76]. Compared to the micrometer distances between the edges of the thin films, this means that the spin accumulations on opposite interfaces will have completely decayed before they can overlap. The situation changes if we look at the interfaces parallel to the film, which are only separated by the film thickness of less than 2 nm in this work. Here, the overlap can be significant, weakening the spin accumulation and as a result reducing the electric field generated by the ISHE.

As a result, phenomenologically, the magnetization dependence of the AHMR ends up resembling the SMR, where

$$E\left(\boldsymbol{m} \parallel \boldsymbol{j}_{\mathbf{c}}\right) \approx E\left(\boldsymbol{m} \parallel \boldsymbol{n}\right) > E\left(\boldsymbol{m} \parallel \left(\boldsymbol{n} \times \boldsymbol{j}_{\mathbf{c}}\right)\right), \tag{3.12}$$

where $\boldsymbol{n}$ is the interface normal. The specific relation depends on the geometry of the device cross section as well as spin diffusion length of the FM.

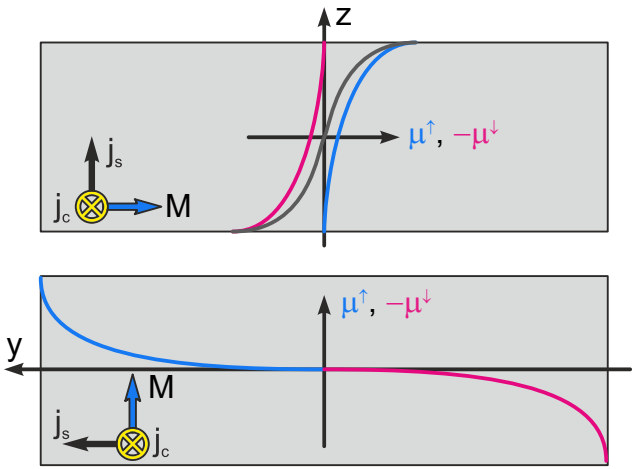

Figure 3.6.: Schematic of electrochemical potential build up, for up spins (blue) and down spins (magenta), as a result of the SAHE. For in-plane magnetization (top), the SAHE produces an electrochemical potential of opposite spins on the opposite interfaces parallel to the plane. Since, these interfaces are in such close approximation, the potentials overlap, leading to partial cancellation. In out-of-plane magnetized films (bottom), the accumulation occurs on the edges of the film and thus no cancellation of the potential is observed. This difference allows for the AHMR to occur, as the change in the electrochemical potential, relates to a change in the spin accumulation, which is responsible for the ISHE.

Spin-Dependent Unidirectional Magnetoresistance

Next, we want to discuss another recently discovered spin-current-induced MR [27], namely the spin dependent unidirectional MR (sd-UMR). The sd-UMR, is a result of the interaction

between the spin dependent conductivity of a FM and spin currents injected into said FM [77]. This causes an MR that is described by

$$\rho^{\mathrm{sd-umr}} \propto (\boldsymbol{m} \cdot \boldsymbol{\sigma}) \tag{3.13}$$

We have already seen above how a spin accumulation can generate additional electric signals through the ISHE. However, a change in the resistance of FMs can also be achieved by modifying the spin polarization of the injected current pushed along the interface and taking advantage of the spin dependent conductivity. If $\boldsymbol{\sigma}$ is parallel to $\boldsymbol{m}$ the proportion of majority spins increases, lowering the resistance, as scattering is reduced for majority spins. On the other hand, if $\boldsymbol{\sigma}$ opposes $\boldsymbol{m}$, the resistance increases, due to the increased proportion of minority spins.

Spin-Flip Unidirectional Magnetoresistance

As more studies were conducted about the UMR, is was soon discovered that the insensitivity of the UMR to external magnetic fields ceases to apply at external fields in the order of tens of mT [77, 78]. As the external field is lowered, the UMR starts to diverge and can even change the sign in the process in certain cases, which ultimately indicates that the UMR is made up of multiple components in addition to the spin-dependent UMR. This field dependent component was identified as the spin-flip UMR, the explanation of which first requires the introduction of the magnon magnetoresistance.

The magnon magnetoresistance describes a change in the resistance arising from electron-magnon scattering [79]. The likelihood of this scattering is regulated by the magnon population, which can be manipulated and suppressed with external fields. As a result, the magnon magnetoresistance is generally observed as a decrease of the longitudinal resistance with increasing external fields.

However, a change in the magnon population can also be induced by the injection of spin currents, which is the origin of the spin-flip UMR. Since this change is small in general, this effect can easily be suppressed by the external field and thus is only observed at low fields.

In addition to exhibiting a different external field dependence compared to the sd-UMR, the magnetization dependence and current dependence of the spin flip UMR can also differ from the sd-UMR.

4. Measurement Technique & Data Analysis

This chapter will cover the whole procedure we developed to characterize the magnetotransport properties of thin films with strong magnetic anisotropy. We use this to extensively study the properties of epitaxial MgO(001)/Fe thin films as layed out in Chapter 3, although this procedure can be also be applied to polycrystalline HM/FM systems, which are the focus of Chapter 7. The final goal of these measurements is to quantify current-induced effects such as the SOTs and the UMR, for which we will first need to characterize the magnetoresistance and magnetic anisotropy. This journey starts with the design of the devices we use for our study, followed by the analysis of the signal produced by the electrical transport measurement technique used. Finally, we will present a flexible method to simulate the signal for any set of external fields, current-induced fields and magnetic anisotropies, with which we can extract material parameters and quantify magnetotransport phenomena with high precision from our data.

4.1. Hall Bar Geometry

The full mapping of the magnetotransport properties of thin films is most easily achieved in Hall bar structures, which allow for the simultaneous measurement of transverse and longitudinal signals. In this work, we use Hall bars consisting of two crosses

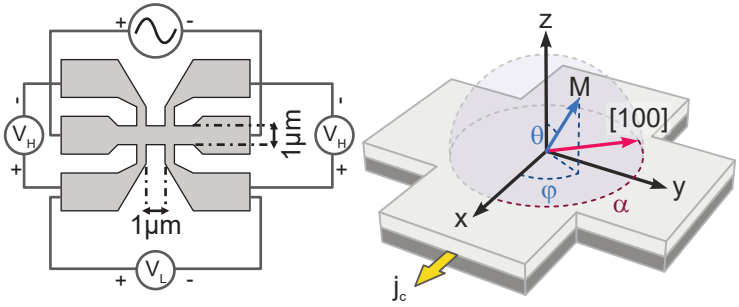

Figure 4.1.: Left: is an illustration of a typical Hall bar device used for electrical transport measurements. The Hall bar consists of a current channel, with a width of 1 µm, through which an AC current is applied. The remaining four contacts, each with a width of 0.5 µm, are used to pick up two transverse voltages across the current channel and one longitudinal voltage along the channel over a distance of 1 µm. On the right, we show the measurement coordinate system, which is bound to the Hall bar. The axes are defined by $\boldsymbol{x} \parallel \boldsymbol{j_c}$ and $\boldsymbol{z} \parallel \boldsymbol{n}$, where $\boldsymbol{n}$ is the surface normal. The angle α is the angle between the current and the crystal axis MgO[100]. The illustrations are not to scale.

as shown in Figure 4.1. In these devices, the current is pushed through the main central channel and the remaining four contacts are used to pick up the generated signals. In our case we typically measured both transverse signals and one longitudinal signal, measured on the contacts that serve as the positive terminal for the transverse signal. We minimized the resistance of the devices by setting the main channel width to $w = 1\,\mu\text{m}$ and length to $l = 1\,\mu\text{m}$ while the voltage lines were kept at $0.5\,\mu\text{m}$. Limiting the resistance was mainly a technical concern, as it allows us to

maximize the sensitivity of the voltmeter used.

For our purposes, the Hall bar structure is used as the anchor point with which we define our measurement coordinate system, such that $\boldsymbol{x}$ is parallel to the current direction $\boldsymbol{j_c}$ and $\boldsymbol{z}$ is parallel to the substrate normal. In the special case of HM/FM bilayers, however, we adapt $\boldsymbol{z}$ to be parallel to the HM/FM interface normal pointing from the HM to the FM, instead of the commonly used substrate normal. This means that depending on the HM/FM stacking order, $\boldsymbol{z}$ will either be parallel or anti-parallel to the substrate normal. This definition has the advantage of resulting in consistent signs of the SOTs, UMR and DMI regardless of the stacking order of the bilayer. For example, in Pt/Co/AlO_x, where the Pt is closest to the substrate, and in the reversed stack AlO_x/Co/Pt, the SOT and UMR have the same sign in the respective coordinate systems, determined only by the material choice.

Since our coordinate system is fixed to the current, the magnetization can point in any arbitrary direction. In such a coordinate system, the direction of the magnetization $\boldsymbol{m}$ is naturally given by the cartesian coordinates $\boldsymbol{m} = \left(m_x, m_y, m_z\right)$ or the spherical coordinates $\boldsymbol{m} = (\cos\varphi \sin\theta, \sin\varphi \sin\theta, \cos\theta)$, where θ is the polar angle between $\boldsymbol{m}$ and $\boldsymbol{z}$ and φ is the azimuthal angle between the projection of $\boldsymbol{m}$ onto the xy-plane and $\boldsymbol{x}$.

Finally, the magnetotransport properties in crystalline systems heavily depend on the direction of the current with respect to the crystal axes. To probe this, multiple devices with different rotations were patterned into the film, instead of a long curved Hall bar, which has been used in similar studies. Ultimately, the choice was made to maintain a consistent measurement geometry at the cost of more spread out devices. The angle between the current and the main crystal axes will be denoted with α in this work, measured from $\boldsymbol{j_c}$ to one of the crystal axes.

4.2. Harmonic Voltage Analysis

The measurement technique of choice for this work is the harmonic voltage analysis, which is a high precision measurement technique that has been shown to allow for the separation of the magnetotransport effects according to their current scaling [27, 54, 80, 81]. In this section, we narrow down the scope of the magnetotransport effects described in Chapter 3 and will see how they specifically manifest with this measurement technique. By the end, we will have analyzed the voltage produced by our probing AC current and provide analytical expressions and simulation techniques to recreate the signal and fit our data.

Our starting point is the voltage generated by the injection of an alternating current $I(t) = I_0 \cos \omega t$. If we include both the linear and quadratic response, the induced voltage reads as

$$V(t) = R_1(\boldsymbol{H})\, I_0 \cos \omega t + R_2(\boldsymbol{H})\, I_0^2 \cos^2 \omega t, \tag{4.1}$$

where the resistance term $R_1(H)$ contains the MR effects that scale linearly with the current, while $R_2(H)$ contains thermoelectric effects and the UMR, which scale quadratically. In addition to the effects that directly generate a signal, we also need to take into consideration the effect of the Oersted field and SOTs on the direction of the magnetization $\boldsymbol{m}$. We can think of the current-induced fields to modulate $\boldsymbol{H}$ such that

$$R_1(\boldsymbol{H}) = R\Big(\boldsymbol{H}^{\mathbf{stat}} + \boldsymbol{H}^{\mathbf{I}} \cos \omega t\Big), \tag{4.2}$$

where $\boldsymbol{H}^{\mathbf{stat}}$ corresponds to the current independent static component of $\boldsymbol{H}$ and $\boldsymbol{H}^{\mathbf{I}}$ corresponds to the dynamic current-induced component, which scales linearly with the current, hence the $\cos \omega t$ term. We can approximate the resistance with a series expansion of R to first order with respect to $\boldsymbol{H}$ around $\boldsymbol{H}^{\mathbf{stat}}$,

yielding

$$\begin{aligned} R_1(\boldsymbol{H}) &\approx R(\boldsymbol{H}^{\mathbf{stat}}) + \frac{dR}{d\boldsymbol{H}} \cdot (\boldsymbol{H} - \boldsymbol{H}^{\mathbf{stat}}) \\ &\approx R(\boldsymbol{H}^{\mathbf{stat}}) + \frac{dR}{d\boldsymbol{H}} \cdot \boldsymbol{H}^{\mathbf{I}} \cos(\omega t). \end{aligned} \tag{4.3}$$

After inserting this new expression of the resistance into Eq. 4.1 and normalizing by the amplitude of the AC current I_0, the voltage becomes

$$\begin{aligned} V(t)/I_0 &= \left(R(\boldsymbol{H}^{\mathbf{stat}}) + \frac{dR}{d\boldsymbol{H}} \cdot \boldsymbol{H}^{\mathbf{I}} \cos \omega t \right) \cos \omega t + R_2(\boldsymbol{H}) I_0 \cos^2 \omega t \\ &= R(\boldsymbol{H}^{\mathbf{stat}}) \cos \omega t + \left(\frac{dR}{d\boldsymbol{H}} \cdot \boldsymbol{H}^{\mathbf{I}} + R_2(\boldsymbol{H})\, I_0 \right) \left(\frac{1}{2} - \frac{\cos 2\omega t}{2} \right) \\ &= R^{0\mathrm{f}} + R^{1\mathrm{f}} \cos \omega t + R^{2\mathrm{f}} \cos 2\omega t, \end{aligned} \tag{4.4}$$

where

$$R^{1\mathrm{f}} = R(\boldsymbol{H}^{\mathbf{stat}}) \tag{4.5}$$

and

$$R^{0\mathrm{f}} = R^{2\mathrm{f}} = \frac{1}{2} \frac{dR}{d\boldsymbol{H}} \cdot \boldsymbol{H}^{\mathbf{I}} + \frac{1}{2} R_2(\boldsymbol{H})\, I_0. \tag{4.6}$$

The $R^{n\mathrm{f}}$ terms refers to the the n-th harmonic component of the resistance, corresponding to the oscillation frequency compared to the fundamental frequency of the injected AC current. We also note that for the last simplification in Eq. 4.4, we assume that $\boldsymbol{H}^{\mathbf{stat}}$ does not change with the current. This is only true to a first approximation, as the effective field of the magnetic anisotropy, which is part of $\boldsymbol{H}^{\mathbf{stat}}$, depends on $\boldsymbol{m}$. The direction of the magnetization $\boldsymbol{m}$, itself is affected by the current through $\boldsymbol{H}^{\mathbf{I}}$, however. The different harmonics can be measured individually

using lock-in detection, in which the current $I(t) = I_0 \cos \omega t$ is taken as a reference to reliably extract the signals with frequency $n\omega$ that are in phase with the injected current. Since the measurement of the 0th-harmonic R^{0f} is typically riddled with noise, we will focus on how to analyze and simulate the first harmonic resistance R^{1f} and the second harmonic resistance R^{2f}.

4.2.1. First Harmonic Resistance Analysis

The first harmonic $R^{1f} = R(\boldsymbol{H}^{\mathbf{stat}})$ encompasses the entirety of the MR excluding non-linear effects that scales with the current as it only reflects the changes in the resistance as a response to the static field $\boldsymbol{H}^{\mathbf{stat}}$. $\boldsymbol{H}^{\mathbf{stat}}$ in our case is comprised of the external field $\boldsymbol{H}^{\mathbf{ext}}$, demagnetizing field $\boldsymbol{H}^{\mathbf{dem}}$, magnetocrystalline anisotropy $\boldsymbol{H}^{\mathbf{cub}}$ and uniaxial anisotropy in the plane $\boldsymbol{H}^{\mathbf{u}}$. The MR effects that can enter R^{1f} and their magnetization dependence have already been discussed for general cases in Chapter 3. Here, we describe the phenomenological magnetization dependence of the resistance and show how different contributions to the MR can be separated. We start with the general expression of the longitudinal and transverse resistance, followed by the resistance including crystalline effects and spin-orbit fields for in-plane magnetized epitaxial thin films.

First Harmonic Longitudinal Resistance The longitudinal resistance for a polycrystalline sample in its general form can be written as,

$$R_{\mathrm{L}}^{1f} = R_{\mathrm{L}}^{x} m_{x}^2 + R_{\mathrm{L}}^{y} m_{y}^2 + R_{\mathrm{L}}^{z} m_{z}^2, \tag{4.7}$$

where $R_{\mathrm{L}}^{x/y/z}$ correspond to the resistance measured for $\boldsymbol{m}$ along the specified axis. Although there may be higher order terms, we saw no indications of their contribution in our systems, and so neglect them in this model. Eq. 4.7 describes the MR well

but it is often more meaningful to describe the MR in terms of the relative change of the resistance compared to a well defined and measurable offset, which we get by grouping the terms differently, namely

$$R_{\mathrm{L}}^{1\mathrm{f}} = R_{\mathrm{L}}^{\mathrm{z}} + (R_{\mathrm{L}}^{\mathrm{x}} - R_{\mathrm{L}}^{\mathrm{z}})\, m_{\mathrm{x}}^2 + (R_{\mathrm{L}}^{\mathrm{y}} - R_{\mathrm{L}}^{\mathrm{z}})\, m_{\mathrm{y}}^2. \tag{4.8}$$

Here we chose the grouping to end up with two terms, the first term $\propto m_{\mathrm{x}}^2$ includes all MR effects that are insensitive to rotations of $\boldsymbol{m}$ around $\boldsymbol{x}$ or $\boldsymbol{j}_{\mathbf{c}}$, while contributions covered by the second term are insensitive to rotations of $\boldsymbol{m}$ around $\boldsymbol{y}$. Consequently, $(R_{\mathrm{L}}^{\mathrm{x}} - R_{\mathrm{L}}^{\mathrm{z}})\, m_{\mathrm{x}}^2$ is typically associated with the classical AMR [5] whereas the contributions to the second term $(R_{\mathrm{L}}^{\mathrm{y}} - R_{\mathrm{L}}^{\mathrm{z}})\, m_{\mathrm{y}}^2$ can include spin-current-induced effects and structural effects. Among the spin-current-induced effects are the SMR [28], AHMR [34], while structure related effects include anisotropic interface MR [30] and geometric size effect [35], which both can also be ascribed to crystalline textures [36]. These two components of $R_{\mathrm{L}}^{1\mathrm{f}}$ can be easily separated in ZX- and ZY-angle scans, in which the magnetization is rotated in the indicated plane by a rotating $\boldsymbol{H}^{\mathbf{ext}}$. For rotations in the film plane, i.e. XY-scans, which are often used for the quantification of the second harmonic resistance, the expression simplifies down to

$$R_{\mathrm{L}}^{1\mathrm{f}} = R_{\mathrm{L}}^{\mathrm{y}} + (R_{\mathrm{L}}^{\mathrm{x}} - R_{\mathrm{L}}^{\mathrm{y}})\, m_{\mathrm{x}}^2 \tag{4.9}$$

Not only do these three angle scans allow for the separation of effects with different angle dependencies, the ratio of the amplitudes for different angle scans is often used as a good indicator of what MR effects are actually present in the system.

First Harmonic Transverse Resistance The transverse resistance in our thin films is characterized by two distinct terms, namely

$$R_{\mathrm{H}}^{1\mathrm{f}} = R_{\mathrm{H}}^{\mathrm{xy}} m_{\mathrm{x}} m_{\mathrm{y}} + R^{\mathrm{ahe}} m_{\mathrm{z}}. \tag{4.10}$$

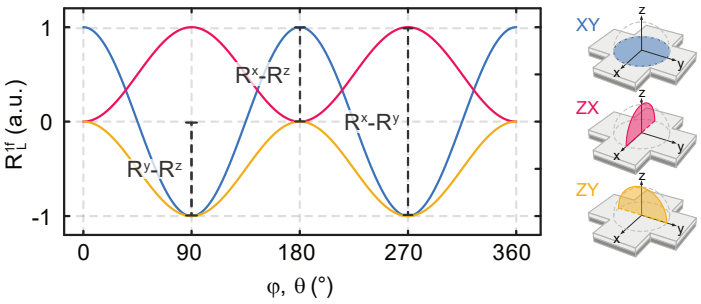

Figure 4.2.: The angle dependence of the longitudinal resistance can be mapped out using *XY*-, *ZX*- and *ZY*-scans, where the magnetization is rotated in the respective plane, as shown on the right. For the calculated signal shown here, we chose $R_L^x = 1$, $R_L^y = -1$ and $R_L^z = 0$, which demonstrates the typical $\cos^2$ shape observed in angle scans.

R_H^{xy} describes the amplitude of the transverse magnetoresistance for rotations of $\boldsymbol{m}$ in the xy-plane, which is often associated with the planar Hall effect (PHE). Similar to the longitudinal case though, spin-current-induced effects and structural effects can also contribute to the amplitude of the in-plane component of R_H^{1f}. Since R_H^{xy} and $(R_L^x - R_L^y)$ are just the transverse and longitudinal manifestations of the same effects, the resistivity values ρ_H^{xy} and $(\rho_L^x - \rho_L^y)$ must be equal. The resistances can differ however, depending on the device geometry leading to the relationship $R_H^{xy} = (R_L^x - R_L^y)\, w/l$, where w and l are the width and length of the main channel, respectively.

In contrast to that, there is no ambiguity about the sources of the second term of Eq. 4.10, as it is entirely comprised of the AHE [56]. The measurement of the AHE is best achieved with out-of-plane hysteresis loops, where a perpendicular external field is swept from $-H^{ext}$ to H^{ext}. Compared to *ZX*- or *ZY*-scans, in such

hysteresis loops, one sees more clearly whether the external field was strong enough to saturate the magnetization out-of-plane or not, which is critical for the correct measurement of the AHE. As we are applying an out of plane field in this geometry, the ordinary Hall effect (OHE) will contribute a signal $\propto H^{\text{ext}}$ that overlaps with the AHE. However, the contribution of the OHE can be isolated and then removed by applying external fields well past the saturation of the AHE.

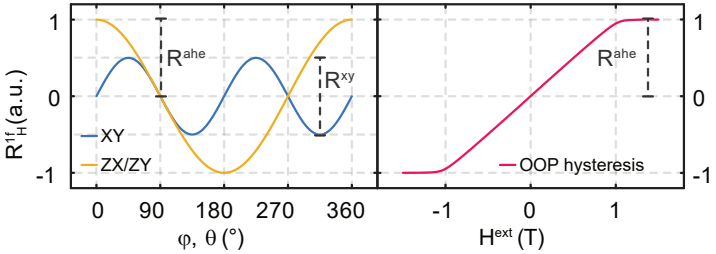

Figure 4.3.: The transverse signal of the magnetoresistance displays a $m_x m_y$-dependence and a m_z-dependence. The former is isolated in XY-scans, where the amplitude of the change in the resistance R^{xy} corresponds to the amplitude $(R_L^x - R_L^y)$ observed in the longitudinal system. The out-of-plane angle scans on the other hand are dominated solely by the AHE. Since the accurate measurement of the AHE requires the magnetization to be fully saturated out-of-plane, we measure it with out-of-plane hysteresis loops instead, where it is easier to discern whether the magnetization is saturated or not.

With Eq. 4.8 and Eq. 4.10 we have expressions for the resistance that apply to the usual case of polycrystalline thin films. However, in epitaxial systems, these expressions need to be modified

slightly to properly describe the CMR.

Crystalline Longitudinal Magnetoresistance In epitaxial thin film systems the XY-scan is especially well suited to identify effects induced by the crystal structure for two reasons. First, the additional symmetry breaking along the z-axis in thin films does not have an effect. Secondly, the magnetization can easily be saturated in the plane, meaning that there is no need to apply very high external fields, which can suppress the influence of weaker effective fields, such as the SOTs. The first harmonic including the interfacial CMR becomes [63]

$$R_{\mathrm{L}}^{1\mathrm{f}} = R_{\mathrm{L}}^{0} + b\cos^2(\varphi) - \frac{b-c}{2}\cos(2\alpha)\cos\left(2\left(\varphi-\alpha\right)\right), \tag{4.11}$$

where b and c are the CMR parameters, which govern the symmetry and strength of the CMR. This expression can be naively understood as Eq. 4.9, where $b = (R_{\mathrm{L}}^{\mathrm{x}} - R_{\mathrm{L}}^{\mathrm{y}})$, with an added m_{x}^2 contribution that is phase shifted by α.

Since the two terms share the same 2φ-dependence, the magnetization dependence of the total resistance $R_{\mathrm{L}}^{1\mathrm{f}}$ will also display a 2φ-dependence. In particular we can combine them and rewrite Eq. 4.11 as

$$R_{\mathrm{L}}^{1\mathrm{f}} = R_0(\alpha) + R_{\mathrm{L}}^{\mathrm{cmr}}(\alpha)\cos^2\left(\varphi - \Delta\varphi_{\mathrm{L}}(\alpha)\right), \tag{4.12}$$

where $R_{\mathrm{L}}^{\mathrm{cmr}}$ is the α-dependent amplitude

$$R_{\mathrm{L}}^{\mathrm{cmr}} = \frac{\sqrt{b^2 + c^2 - (b^2 - c^2)\cos(4\alpha)}}{\sqrt{2}} \tag{4.13}$$

and $\Delta\varphi$ is the resulting phase shift

$$\Delta\varphi_{\mathrm{L}} = -\frac{1}{2}\arctan\left(\frac{(b-c)\sin(4\alpha)}{b+c-(b-c)\cos(4\alpha)}\right). \tag{4.14}$$

This combined expression is helpful in analyzing the data, as $R_{\mathrm{L}}^{\mathrm{cmr}}$ is immediately available to us from a single angle scan, whereas Eq. 4.11 is not useful until a whole set of data for different device rotations α has been collected. From the α-dependence of $R_{\mathrm{L}}^{\mathrm{cmr}}$, which hints at the underlying crystalline effects due to its tendency to reflect their symmetry, the CMR parameters b and c can be retrieved.

Crystalline Transverse Magnetoresistance As usual, there is a transverse equivalent to the longitudinal CMR

$$R_{\mathrm{H}}^{1\mathrm{f}} = \frac{b}{2}\sin(2\varphi) - \frac{b-c}{2}\sin(2\alpha)\cos(2(\varphi-\alpha)). \tag{4.15}$$

Similar to Eq.4.11, there are two terms contributing to the CMR signal. The first term corresponds to the classical MR, which is seen in polycrystalline systems, and the second term contributes a phase-shifted signal with a α-dependent amplitude. Like the longitudinal resistance Eq.4.15, can be reduced to a more accessible form, which we will use to analyze the data, particularly

$$R_{\mathrm{H}}^{1\mathrm{f}} = \frac{R_{\mathrm{H}}^{\mathrm{cmr}}(\alpha)}{2}\sin(2[\varphi - \Delta\varphi_{\mathrm{H}}(\alpha)]), \tag{4.16}$$

where the amplitude of the combined terms is expressed as

$$R_{\mathrm{H}}^{\mathrm{cmr}} = \frac{\sqrt{b^2 + c^2 + (b^2 - c^2)\,\cos(4\alpha)}}{\sqrt{2}}, \tag{4.17}$$

and the resulting phase shift is

$$\Delta\varphi_{\mathrm{H}} = \frac{1}{2}\arctan\left(\frac{(b-c)\sin(4\alpha)}{b + c + (b-c)\cos(4\alpha)}\right). \tag{4.18}$$

Since this is the transverse manifestation of the CMR it contains the same information as the longitudinal CMR, making it valuable for validating the longitudinal measurements. However,

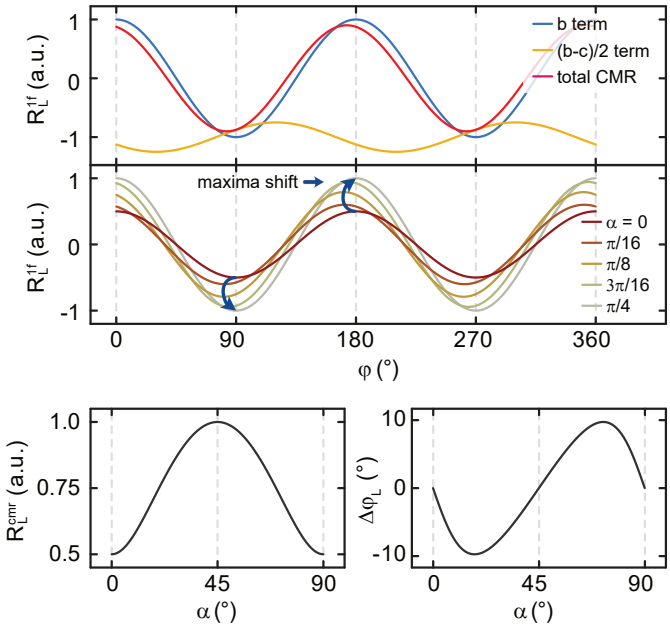

Figure 4.4.: Simulations of the CMR for $b = 1$ and $c = 0.5$ and the resulting amplitude R_L^{cmr} and phase shift $\Delta\varphi_L$. The CMR can be understood as a superposition of two contributions. One resembles the classical MR, displaying a constant $\cos^2\varphi$ dependence (blue), whereas the other contributes a phase shifted $\cos 2(\varphi - \alpha)$ signal (yellow) as shown in the top graph. The combination of the two leads to a 2φ dependent resistance (magenta), whose maxima shift as the angle α between the current and the crystal axes is varied, as shown in the middle graph. The α-dependence of the amplitude R_L^{cmr} (bottom left) and phase shift $\Delta\varphi_L$ (bottom right) exhibit the 4-fold symmetry imposed by the cubic crystal

compared to in the longitudinal case, the CMR parameters b and c extracted here will be scaled by w/l, as we have seen before for the transverse component of the AMR. Aside from letting us validate the CMR parameters obtained with the longitudinal resistance, $R_{\mathrm{H}}^{1\mathrm{f}}$ is required to characterize the SOTs more accurately, as it has a lower noise floor, and is essential to quantify the UMR.

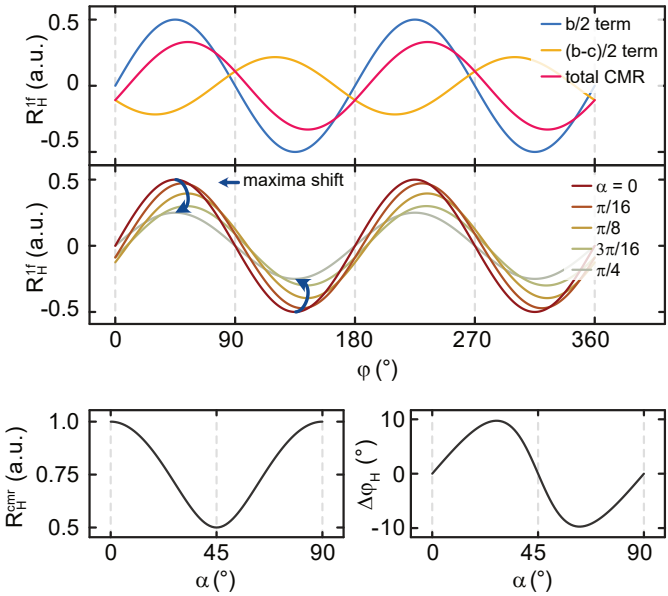

Figure 4.5.: The transverse CMR also is composed of a PHE-like signal (blue) and α shifted signal (yellow). Consequently the total signal (magenta) also phase-shifts and changes amplitude as the current is rotated w.r.t. to the crystal axes. If we track the maxima of the total signal (middle), we see that the amplitude (bottom left) and phase (bottom right) of this curve exhibit a 4-fold symmetry, reflecting the symmetry of the crystal.

Equation 4.12 and Eq. 4.16 lay bare a problem that plagues CMR measurements, which is the phase shift $\Delta\varphi_{\mathrm{L/H}}$. Looking at the expressions to evaluate the MR given in this section so far, we see that for each one, we need to know the direction of the magnetization. As $\boldsymbol{m}$ is not directly known to us, strictly speaking, it is common practice to conduct one of the angle scans with a very high external field, to guarantee that the magnetization is saturated along H^{ext}. Knowing that $H^{\mathrm{ext}} \parallel \boldsymbol{m}$, still does not reveal their direction with respect to the current, but that can be deduced with the symmetry of the resistance, which is normally assumed to follow the classical MR, namely Eq. 4.8 or Eq. 4.8. However, this procedure does not work with the CMR as the phase shift $\Delta\varphi_{\mathrm{L}}$ is inaccessible until the CMR parameters are known to us. Luckily, the CMR parameters can be calculated without precise knowledge of $\boldsymbol{m}$, as only the amplitude $R_{\mathrm{L}}^{\mathrm{cmr}}$ is needed, though multiple measurements at varying device rotations α are required. In this work we mapped out α in 45° steps starting at 0°, for which $\Delta\varphi_{\mathrm{L}} = 0°$, allowing us to avoid this problem. Nevertheless, this issue should be kept in mind when conducting MR studies on epitaxial or textured systems.

Now that we have the analytical expressions for the first harmonic resistances, for both crystalline and polycrystalline systems, we can approach the extraction of current-induced effects from the second harmonic resistance, which builds on the knowledge of $R^{1\mathrm{f}}$.

4.2.2. Second Harmonic Resistance

As shown in Eq. 4.6, $R^{2\mathrm{f}}$ consists of two terms, namely $\frac{1}{2}\frac{dR}{d\boldsymbol{H}} \cdot \boldsymbol{H}^{\mathbf{I}}$ that is related to the current-induced oscillation of $\boldsymbol{m}$ around its equilibrium position caused by $\boldsymbol{H}^{\mathbf{I}}$, and secondly $\frac{1}{2} R_2(\boldsymbol{H})\, I_0$, which contains thermoelectric effects and the UMR.

Thermoelectric Effects The thermoelectric effects that we need to take into consideration in our systems are the MTP, PNE and ANE, which are driven by thermal gradients ∇T. These gradients find their source in the injected current that can generate a substantial amount of heat via Joule heating. This is especially true for our thin films, since for the observation of appreciable SOTs, domain injection and domain wall motion, relatively high current densities in the range of 10^{10}-10^{11} A m^{-2} have to be applied to the main current channel of the device. This heat then either dissipates laterally into the contact pads, or perpendicularly into the substrate. The dissipation into these two heat sinks subsequently results in two thermal gradients that have been found to a strong electric signal, namely the in-plane gradient ∇T_x along $\boldsymbol{x}$ and the perpendicular gradient ∇T_z. Inserting these two gradients into the expressions of the thermoelectric effects yields for the longitudinal second harmonic signal

$$R_L^{th} = R^{mtp} m_x^2 - R^{ane} m_y \tag{4.19}$$

and for the transverse signal

$$R_H^{th} = R^{pne} m_x m_y - R^{ane} m_x, \tag{4.20}$$

Unidirectional Magnetoresistance As for the UMR, it also consists of multiple components, particularly the spin-dependent UMR and the spin-flip UMR as explained in Section 3.4.3. To find the expression of the spin-dependent UMR we need to determine the direction of the spin polarization $\boldsymbol{\sigma}$ with the respect to $\boldsymbol{m}$. Usually, the spin current generated in both HM/FM bilayers as well as FM layers has spin polarizations $\boldsymbol{\sigma}$ parallel to $\boldsymbol{y}$. For the spin-dependent UMR it then follows that

$$R^{umr} = -R^{sd-umr} m_y \tag{4.21}$$

which represents the lowering of the resistance for parallel alignment of $\boldsymbol{\sigma}$ and $\boldsymbol{m}$.

The magnetization direction dependence of the spin-flip UMR is not as easily predicted however. In the first experimental observation of the sf-UMR, its symmetry was found to deviate from the m_y dependence, showing a more complex magnetization dependence instead [77], owing to the anisotropy of the magnon excitation using spin currents. Nevertheless, this component can be separated from the sd-UMR by exploiting its current and field dependence, instead of predicting the magnon anisotropy.

In any case, while the sf-UMR is strong in HM/FM bilayers, in crystalline FM layers it seems too weak to be measured according to our observations, as we will present in Chapter 6.

Current-induced Torques Lastly, we need to unravel the only remaining part of the second harmonic resistance. As we already mentioned, the current-induced fields cause the magnetization to oscillate around $\boldsymbol{H}^{\mathbf{stat}}$, which modulates the first harmonic resistance in sync with the current. The strength of R^{2f} can be understood as the amplitude of this oscillation. Naturally, R^{2f} will increase with the amplitude of the induced fields H^{I}, as this leads to larger changes in $\boldsymbol{m}$. On the other hand, the signal also depends on the sensitivity of the first harmonic resistance to changes in $\boldsymbol{m}$ around the static field $\boldsymbol{H}^{\mathbf{stat}}$, as is encapsulated in its expression

$$R^{2f}(\boldsymbol{H}^{\mathbf{I}}) = \frac{1}{2}\frac{dR}{d\boldsymbol{H}} \cdot \boldsymbol{H}^{\mathbf{I}}. \tag{4.22}$$

The sensitivity of the resistance to changes in the direction of $\boldsymbol{H}^{\mathbf{I}}$ can be linearly approximated, giving us

$$R^{2f} \approx \frac{R(\boldsymbol{H}^{\mathbf{stat}} + \boldsymbol{H}^{\mathbf{I}}) - R(\boldsymbol{H}^{\mathbf{stat}} - \boldsymbol{H}^{\mathbf{I}})}{2}. \tag{4.23}$$

This expression allows us to calculate the second harmonic response given that we have fully characterized R^{1f} and can precisely determine $\boldsymbol{m}$ for any specific $\boldsymbol{H}^{\mathbf{stat}} \pm \boldsymbol{H}^{\mathbf{I}}$.

With the full expression of the first harmonic resistance and a simple method to calculate the second harmonic, we are fully prepared to successfully analyze our magnetotransport measurements, bar the last piece of the puzzle. Every calculation shown above assumes that we know the total effective field $\boldsymbol{H}$ and thus know the direction of the magnetization. Whereas we do have relatively good control over the magnetization via $\boldsymbol{H}^{\mathbf{ext}}$, the rest of the effective fields acting on the magnetization, such as the anisotropies and damping-like SOT, depend on $\boldsymbol{m}$ themselves. We can unwind this entanglement by approximating the magnetization of our films with a macrospin model, and calculate $\boldsymbol{m}$ for known external fields, anisotropies and SOTs.

4.3. Macrospin Simulations

The crux of the macrospin model is that the magnetization is considered to be uniform and act as a single unit, whose interaction with its environment is described by the LLG equation, namely

$$\frac{\partial \boldsymbol{m}}{\partial t} = -\frac{\gamma}{1+\alpha_{\mathrm{d}}^2}\, \boldsymbol{m} \times \boldsymbol{H} - \frac{\gamma \alpha_{\mathrm{d}}}{1+\alpha_{\mathrm{d}}^2}\, \boldsymbol{m} \times (\boldsymbol{m} \times \boldsymbol{H})\,, \tag{4.24}$$

where γ is the gyromagnetic ratio and α_{d} is the dimensionless damping factor. The effective field $\boldsymbol{H}$ that enters this expression again consists of the induced fields $\boldsymbol{H}^{\mathbf{I}}$ and the static fields $\boldsymbol{H}^{\mathbf{stat}}$. The dynamic component $\boldsymbol{H}^{\mathbf{I}}$ contains the Oersted field ($\boldsymbol{H}^{\mathbf{oe}}$), field-like SOT ($\boldsymbol{H}^{\mathbf{fl}}$) and damping-like SOT ($\boldsymbol{H}^{\mathbf{dl}}$), while the static component $\boldsymbol{H}^{\mathbf{stat}}$ consists of the external field ($\boldsymbol{H}^{\mathbf{ext}}$),

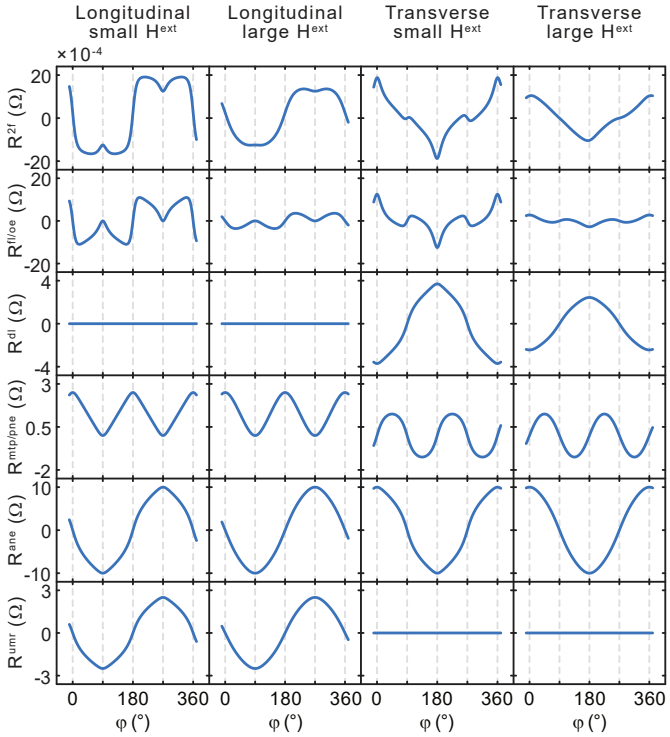

Figure 4.6.: Overview of the XY-scan R^{2f} signal for large ($H^{ext} \gg H^{cub}$) and small ($H^{ext} \approx H^{cub}$) external fields for cubic systems with magnetocrystalline anisotropy along $\varphi = 0°, 90°, 180°, 270°$. To separate these effects, we mostly make use of their magnetization dependence. However, R^{dl}, R^{ane} and R^{umr}, have a very similar symmetry, such that the magnetization dependence does not suffice to separate these effects. Instead, we exploit the fact that the signal of the damping-like SOT R^{dl} scales with the external field and R^{umr} does not appear in the transverse component of the resistance.

effective demagnetizing field ($\boldsymbol{H}^{\mathbf{dem}}$), uniaxial in-plane anisotropy ($\boldsymbol{H}^{\mathbf{u}}$) and the cubic anisotropy ($\boldsymbol{H}^{\mathbf{cub}}$). Combining all these contributions, the effective field results in

$$\begin{aligned}\boldsymbol{H} = &\left(H^{\mathrm{oe}} + H^{\mathrm{fl}}\right)\begin{pmatrix}0\\1\\0\end{pmatrix} + H^{\mathrm{dl}}\begin{pmatrix}\cos\theta\\0\\-\cos\varphi\end{pmatrix} + H^{\mathrm{ext}}\begin{pmatrix}h_{\mathrm{x}}^{\mathrm{ext}}\\h_{\mathrm{y}}^{\mathrm{ext}}\\h_{\mathrm{y}}^{\mathrm{ext}}\end{pmatrix}\\ &+H^{\mathrm{dem}}\begin{pmatrix}0\\0\\\cos\theta\end{pmatrix} + H^{\mathrm{u}}\begin{pmatrix}\cos\beta\,\sin\theta\,\cos\varphi-\beta\\\sin\beta\,\sin\theta\,\cos\varphi-\beta\\0\end{pmatrix}\\ &+H^{\mathrm{cub}}\begin{pmatrix}\cos\alpha\,\sin^3\theta\,\cos^3(\varphi-\alpha)+\sin\alpha\,\sin^3\theta\,\sin^3(\varphi-\alpha)\\\sin\alpha\,\sin^3\theta\,\cos^3(\varphi-\alpha)+\cos\alpha\,\sin^3\theta\,\sin^3(\varphi-\alpha)\\\cos^3\theta\end{pmatrix},\end{aligned} \tag{4.25}$$

where $h_{\mathrm{i}}^{\mathrm{ext}}$ corresponds to the directional cosines of the external field and β is the angle between the uniaxial anisotropy axis and $\boldsymbol{j}_{\mathbf{c}}$. As was mentioned before, the LLG describes a precession *around* $\boldsymbol{H}$ and a damping motion *towards* $\boldsymbol{H}$. Since, for the harmonic voltage analysis, we are only interested in the equilibrium position of the magnetization, we can ignore the precession term and only consider the damping term. This reduces the required computing time and accelerates the convergence towards equilibrium.

Although we can now find the equilibrium position of the magnetization and thus $\boldsymbol{H}$ for any set of parameters, we are still left with the problem that we only know and control $\boldsymbol{H}^{\mathbf{ext}}$. The other contributions to the effective field are all part of the material parameters that we are attempting to characterize. In the next step, we will combine the first harmonic voltage analysis with the macrospin simulations to simultaneously calculate the MR and anisotropies. After that, we are ready to quantify the current-induced effects.

4.4. Data Analysis

Before we can start analyzing data, we need to measure a complete data set, suitable for the extraction of the MR, SOTs, etc. Most of the information we are seeking can be obtained from XY-scans, as we mentioned above. A single XY scan, however, is not sufficient to separate the SOTs and thermoelectric effects, as the main differentiator we rely upon for that is their H^{ext}-dependence. Consequently, if we know the H^{ext}-dependence, a full set of XY scans should comprise of at least two scans, one with a lower external field in the range of the in-plane anisotropies, and one with an external field strong enough to fully saturate the magnetization along $\boldsymbol{H}^{\mathbf{ext}}$. Additional XY-scans are not necessary, but would increase the precision of the analysis. The in-plane scans need to be complemented with an out-of-plane hysteresis loop, which gives access to the demagnetizing field and the AHE. Here, we have to make sure that $\boldsymbol{H}^{\mathbf{ext}}$ sufficiently exceeds $\boldsymbol{H}^{\mathbf{dem}}$ to separate the AHE from the OHE.

First Harmonic Resistance Fit We apply an iterative fit to $R^{1\text{f}}$ that can be condensed down to two steps. First, we guess the strength of the anisotropies H^{dem} and H^{cub}, and in the case of $\boldsymbol{H}^{\mathbf{u}}$ we also guess a direction, and solve the LLG equation numerically for each $\boldsymbol{H}^{\mathbf{ext}}$ using an adaptive Runge-Kutta method, giving us the equilibrium direction of the magnetization $\boldsymbol{m}$. Given appropriate starting conditions, the solver converges relatively fast and never results in a meta-stable solution. The second step is to fit the MR for the calculated $\boldsymbol{m}$ to the $R^{1\text{f}}_{\text{L/H}}$ data using linear regression and the appropriate expression of the resistivity, such as Eq. 4.12 and Eq. 4.16.

With this fitting methodology, we can fully quantify H^{cub}, $\boldsymbol{H}^{\mathbf{u}}$, and in terms of the MR we will obtain $R^{\text{cmr}}_{\text{L/H}}$ from a set of XY-scans.

H^{dem} and R^{ahe} can be obtained from an out-of-plane hysteresis loop. Finally, from the α-dependence of $R^{\mathrm{cmr}}_{\mathrm{L/H}}$ we can calculate the CMR parameters b and c and with these parameters we can retrieve $\Delta\varphi$.

Second Harmonic Resistance Fit Now that we have fully characterized the MR and the anisotropies, we can continue with second harmonic signal of the XY-scans measured for different amplitudes H^{ext}. The aim here is to quantify the SOTs, thermoelectric effects and the UMR. The analysis of the second harmonic is also done in an iterative fit where we first solve the LLG for guessed set of parameters, in this case the dynamic field $\boldsymbol{H}^{\mathbf{I}}$, and then fit the rest of the parameters using linear regression.

Specifically, we first take a guess at $\boldsymbol{H}^{\mathbf{I}}$ and solve the LLG for $\boldsymbol{H} = \boldsymbol{H}^{\mathbf{stat}} + \boldsymbol{H}^{\mathbf{I}}$ and $\boldsymbol{H} = \boldsymbol{H}^{\mathbf{stat}} - \boldsymbol{H}^{\mathbf{I}}$. The signal generated by the current-induced torques is then calculated with Eq. 4.23. The SOT signal is then subtracted from the R^{2f} data, after which the thermoelectrical effects and UMR remain in the data. As the UMR does not appear in the transverse signal $R^{\mathrm{2f}}_{\mathrm{H}}$, we can fit this data with Eq. 4.20 using linear regression. From this iterative fit, we obtain $H^{\mathrm{fl/oe}}$, H^{dl} and the parameters of the thermoelectric effects R^{ane} and R^{pne}.

As a last step, we will isolate the UMR signal contained in $R^{\mathrm{2f}}_{\mathrm{L}}$. For this, we need to remove the SOT signal and the thermoelectric signal, using the SOT signal that is already available to us from the iterative fit. For the thermoelectric signal, we need to transpose the transverse PNE and ANE, which is achieved by scaling the parameters obtained from the fit of the transverse signal by the length-to-width ratio l/w or the ratio of the CMR parameters retrieved from the longitudinal and transverse measurements, i.e. $b_{\mathrm{L}}/b_{\mathrm{H}}$ or $c_{\mathrm{L}}/c_{\mathrm{H}}$. These factors are nominally the same, however, usually the latter two are more accurate, as they include

device deviations from which the thermoelectric effects will also suffer. Once the SOT signal and thermoelectric effects have been removed from R_L^{2f}, any remaining angle dependencies in the residual of the fit can be assigned to the UMR.

4.5. Magnetic Microscopy

Although a large part of this thesis has involved the use and modelling of magnetotransport effects, for new effects the unambiguous imaging of the magnetic state itself is particularly useful. To this end, we make use of microscopy techniques to image the magnetic state of our systems, and thus to visualize and further understand the unique effects that arise in thin films, specifically the chiral coupling. We make use of three microscopy techniques: X-ray photoemission electron microscopy and magnetic force microscopy (MFM) to image the magnetic state of chirally coupled nanomagnets and magneto-optic Kerr effect (MOKE) microscopy to image the SOT-driven domain nucleation in DW conduits in Chapter 7.

The three different techniques are used for different systems, and to address different scientific questions, based on our scientific requirements.

4.5.1. X-ray Photoemission Electron Microscopy

For the imaging of the chirally coupled nanomagnets discussed in Chapter 7, we require a resolution on the order of tens of nanometers. To achieve this, we turned to the well-established technique, X-PEEM, which is a photon-in, electron-out technique that makes use of X-rays produced by a synchrotron source [82–84]. Specifically, the sample is illuminated by a collimated beam of high brilliance, monochromatic X-rays, which results

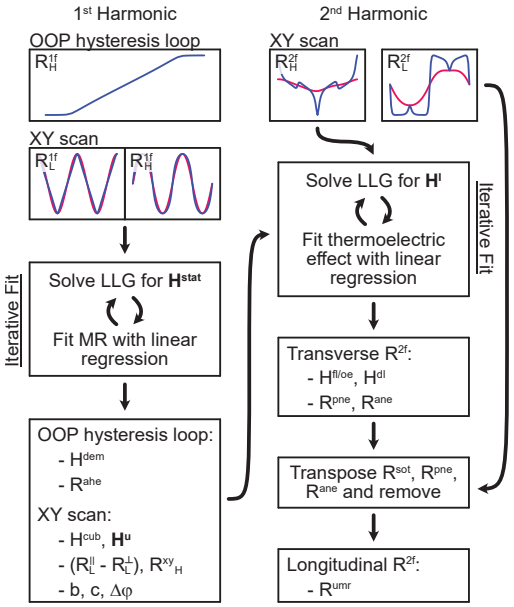

Figure 4.7.: Overview of the fitting procedure outlining which parameters are extracted from which signal. R^{1f} is fitted with an iterative fit, where we solve the LLG equation for a guessed $\boldsymbol{H}^{\mathbf{stat}}$ and then use the calculated $\boldsymbol{m}$ to fit the MR parameters via linear regression. For R_{H}^{2f} we also apply an iterative fit, where we first solve the LLG equation with a guessed $\pm\boldsymbol{H}^{\mathbf{I}}$. From this calculation and the MR parameters we can evaluate R^{sot}. This is removed from the R_{H}^{2f} and from the residual we can extract the thermoelectric effects with linear regression. Finally, we transpose the transverse signal of the SOTs and thermoelectric effects and remove it from R_{L}^{2f}. The residual can be analyzed for the UMR.

in the photo-emission of secondary electrons. These secondary electrons are collected from the surface by the application of a high voltage, and the spatial variations in the electron emission are resolved using an electron microscope. PEEM is intrinsically a surface-sensitive technique since the photo-emitted electrons originate from the top $\propto 5\,\text{nm}$ of the material.

To gain sensitivity to the magnetization, we tune the energy of the X-rays to the absorption edge of our element, in this case the Co L_3 edge, and use circularly polarized light to probe the X-ray magnetic circular dichroism (XMCD). The XMCD is an effect where the angular momentum of the incoming photons, $\pm\hbar$ parallel to the direction of light for circular positive and negative polarizations, couples to the spin angular momentum of the electrons of a magnetic material via spin-orbit coupling. As a result, there is a difference in the absorption of positive and negative circular polarized X-rays due to the imbalance of spin-up and spin-down electrons in the valance band. Thus, the XMCD provides an element specific directional probe of the magnetization of a magnetic material.

By combining XMCD with X-PEEM, where we measure high resolution X-PEEM images with both circular polarizations, and take the difference to isolate the magnetic contribution, we can obtain a high spatial resolution image of the component of the magnetization parallel to the X-ray beam. In the Swiss Light Source, where we performed the measurements, the X-rays are incident on the sample at a shallow angle of 16°, meaning that XMCD-PEEM images are mostly sensitive to the in-plane component of the magnetization.

4.5.2. Magnetic Force Microscopy

Although X-PEEM is a very effective technique for directly imaging the surface magnetization of a sample, one drawback is its

availability: Synchrotron beamtime is a very valuable and highly competitive resource that is only available for up to a week every six months through the writing of beamtime proposals. As a result, we supplement our X-PEEM results with a lab-based microscopy technique that also offers access to the magnetic state of a system with the required spatial resolution, namely MFM [84, 85].

In contrast to X-PEEM, which exploits light-matter interactions, MFM is a form of atomic force microscopy that involves the scanning of a sharp tip at the end of a cantilever over the surface of a sample. In the case of MFM, the tip is coated with a magnetic material, allowing for the stray magnetic fields emitted from the surface of the sample to be probed. Specifically, the cantilever oscillates at a resonance frequency. This frequency shifts in the presence of a force, which in this case is due to gradients in the magnetic field. In this way, magnetic field gradients can be imaged with resolutions on the order of tens of nanometers - where the spatial resolution is determined by the lateral size of the tip. For samples with out-of-plane magnetization, the positive and negative charges on the sample surface induced by the magnetization result in negative and positive magnetic field gradients, respectively. In this case, as used in this work, MFM results in a clear mapping of magnetic field gradients that map out the magnetic domains present.

4.5.3. Wide-Field Magneto-optic Kerr Effect

While MFM has a very high spatial resolution it suffers from slow acquisition times. Although this is not a problem for static imaging, for measurements of domain wall propagation it is more convenient to use a faster technique, such as MOKE microscopy [38, 86]. In MOKE microscopy, similar to X-PEEM, we probe light-matter interaction, however this time via a photon-in photon-out

mechanism, where the direction of the magnetization results in a slight rotation of the linear polarization of the laser light incident on the sample. As MOKE is an optical technique, it has a lower spatial resolution than X-PEEM and MFM of the order of hundreds of nanometers, depending on the wavelength of the light. For the domain wall conduit structures, this is not an issue, as the structures are micrometers in size.

In particular, to probe thee rotation of the polarization, the laser light is first linearly polarized by a polarizer before it reflects off the sample. Through the interaction with the magnetization, the linear polarization is slightly rotated. The strength of the rotation is determined by the direction of the magnetization with the respect to the polarization. The reflected light then passes through an analyzer, which filters according to the polarization set by the polarizer, and hits a photodiode. The result of this is a magnetization dependent signal that can be used to determine the magnetization direction. Depending on which component of the magnetization we are interested in, we either measure in the polar or longitudinal geometry, which reveal the OOP and the IP component parallel to the propagation direction of the light, respectively.

In this thesis, we use the MOKE for domain imaging, for which we illuminate the whole area of interest at once, instead of using a scanning laser. While the wide-field MOKE microscope is provides us with the spatial and time resolution required to observe DW propagation, topographic information usually dominates the recorded images. To increase the magnetic contrast, we measure differential images, where the image of the current magnetization state is subtracted from a reference image, taken of a known magnetization state. This highlights changes in the magnetization and removes topographic information, allowing for the magnetic domains to be mapped.

5. Sample Fabrication

In this chapter we will detail the growth and patterning of the FM/Ox systems studied in this work, which entails the deposition methods, techniques to control the oxidation and lithography procedures. This chapter aims to give an overview of the fabrication techniques used and the considerations that need to be taken into account in the process. The detailed guides about the fabrication of epitaxial Fe and Pt/Co/AlO_x systems can be found in Appendix A.

5.1. Fabrication Methods

5.1.1. Film growth

We mainly employ three deposition techniques in this work to grow our films, i.e. thermal evaporation, molecular beam epitaxy and sputtering. Here we will quickly discuss each technique and provide motivation for their use in this work.

Thermal Evaporation Deposition via thermal evaporation is based on the sublimation or evaporation of the material in vacuum ($< 10^{-6}$ mbar). For this the material is indirectly heated in a tungsten metal boat which is in turn resistively heated. While this allows for the deposition of a variety of FMs, the relatively low vacuum and reactivity with the tungsten boats limits the quality of the films achieved using this method. Nevertheless, the low preparation overhead, high deposition rates of several

nm/min and, on a practical level, availability makes this a good candidate for the deposition of Cr/Au contact pads.

Molecular Beam Epitaxy Similar to the deposition using thermal evaporation, with MBE we also either sublimate or evaporate by heating up the source material. However, MBE requires ultra high vacuum ($< 10^{-10}$ mbar) and does not necessarily imply the use of metal crucibles for evaporation. Because of the UHV, we can work with growth rates of a few Å/min with little to no risk of decontamination of the sample surface or the deposited material. The slow deposition process combined with in-situ annealing allows for the growth of single crystal films. This was used in this work to grow epitaxial single layer FMs such as MgO(001)/Fe. Other than for depositing metals, which is relatively straightforward, we also use MBE to deposit metal oxides. Although it is possible to deposit these oxides straight from an oxide source, we opted to grow them reactively, meaning that we deposit the metal in an oxygen atmosphere ($\approx 10^{-7}$ mbar). One aspect of MBE that we have not explored in this work, but seen the effect of, is the directional growth, which can induce magnetic anisotropy in the grown films. As this anisotropy is dependent on the incident angle of the beam of atoms emitted from the source, great care has to be taken to keep the deposition angles consistent.

The film quality achievable by MBE comes at the cost of long deposition times, large preparation overhead and the requirement for UHV. The low deposition rate realistically limits the growth to thin films of a few nm thickness and the UHV restricts the use of organic resist masks to deposit patterned layers. If we compromise the UHV to use organic resist masks, shadowing effects due to the directional growth has to be considered. As a result we use MBE exclusively to grow epitaxial FM/Ox stacks.

Sputtering Unlike in the previous techniques, with sputtering, the material is forcefully ejected from the target source by collision with high energy ions. The source of these ions, in our case Ar^-, is a radio frequency powered plasma that is maintained on the target. Maintaining this plasma requires an argon atmosphere with pressures in the mbar range. This process can yield relatively high growth rates for metals, but, for our purposes, we target lower and sub-nm/s rates to achieve better thickness control. For the growth of metal oxides, AlO_x specifically, we again opted to use a metal target and force the oxidation post growth. The oxidation is achieved using a process similar to sputtering, but instead of an argon plasma on the target, we apply an oxygen plasma on the sample.

Sputtering was applied for the fabrication of Pt/Co/Al(O_x) stacks, where precise oxidation of the Al layer is paramount for controlling the PMA.

The controlled growth of the desired material is only one step in the fabrication process as functional devices also heavily rely on precise patterning, which we will address next.

5.1.2. Electron Beam Lithography

Lithography in this context encompasses all steps required to fabricate a patterned mask that can be used to transfer a pattern onto a film on a sample. The procedure consists of the application of an organic resist to the sample, its subsequent exposure to some form of radiation and finally the development that reveals the pattern, as shown in Figure 5.1c-e. The lithography technique of choice here is electron beam lithography (EBL). As the name suggest, EBL employs a scanning electron beam, which, upon scattering on the resist and substrate, transfers energy to the resist. In the process the resist goes through a structural change, affecting its solubility. This technique allows for feature sizes

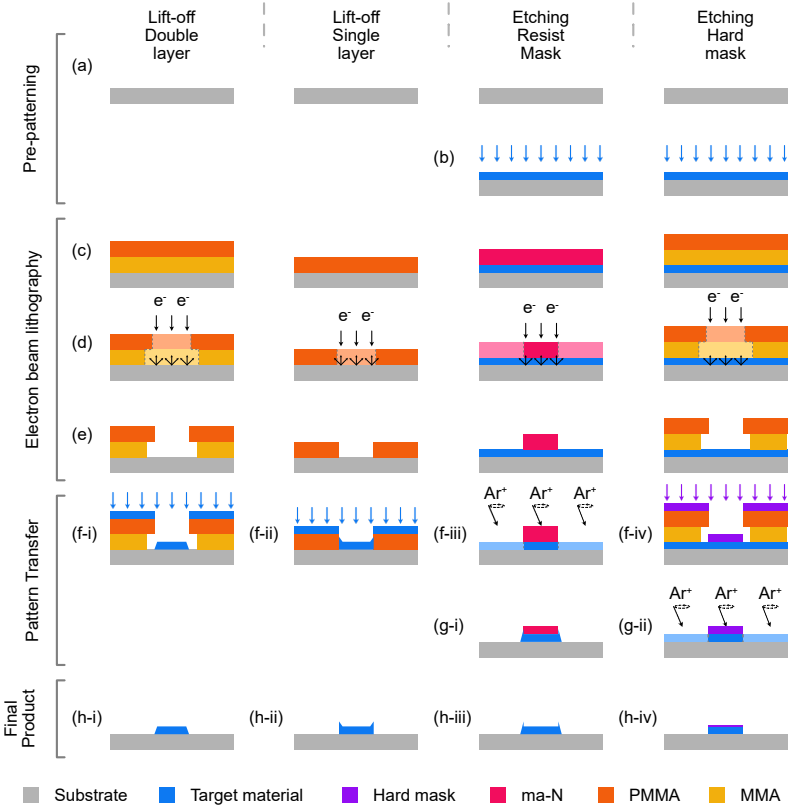

Figure 5.1.: Schematic illustrations of the four pattern transfer techniques used in this work. In the two lift-off processes, the target material is deposited on a already patterned mask, which transfers the pattern to the material. For the etching techniques the multilayer stack is first deposited as a full film and then etched, transferring the pattern of the resist mask or hard mask to the film.

down to a few tens of nanometers, but as a scanning method, it scales poorly with the area of the region that has to be exposed. Nonetheless, the design flexibility and achievable resolution with EBL are unmatched. The final quality of the patterned resist does not only depend on the exposure technique though, so for the rest of this section we will run through a general lithography step, and, on the way, point out the components that are at play in determining the end result.

As was mentioned, the first step in the process, other than substrate cleaning, is the application of a resist. The resist plays a critical role in determining the achievable resolution and overall fabrication and pattern design. In our case we worked with two resists, namely MMA/PMMA and ma-N 2403. The positive MMA/PMMA resists was chosen for its ease of use and high resolution, whereas the negative ma-N resist was used for its high etching resistance. The positive and negative labels describe their reaction to the exposure to the electron beam, akin to photographic film. In a positive resist, the exposure causes an increase in solubility and as a result the exposed resist dissolves during development. On the other hand, a negative resist has the opposite behavior and the solubility decreases due to the exposure. Thus, the exposed areas remain after development. As a consequence of effectively having to invert the exposed area to reach the same remaining pattern, the type of resist was chosen based on the pattern design, in an effort to limit exposure time to less than an hour.

Not only does the choice of resist impact the resulting quality of the devices, the application of the resist, i.e. spin coating, is as important. In this procedure, a droplet of resist is put in the center of the substrate, which is then rotated at several thousand rotations per minute, spreading the resist over the substrate. Spin coating results in very even resist thickness throughout the sample and through the rotation speed we can control the

thickness to a certain degree. As a last step before the exposure, the resist goes through a soft bake, where the substrate is heated in order to evaporate any solvent remaining in the resist.

During the exposure itself, the main factors contributing to the quality of the lithography are the current of the e-beam and the electron dose the resist is exposed to. When choosing the current used for the exposure we need to consider the beam size and the exposure time, which scale linearly and inversely with the current, respectively. Thus the goal is generally to minimize the current while maintaining practical exposure times. On the other side of the scale, if larger patterns are being exposed and resolution is not an issue, large currents can be used to cut down on the exposure time, but there are upper limits to the current such as the the maximal stepping frequency and, more critically, charging effects. Charging occurs on poor conductors where the charges from the e-beam build up, leading to a distortion of the incident beam or even spark discharges, which can damage the sample as well as the e-beam system.

The amount of charge, or the dose, required for proper exposure is a property specific to the resist and substrate combination used, although there is generally some leeway for adjustments depending on the design, e.g. depending on the overhang in the resist. Additionally, local adjustments to the exposure time have to be made to compensate for the proximity effect. The proximity effect is a result of the backscattering of the incident e-beam, which can occur at wide angles, effectively widening and blurring the focused beam. Thus not only the area hit by the beam is exposed but the surrounding area also receives some of the dose, which quickly adds up in densely packed patterns, requiring the previously mentioned decrease in exposure time. In this work, corrections to the exposure time per pixel due to proximity effect are taken into account at the stage of the design, using calculations done for preset model systems.

After the exposure, the resist is ready for the development. During the development we make use of the solubility change induced by the exposure and selectively dissolve the regions with lower solubility. Thus, choosing the right developer to maximize the selectivity and using the correct development time is of the utmost importance to preserve the precision of the exposed pattern. As a last optional step, the developed pattern can be hard baked, i.e. heated on a hot plate, with the goal to increase the performance of the resist in etching processes.

The developed resist can then be used with two types of processes to transfer the pattern onto the substrate, namely lift-off and etching, the difference between the two being at whether the material we aim to pattern was deposited before or after the lithography.

Patterning via Lift-off In the lift-off process we deposit the target material after the lithography step, i.e. on the resist mask and sample surface, which is analogous to using masking tape to paint in predefined areas. The resist mask serves as a temporary protection layer that we can easily remove after the deposition, including the material on top of it, leaving only the material deposited on the exposed surface. As we are filling in the areas with no resist, the patterned resist must be the inverse of the desired final pattern of the film. The whole patterning process via lift-off is depicted in Figure 5.1.

There are a few points we need to pay attention to in order to improve the quality of the layers patterned via lift-off. First is to ensure a clean surface. Some of the symptoms of this being an issue are poor wetting, unusually high roughness, high resistance and electrical devices that inconsistently break during electric measurements. Since a lithography step precedes the deposition, the open surface can be contaminated with some resist residues

after the development. Cleaning the surface after development, while leaving the mask intact is not a simple task as our options are limited. For thick and etch resistant resists, a short burst of plasma oxidation is a good option. If the resist is too fragile for plasma oxidation, increasing the development time and more rigorous rinsing can help.

Another problem typically faced are so called lift-off edges, where excess material piles up at the edges of the patterns. This issue is can be avoided if the resist overhangs, as shown in Figure 5.1. While overhangs can happen naturally in positive resist due to the backscattered electrons, we can purposefully create large overhangs by using two resist layers. The idea is to layer two resist with different solubility in the developer solvent, the top one having lower solubility. During the development the bottom layer will dissolve quicker and leaver the overhanging top layer. The combination of resists we use in this work is MMA/PMMA, both positive resists with very similar properties and required processing but enough of a different solubility to generate large overhangs.

Lastly, a suitable thickness for the planned deposition must be chosen. Ideally, the total resist thickness should be 2-3 times larger than the deposited film, as otherwise we run the risk of growing a continuous film making the lift-off impossible. Thicker resists are also needed with sputtering compared to evaporation techniques, since the high energy plasma used for sputtering can partially burn and remove the resist.

Lift-off processes are simple and cheap requiring no other special equipment other than the ones used for the lithography and deposition. Since it leaves the existing sample unchanged and only adds to it, this process is ideal to fabricate structural layers such as labels, alignment markers and contact pads. The patterning of electrical devices is possible but even after taking precautions we found the devices to be more sensitive and break

at lower applied currents.

Patterning via Etching The second process we use for patterning is etching. Unlike the lift-off process, which is additive, etching is subtractive, meaning we start with a full layer of the target material, protect the areas we want to keep with an etch mask and then etch the unwanted parts to obtain our pattern as shown in Figur 5.1. For the actual etching itself, we employ argon ion etching, a technique that sets itself apart by its ability to etch most materials at an efficient rate. The etching process is similar to sputtering, but the argon plasma is maintained in a source separate from the sample. Ar^+ ions are accelerated towards the sample, neutralized with electrons and on impact with the sample remove some material. The physical nature of this process makes it relatively agnostic towards the material that is being etched compared to chemical etching processes, scaling only slightly with the hardness of the material. However, the selectivity between most materials is low. Since we cannot use etch stop layers, i.e. layers of materials that have very low etch rate, to protect the layers beneath the ones we want to etch, we only use etching processes to etch all the way through to the substrate.

The low selectivity also means that the etch masks need to be adjusted accordingly. If we use the resist as our etch mask, we can increase the etch resistance by increasing the cross linking of the polymers. The techniques to increase cross linking are specific to the resist so no general process will work for all resists, but among the techniques used are hard baking and overexposure of the resist. A simpler approach to making the resist survive the etching process is to use thicker resist layers. Since the resist can just be removed by a solvent after the etching, having excess resist is not inherently a problem. Thick etch masks do come with

a caveat though, especially when the etching method used is very directional, as is the case in Ar ion beam etching. In the etching process we essentially sputter the target material, which can then redeposit on the resist and create a thin fence at the edge of the pattern, similar to lift-off edges mentioned before. To avoid this, we do not etch normal to the surface but at an angle, typically 30°, while the sample is rotated, which prevents the material from building up on the resist walls. This procedure has the drawback of causing shadowing effects though, because the tall resist wall will partially block the ion beam and prevent the shaded areas from being etched, causing the edges of the pattern to blur. These problems can be mended by optimizing the rotation speed and the etch angle, but can also be alleviated by using other materials as our etch mask, i.e. hard masks. Hard masks are patterned layers of etch resistant materials, which are fabricated via lift-off, as shown in Figure 5.1. The advantage of making hard masks is having a larger variety of available materials that can be used as etch masks to maximize the selectivity and reducing the problems that come with thick resist masks. The other side of the coin is that hard masks cannot be simply removed in a solvent but rather are designed to remain or be etched away.

In the last sections we covered every step of the device fabrication process and addressed general considerations that can be taken into account to improve the quality of the patterns. While in the end every specific sample system will require its own set of optimizations, the sections above should serve as a good overview and starting point to appreciate the intricacies of nanolithography. The fabrication of actual functional devices is a matter of combining the processes described above. For a full step-by-step description of the device fabrication recipes, see Appendix A.

6. Magnetotransport in Epitaxial Fe Single Layers

The study of magnetotransport in thin films has garnered a lot of attention in the field of spintronics, resulting in a rapidly growing compendium of phenomena. Looking back at the work that has been done, is hard to ignore the fact that a large portion of research has been focused on heavy metals, which due to their inherently strong spin-orbit coupling have shown to be excellent subjects to study. However, as time went on, many of the phenomena previously attributed to the heavy metals have been observed even in their absence, leading to the questions about their origin in these cases. In this chapter, we address these questions by studying epitaxial Fe single layers, a model system that has been stripped down to the bare necessities. This project puts a spotlight on FM/oxide interfaces, which have been often overlooked regardless of their ubiquity. The contents of this chapter are taken from a manuscript in preparation.

The work was led by myself, under the supervision of Pietro Gambardella. I performed the data acquisition, and developed both the specific implementation of the fitting algorithm, and the design and fabrication of the devices, excluding the sample growth. The deposition of the epitaxial samples was performed in our in-house MBE setup in the Magnetism and Interface Physics Group at the ETH Zürich with the assistance of Santos F. Alvarado. For the device fabrication, the cleanroom facilities at the PSI Villigen were used, for which I acknowledge Vitaliy Guzenko and Anja Weber for their support and Laura Heyderman for enabling this collaboration.

6.1. Magnetoresistance and Current-induced Effects

Over the last decades, concerted efforts in the field of spintronics have led to a continuous flux of new discoveries about the response of ferromagnets to electrically-induced spin currents. Among the most studied systems, HM/FM bilayers have been shown to exhibit a large variety of current-induced phenomena, a prominent one being the spin-orbit torque [20]. Starting with the demonstration of current-induced switching of Pt/Co/AlO_x dots [87] , the properties of spin-orbit torques have been steadily revealed [54, 88–93] , which eventually enabled fast and precise control of the magnetization [94–97]. Not only were new paths opened up to control the magnetization, through the study of bilayer systems our understanding of magnetic sensing using magnetoresistance measurements has also expanded. For one, several magnetoresistive effects deviating from the well known anisotropic magnetoresistance[5] were found, such as the spin Hall magnetoresistance [28, 98], the UMR [27, 67, 77], and the crystalline anisotropy of the magnetoresistance observed in epitaxial systems, which consists of contributions from the bulk [36, 37, 57–62] as well as the interfaces [63]. While the bulk contribution to the crystalline magnetoresistance was predicted very early on [37] and demonstrated in many thin film systems [36, 57–62] , evidence of an interfacial contribution has only recently come to light in a study of the epitaxial GaAs/Fe system [63, 99]. The interfacial crystalline magnetoresistance imprints the symmetry of the spin-orbit-induced interfacial fields at the interface onto the AMR, leading to a change of the amplitude and shifting of the angular dependence according to the direction of the current with respect to the crystal axes. In addition to such modifications of the AMR, an entirely new behavior of

the magnetoresistance presented itself with the discovery of the UMR. Unlike the previously discussed magnetoresistances, the UMR is a non-linear effect, meaning that the resistance scales with the current [27, 67, 77]. Here, the spin-dependent resistivity of FMs in conjunction with the injection of a spin current from the HM into the FM results in a change in the resistance [77, 100], which allows for the differentiation between opposite in-plane magnetized states using two terminal resistance measurements [101].

These phenomena all have one thing in common, which is the interaction between a spin current and the magnetization. While charge currents are spin polarized in ferromagnetic layers, such a naturally occurring spin polarized current by itself is not able to manifest these phenomena, as the spin polarization is collinear with the magnetization. Instead, the necessary transverse spin current in these cases is produced in the HM via the SHE or at the interface via the Rashba-Edelstein effect and spin-dependent scattering [70, 72]. Although heavy metals are a good choice as a source of transverse spin current, the catalogue of promising material combinations is constantly being expanded, leading to the discovery of an unlikely competitor, namely Cu, a normal metal. The lack of strong spin orbit coupling in normal metals, usually makes them unattractive for their usage as spin current sources, however, the introduction of oxidation gradients in these films has shown to boost their spin current conversion efficiency, rivaling even heavy metals [68, 69, 102]. Lately, however, mechanisms to generate spin currents with spin polarization non-collinear to the magnetization have been found also in single layer ferromagnets in the absence of heavy metals. In particular, single layer FM with oxide interfaces, which are the focus of this work, have been found to exhibit both spin-orbit torques [53, 68–72, 102–105] and unusual magnetoresistance effects [32, 33, 35, 36, 106]. One of those mechanisms is the SHE. Although symmetry

considerations allow for the SHE to exist in FMs, it was assumed to have a diminished effect in FMs due to the rapid dephasing of spins that are not parallel to the magnetization. However, first principles calculations have shown that the SHE generated spin currents are indeed intrinsically stabilized [70], making the SHE a viable source of transverse spin currents, where transverse in this case refers to the alignment of the spin polarization and the magnetization. Around the same time, current-induced SOTs similar to those in multilayers were reported in single layer FMs, an example of the effect of these intrinsic transverse spin currents [71]. Since the observation of SOTs is naturally accompanied by the presence of spin currents, other spin current related effects can in principle also manifest in a single FM layer, which brings us to the starting point of this work.

Here, we study the magnetoresistance and current-induced and spin current related effects using harmonic voltage measurements in epitaxial Fe/MgO and Fe/AlO_x layers grown on MgO(001) and demonstrate a self consistent method to analyze this suite of effects using macrospin simulations. This measurement technique provides access to the CMR, SOTs, and UMR using a single type of device. Moreover, the study of epitaxial systems allows us to unveil the crystalline anisotropy as a function of the direction of the current with respect to the crystal axes of each effect. And indeed, we observe significant CMR, SOTs and UMR in both the nominally symmetric MgO/Fe/MgO as well as the asymmetric MgO/Fe/AlO_x system. In both systems, the 4-fold symmetry of the crystal structure was imprinted on the CMR. The same crystalline anisotropy was observed in the current-induced effects, i.e. the SOTs and the UMR.

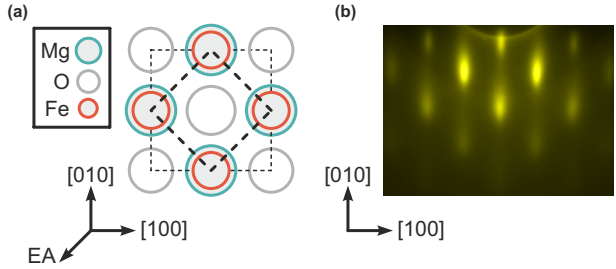

Figure 6.1.: (a) In the epitaxial MgO(100)/Fe system, the Fe lattice is rotated by 45° with respect to the MgO lattice and as a consequence the easy directions of the cubic magnetic anisotropy are rotated as well. (b) The RHEED image taken after the deposition of Fe on MgO shows the 45° rotation and confirms the quality of our epitaxial films.

6.2. Sample Fabrication

The epitaxial 2 nm thick Fe layers studied here were grown on MgO(001) crystals using molecular beam epitaxy. Prior to deposition, the MgO crystals were heated to ≈ 600 °C in ultra-high vacuum and left to cool down to room temperature before deposition. As shown in Figure 6.1a, the Fe lattice grows with a 45° rotation on the MgO(001) substrate, leading to a 4-fold magnetic easy axis oriented along the ⟨110⟩ directions of the MgO. The RHEED images, shown in Figure 6.1b, were taken during the deposition to control the growth and confirm the 45° rotation of the Fe lattice compared to the MgO(001) surface, which confirms the crystallinity of our films. The single magnetic layer was subsequently capped with two different oxides, producing the nominally symmetric system MgO(001)/Fe (2 nm)/MgO (2 nm)/AlO_x (5 nm) and the asymmetric system MgO(001)/Fe (2 nm)/AlO_x (5 nm). In addition to directly modifying the Fe/Oxide interface,

changing the top interface also results in different inversion symmetries around the Fe and the neighboring layers. Whereas MgO(001)/Fe/AlO_x is asymmetric and lacks inversion symmetry, MgO(001)/Fe/MgO is nominally symmetric and possesses inversion symmetry. The MgO system was additionally capped with an AlO_x layer to protect the MgO from the atmosphere. For the rest of this chapter, we will refer to these systems by the top Fe interface.

Before the samples were patterned for electrical transport measurements, we characterized the in-plane magnetic anisotropy of the full films via MOKE measurements, shown in Figure 6.2a. As expected, we found the 4-fold magnetocrystalline anisotropy

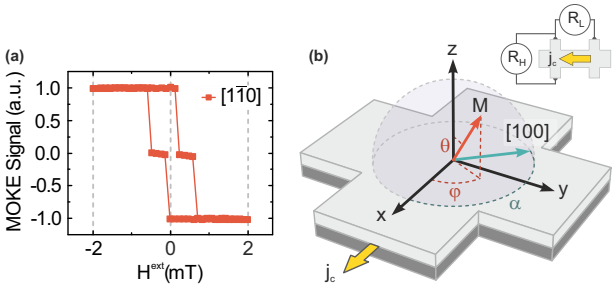

Figure 6.2.: (a) The longitudinal MOKE hysteresis measured along one of the easy directions of the as grown Fe/MgO shows the two step reversal which is typical for systems where a uniaxial anisotropy overlaps the cubic anisotropy. (b) The Hall bar devices allow for the simultaneous measurement of the longitudinal and transverse resistance. We define a coordinate system where $\boldsymbol{x} \parallel \boldsymbol{j_c}$ and use spherical coordinates to describe the direction of $\boldsymbol{M}$ (red arrow). The angle between the current (yellow arrow) and the [100] direction (teal arrow) of the MgO is defined as α.

with easy directions along the diagonals MgO⟨110⟩. Interestingly, there is also evidence of a uniaxial anisotropy in the full films, as indicated by the two-step jump in the hysteresis loop. Such a hysteresis loop is typical for systems where a 2-fold anisotropy overlaps with the 4-fold anisotropy [44, 45, 107–109]. Specifically, the uniaxial anisotropy lies along MgO[110], overlapping with one of the cubic easy axes, while the magnetic field for the hysteresis loop points roughly along the other cubic easy axis MgO[1$\bar{1}$0]. In this case, instead of directly reversing from [1$\bar{1}$0] to [$\bar{1}$10] in a single jump, the uniaxial anisotropy forces the magnetization to jump from [1$\bar{1}$0] to [110] first, before fully reversing, resulting in the characteristic two-step jump. Uniaxial anisotropies in MgO(001)/Fe films have been shown to be caused by an angled deposition, where the Fe beam is not normal to the surface, leading to a strained microstructure and anisotropic surface roughness, which can induce a magnetic anisotropy. [44–47]

After the patterning process, we can quantify the in-plane magnetic anisotropy of the patterned Hall bars by scanning the angular dependence in the plane and using the fitting process shown in Section 4.4. From this analysis we obtain an effective magnetocrystalline anisotropy field of $\mu_0 H_{\text{cub}} \approx 50\,\text{mT}$ for both the MgO system and the AlO_x system. Unsurprisingly, the magnetocrystalline anisotropy of the two systems are practically identical, as the magnetocrystalline anisotropy is to a large part related to the crystallinity of the Fe, which itself is determined by the substrate. We could not detect any significant contribution of the in-plane uniaxial anisotropy, which we observed in the MOKE measurements of the films prior to patterning. This could be the result of the texture not affecting the anisotropy strongly at the length scales of the Hall bars. Furthermore, the strained microstructure of the Fe layer could have been affected by the baking steps required for the device fabrication

[46, 110]. In addition to the anisotropies in the plane, we can also measure the out-of-plane anisotropy field with out-of-plane hysteresis loops. As expected for magnetic thin films, we see an out-of-plane magnetic hard axis, or more specifically we obtain $\mu_0 H^{\text{oop}}_{\text{mgo}} = -1500\,\text{mT}$ and $\mu_0 H^{\text{oop}}_{\text{alox}} = -1600\,\text{mT}$. This hard axis is the result of the competition between the demagnetizing field, which forces the magnetization into the plane, and the interface-induced anisotropy, which promotes perpendicular magnetic anisotropy. Since interface effects are short-ranged, the 2 nm thickness of the Fe is enough to make the demagnetizing field win against the interface-induces anisotropy. Unlike we have seen for the magnetocrystalline anisotropy, the strength of the out-of-plane magnetic hard axis differs between the two system. The difference in H^{oop} can either be due to difference in the thickness of the films or in the interface-induced anisotropy, but nonetheless the values fall in the expected range.

6.3. Magnetoresistance Measurements

6.3.1. Magnetization Dependence of the Magnetoresistance

In Figure 6.3a we present the three angle scans of the magnetoresistance taken in each plane. According to the anisotropic magnetoresistance model, the amplitude of the ZY-scan should be zero, which is apparently not the case in our single layers. Instead, we observe the opposite, where most of signal is in the ZY-scan and almost none in the ZX-scan. Such a behavior has been reported before in single layer FM thin films and traced back to the anomalous Hall magnetoresistance (see Section 3.4.3). Additionally, the film texture has been demonstrated to allow for significant ZY-scan contributions in Pt/Co/Pt structures, which could also play a role in our epitaxial systems. The lack of higher

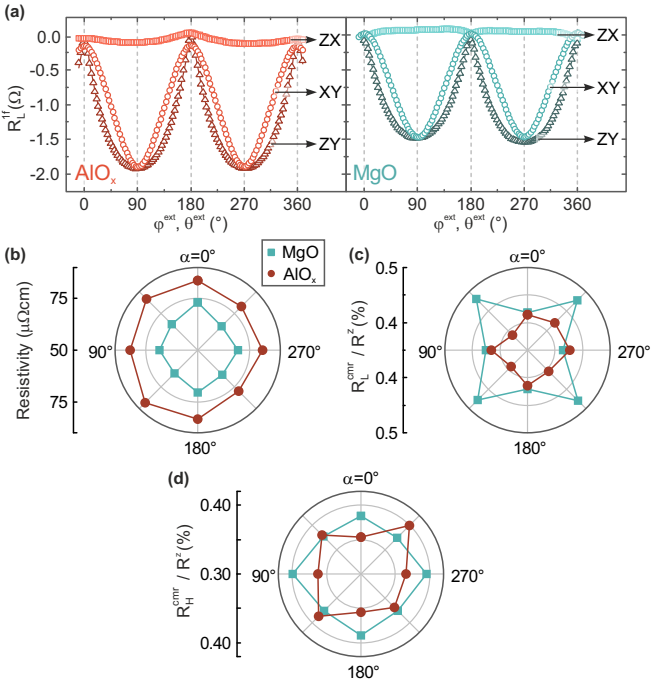

Figure 6.3.: (a) R_L^{1f} signal of the XY, ZX, and ZY scans of the AlO_x and MgO sample both show that the main contribution to the magnetization dependence comes from the ZY scan, instead of the ZX scan. (b-e) Each point of the α-dependence was measured on a different Hall bar on the same sample (b) The resistivity of the two samples shows a weak indication of the 4-fold symmetry. (c-d) In both R_L^{cmr} as well as R_H^{cmr} the 4-fold symmetry is expressed more strongly. The inversion of the maxima and minima in the CMR can be an indicator for the SOTs.

order $\cos^{2n}\theta$ terms in our measurements indicates however that it might not be as dominant here as it was in the textured Pt/Co/Pt structures.

6.3.2. α-dependence of the CMR

The first indicator of the CMR is the resistivity of the devices, presented as a function of α in Figure 6.3b, where each data point was measured on a separate device in the asymmetric (red points) and symmetric (teal points) system. In both systems, the resistivity peaks when $\boldsymbol{j_c}$ flows along one of the MgO ⟨100⟩ crystal axes and is generally lower when $\boldsymbol{j_c}$ is diagonal to the crystal axes, resulting in a slight four-fold symmetry in the resistivity.

We note here that the resistivity of the AlO_x system was consistently higher than the one of the MgO system, which could be caused by several factors. First, as the samples were not deposited simultaneously, we expect some thickness variation between the two, which, in the thickness range studied here, would result in significant changes in the resistance. Another factor might be over- or underoxidation of the top oxide interface, which can occur during reactive deposition. Nevertheless, in each sample the relative change of the resistivity with respect to α still reflects the 4-fold crystal symmetry.

Next, we compare R^{cmr} of the two systems, shown in Figure 6.3c. Both $R_{\mathrm{L}}^{\mathrm{cmr}}$ and $R_{\mathrm{H}}^{\mathrm{cmr}}$ were obtained in the same fit as the magnetic anisotropy. $R_{\mathrm{L}}^{\mathrm{cmr}}$ exhibits a strong four-fold symmetry in both systems, but with the difference that the maxima and minima are inverted. Explicitly, in the symmetric MgO system the maxima are located at the diagonal MgO⟨110⟩ directions i.e. $\alpha = 45°$, 135°, 225° and 315°, and the minima are along the main MgO⟨100⟩ directions. In the AlO_x system, the maxima and minima are reversed, thereby shifting the maxima to MgO⟨100⟩, while the minima are located along MgO⟨110⟩. The apparent ro-

tation of the symmetry axis in $R_{\mathrm{L}}^{\mathrm{cmr}}$ is directly related to a change of sign of $b - c$. The same behavior is observed in the transverse manifestation $R_{\mathrm{H}}^{\mathrm{cmr}}$, shown in Figure 6.3d. Again, the 4-fold symmetry is strong in both systems and we observe the reversal of the maxima and minima going from one system to the other. It is worth pointing out that compared to $R_{\mathrm{L}}^{\mathrm{cmr}}$, $R_{\mathrm{H}}^{\mathrm{cmr}}$ is rotated by 45°, which is consistent with expression of the CMR (Eq.4.12 and Eq.4.16 in Chapter4) From the α-dependence of $R_{\mathrm{L}}^{\mathrm{cmr}}$ and $R_{\mathrm{H}}^{\mathrm{cmr}}$, we can extract the CMR parameters and obtain $b = 1.60\,\Omega$ and $c = 1.48\,\Omega$ for the MgO system and $b = 1.65\,\Omega$ and $c = 1.73\,\Omega$ for the AlO_x system. As can be seen, the sign reversal of the CMR between the two systems is mostly brought about by a change in c, while b remains relatively constant. In a previous study on the CMR, the same behavior was found in GaAs/Fe, where a decrease of the Fe thickness from 8 monolayers (≈ 1.1 nm) to 6 monolayers (≈ 0.86 nm) leads to an increase of b from $\approx 3\,\Omega$ to $\approx 4.5\,\Omega$ and a dramatic increase of c from $\approx 2.6\,\Omega$ to $\approx 7.5\,\Omega$ [63].

This brings us to the source of the interfacial CMR, which has been reported to be the spin-orbit fields at the interface, generated by spin-orbit-induced interface effects [63]. In GaAs/Fe, by decreasing the Fe thickness, the influence of the interfacial spin-orbit fields increases, leading to stronger effective SOTs, which eventually causes the reversal of the CMR. In our systems, we were able to induce a reversal of the CMR in much thicker Fe layers by exchanging the top interface from MgO to AlO_x . This not only hints at the mere presence of SOTs but also indicates that the SOTs should have increased when transitioning from the Fe/MgO system to the Fe/AlOx system, although not as much as through the thickness change in the GaAs/Fe study. Thus as our next step, we further exploit the capabilities of harmonic voltage measurements to quantify the current induced SOTs in these systems and confirm their presence as suggested by the CMR.

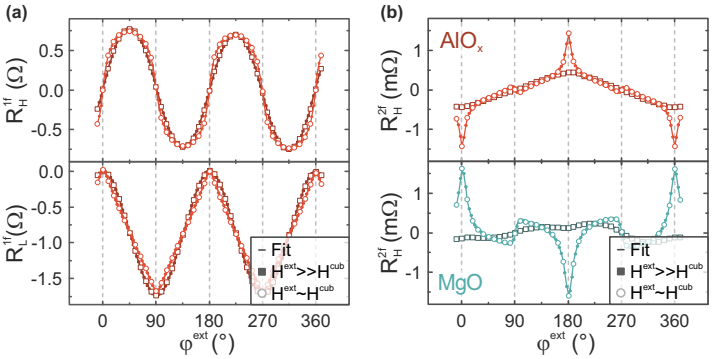

Figure 6.4.: (a) Transverse and longitudinal R^{1f} data (symbols) and fit (line) of a XY-scan measured on the AlO_x system. Only every third data point is highlighted to reduce clutter. For lower fields, the curve distorts, which allows for the extraction of the magnetic anisotropy. (b) Transverse R_H^{2f} data and fit of the asymmetric (red) and symmetric (teal) system measured at high and low fields for $\alpha = 0°$ and $j_c = 10^{11}\mathrm{Am}^{-2}$, which corresponds to $I_0 = 2000\,\mu\mathrm{A}$.

6.4. Current-induced Effects

While magnetoresistance parameters can be accessed by analyzing the first harmonic signal, current-induced effects such as the SOTs and the UMR are found in the second harmonic, the extraction process of which we present in the following sections.

6.4.1. Spin-orbit Torques

The second harmonic Hall signal R_H^{2f} of the XY scan, which is shown in Figure 6.4b for $\alpha = 0°$, will be the main focus of the SOT derivation. All results shown here were measured with a current density of $j_c = 10^{11}\mathrm{Am}^{-2}$. If we first look at the high

external field measurements of R_H^{2f} in Figure 6.4b, we observe a simple $\cos\varphi^{ext}$ dependence. As the field is reduced, however, peaks around $\varphi^{ext} = 0°$ and $\varphi^{ext} = 180°$ start appearing. This hints at the presence of SOTs, more specifically the field-like torque H^{fl}, which typically scales reciprocally with the external field [80]. The deviation of the H^{fl} signal from the well known $\cos\varphi\cos 2\varphi$ symmetry observed in polycrystalline systems is caused by the cubic magnetocrystalline anisotropy (see Fig.4.6). In particular, if $\boldsymbol{m}$ is pointing along one of the hard axes, which in the specific case shown here are located at $\varphi^{ext} = 0°$ and $\varphi^{ext} = 90°$, the magnetization is more susceptible to the SOTs. This results in the amplification of the signature H^{fl} peaks at $\varphi^{ext} = 0°$ and $\varphi^{ext} = 180°$. On the other hand, if $\boldsymbol{m}$ is aligned with an easy axis, the magnetocrystalline anisotropy will suppress the SOTs instead and flatten out the generated signal. While this also applies to the damping-like torque H^{dl}, the much larger influence of H^{oop} shrouds the small variation caused by H^{cub}.

Although the presence of SOTs in single layer ferromagnetic systems is not unheard of [53, 71, 104], evidence of SOTs in such systems has been scarce, which makes the strong signal observed here by harmonic voltage analysis even more remarkable.

From the fitting procedure described in Section 4.4, we can calculate the induced torques for each device. For a current density of $j_c = 10^{11}\,\mathrm{Am}^{-2}$ and averaged over all rotations α, we obtain $\mu_0 H^{fl}_{mgo} = (129 \pm 8)\,\mu\mathrm{T}$ and $\mu_0 H^{dl}_{mgo} = (-9 \pm 6)\,\mu\mathrm{T}$ for the MgO system and $\mu_0 H^{fl}_{alox} = (-41 \pm 8)\,\mu\mathrm{T}$ and $\mu_0 H^{dl}_{alox} = (-23 \pm 7)\,\mu\mathrm{T}$ for the AlO_x system, where the error corresponds to the variance in the α-dependence. Furthermore, we repeated the SOT measurements for a range of applied currents. The results of these additional measurements, shown in Figure 6.5a, reveal the linear relationship between the applied current and the SOTs, which we expected to see in current-induced effects. Generally,

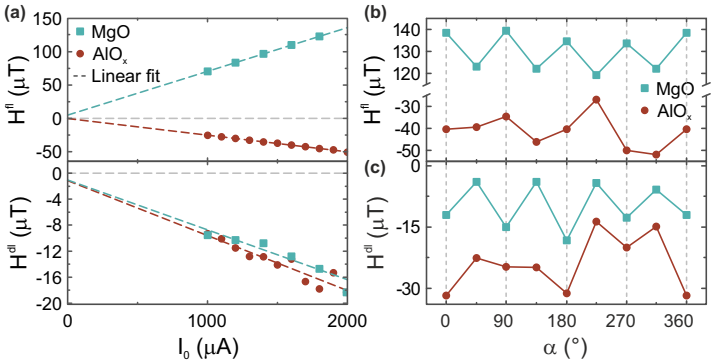

Figure 6.5.: (a) Current dependence of the SOTs for $j_c \parallel$ MgO⟨100⟩. As expected, the SOTs linearly increase with the current, which validates the results of the analysis. Non-zero intercept of the H^{dl} fit is attributed to the variance of the fitted values. (b) Field-like torque extracted from the 2nd harmonic fits. As the reversal of the signature peaks of H^{fl} in Fig.6.4b already implied, H^{fl} changes sign between the two systems. (c) The calculated damping-like torque H^{dl} has a consistent sign regardless of the top interface. The 4-fold crystalline anisotropy was mainly observed in the Fe/MgO system, although there are traces of the symmetry left in H^{dl}_{alox}.

the SOTs ended up in the sub-mT range with some differences between the two systems. As can be seen, both components of the SOT change when the top interface is exchanged, however, H^{fl} is affected much more strongly, to the extent that H^{fl}_{mgo} and H^{fl}_{alox} differ in sign. As shown in Figure 6.5a, the differences between H^{fl}_{mgo} and H^{fl}_{alox} do not end there, as we also observe relatively distinct α-dependencies. In the MgO system, both SOT components exhibit the 4-fold crystal symmetry, with maxima

of magnitudes along MgO⟨100⟩. In the AlO_x system, we can still identify the same symmetry in H^{dl}_{alox}, though the trend has deteriorated. In contrast, H^{fl}_{alox} exhibits no discernible 4-fold symmetry, although the variation that does occur is relatively strong.

The crystalline anisotropy of the SOTs indicates non-trivial behavior of the epitaxial Fe single layers, but before we dive into the possible origins of these SOTs, we want to demonstrate the presence of another current-induced effect, i.e. the UMR, which can shed more light on the spin currents driving these effects.

6.4.2. Unidirectional Magnetoresistance

The UMR is derived from the 2nd harmonic longitudinal resistance R^{2f}_1, an example of which is shown in Figure 6.6a. For this derivation we need to separate the SOT signal, thermo-electric effects and the UMR, for which we use the fitting procedure described in Section 4.4. For the decomposition of R^{2f}_1 presented in Figure 6.6a, we presumed the UMR to consist only of the sd-UMR, which in this configuration is proportional to $\sin\varphi^{ext}$. The good quality of the fit for both external fields, i.e. 77 mT and 1.7 T, suggests that the UMR in our system does not scale with the external field und thus the sd-UMR suffices to accurately describe R^{2f}_L. In addition to the lack of field dependence, we also observed linear scaling of the UMR with the current, as shown in Figure 6.6b, which further hints at the fact that the UMR consist mainly of the sd-UMR [77]. The lack of a sf-UMR signal does not inherently exclude sf-UMR in Fe single layers but shows that it is likely suppressed by the crystalline magnetic anisotropy.

Normalized by the resistance, the UMR in our systems ends up being one order of magnitude smaller than values reported for HM/FM bilayer systems [27]. In the AlO_x system, R^{umr} exhibits a strong 4-fold variation of $\approx 30\,\%$ around its average of 0.56 ppm.

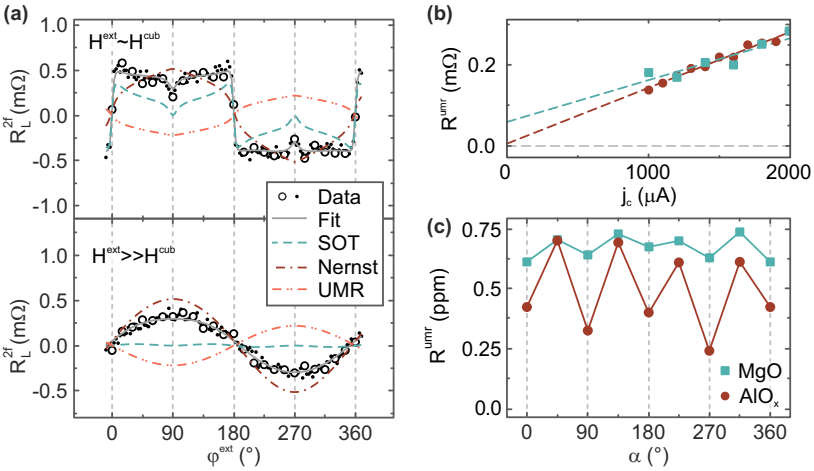

Figure 6.6.: (a) The 2nd harmonic longitudinal data R_L^{2f} (symbols), shown here for Fe/AlO_x and $\alpha = 0°$, is comprised of the SOT signal, Nernst effects and UMR. To reduce the clutter only every fourth data point is highlighted. (b) The UMR appears to scale linearly with the applied current, which has been reported to be a characteristic property of the sd-UMR. The non-zero intercept of the fitted UMR in the MgO system is likely caused by the scattering of the data point measured at the lowest current, which has a large leverage. (c) In both systems, we observe a positive UMR with a 4-fold crystalline anisotropy.

Compared to that, the variation seen in the MgO system is rather weak, with a change of $\approx 7\,\%$ around its average of 0.78 ppm. In both cases the maxima are along the MgO⟨110⟩-directions, which is opposite to the SOTs.

6.5. Discussion

Non-zero SOTs in FM single layers The SOTs reported here are one to two orders of magnitude smaller than the ones in HM/FM bilayers [20, 54, 88], but they match the sub-mT range that has been reported in Fe and NiFe single layer thin films. [71, 92] In the work of Wang et al. on NiFe films [71], they successfully separated the SOT contributions of the top and bottom interface in symmetric AlO_x /NiFe/AlO_x films, and demonstrated how the two contributions opposed each other. The driving force behind the SOTs in that work was concluded to be the SHE of the NiFe alloy. Taken at face value, the total SOTs in systems with symmetric interfaces such as these should vanish, but nevertheless, appreciable total SOTs were observed in NiFe thin films, which fits our findings in the MgO(100)/Fe/MgO system. We ascribe this to the fact that the two interfaces are different in terms of quality, one being a polished substrate where the other is the result of multiple depositions resulting in different topographies [111]. In the asymmetric MgO(100)/NiFe/AlO_x system, the perfect cancelling of SOTs on opposite interfaces is less of an issue, because the system was engineered to have broken inversion symmetry, for one through the change of material and also through the structure of the interface.

UMR vs. SOTs: A Sign Comparison Before we further analyze the sign and crystalline anisotropy of the SOTs, we can set our expectations by looking at the relationship between the UMR and SOTs in the HM/Co system. The initial study on the UMR compared Pt/Co and Ta/Co [27], in which it was already known that the SOTs are opposite, and found the UMR also to be opposite in these cases. Since both the UMR and the SOTs depend on the total spin polarization in the FM layer, our initial assumption would be for the signs of the UMR and SOTs to be identical in

our single layers as well.

Coming back to the MgO and AlO_x systems, we observe an appreciable UMR in both systems, exhibiting the same sign as observed in Pt/Co, which indicates a total spin polarization $\boldsymbol{\sigma_z} \parallel \boldsymbol{y}$, but ranging around one order of magnitude lower than in HM/FM bilayers [27]. In addition to the linear scaling with the injected current, no external field dependence was found, which suggests that only the sd-UMR appears in these systems. The lack of sf-UMR is accredited to the magnetocrystalline anisotropy, which, even in the absence of the external field, will suppress the magnon excitation by the spin current. The observation of the UMR in single layers demonstrates that even small changes in the interfaces, such as in the oxidation level or morphology, can lead to the inversion symmetry breaking required to observe spin-current-induced effects.

Knowing the sign of the dominant spin polarization, we can compare it to the sign of the SOTs. Unlike the UMR, which has the same sign as in Pt/Co bilayers, the DL SOTs in our systems have the opposite sign, matching what has been reported in Ta/Co bilayers [94]. On the other hand, the sign of the FL torques in the two systems differ as we obtain a positive value for the MgO system and a negative value for the AlO_x system. A quick overview of the signs of the UMR and SOTs for the reference systems Pt/Co and Ta/Co, compared to the ones we measured in our systems, is given in Table6.7. Since the FL torque can be induced by the FL SOT and the Oersted field, we first discuss the sign of the DL SOT to get a clearer picture.

Considering that the sd-UMR is a good indicator of the total spin polarization in the system [112], it is surprising to find a DL SOT with the opposite sign, since we would expect it to scale with total spin polarization as well [27, 113]. Thus, there must be a factor other than the spin polarization, which affects the DL SOT balance between the top and the bottom

Table 6.7.: Overview of the signs of the UMR and SOTs measured in epitaxial single layers compared to HM/FM reference systems.

Structure	UMR	DL SOT	FL SOT	Oersted Field
Pt/Co	+	+	+	−
Ta/Co	−	−	−	−
MgO/Fe/MgO	+	−	+	
MgO/Fe/AlO_x	+	−	−	

interface. One possibility is that this is a consequence of two factors. First, the total spin polarization, as indicated by the sign of the UMR, is the average between the opposing spin accumulations at opposite interfaces. This would be the case for spin accumulations produced by the SHE in the Fe layer or by the Rashba-Edelstein effect in the symmetric system where both interfaces are nominally the same. Second, there is a difference in the magnetic susceptibility between the top and the bottom interface due the different magnetic interface anisotropy. The Fe/MgO interface is known for its ability to induce perpendicular magnetic anisotropy, and thus has found uses in magnetic tunnel junctions [114–117]. In our systems the Fe is too thick for the interfaces to induce a PMA, resulting in an OOP hard axis in both systems. Nevertheless, the interface-induced magnetic anisotropy can still affect the magnetization close to the interface. Seeing as morphology and contamination affect the perpendicular magnetic anisotropy, it comes as no surprise that the interface anisotropy of the bottom interface MgO(001)/Fe, which is a result of deposition on a polished single crystal, could differ from the top interface [118]. Consequently, the UMR and SOTs could differ in sign, if the interface that has a weaker spin accumulation, has a higher susceptibility to compensate for it. This would generate

a stronger SOT signal [26] at the interface with the weaker spin accumulation.

However, the UMR and DL SOTs having opposite signs can also be a result of a combination of different spin current sources that affect the UMR and SOTs differently. The SHE and REE are among the spin current sources that have proven to generate both the UMR and SOTs. The different nature of these two effects, the REE being a purely interfacial effect and the SHE generating spin currents throughout the bulk, has shown to directly impact the ratio of the two SOT components [89]. This led to the general association of the FL SOT with the REE and the DL SOT with the SHE. Similarly, the UMR generated by the SHE and REE can differ greatly as observed in other studies, where much larger UMR were found in association with the REE [119, 120]. Ultimately, the question of the microscopic origin of the sign difference remains open.

If we focus our attention on the FL torque H^{fl}, the first aspect that stands out is the difference in sign between the FL torque and the DL SOT in the MgO system. As shown in Table6.7, the SOTs in the HM/FM reference systems possess the same sign, however the sign of the total FL torque in Pt/Co has been shown to differ from the DL SOT, due to to the Oersted field contribution arising in bilayers. In HM/FM bilayers, the Oersted field can be approximated by assuming the two layers to behave as parallel resistors. From the portion of the current passing through the HM layer the Oersted field can then be calculated using a parallel resistor model. In single layers, ideally all of the current is passing through the FM causing no Oersted field that acts on the FM as result. Realistically, however, the uniformity of the FM along the film normal is not a given. For one, interface resistances can be different at the two interfaces due to differences in the chemical composition, including the oxidation level, and the morphology. If as a result of these factors, the resistance at

the top interface is lower than the one on the bottom, the Oersted field contribution to the FL torque is positive. If more current passes through the bottom of the FM, the FL torque is negative. Separating the Oersted field from the FL SOT is not a simple task in single layers, as we have positive and negative contributions of the SOTs from each interface. On top of that, the H^{fl} is then offset by the Oersted field, which can also be both positive or negative depending on whether we presume the top interface to be under- or overoxidized. With a sign comparison between the UMR, DL SOT and FL torque alone, we cannot determine the sign or strength of the FL SOT. However, some evidence can be found the resistivity and the crystalline anisotropy, which we will address next.

Crystalline Anisotropy The α-dependence of both the UMR and almost all of the derived SOTs exhibited a 4-fold crystalline anisotropy imprinted by the cubic structure of the Fe. Again we will start with the comparison between the UMR and the DL SOT. Not only is there a difference in the sign between the UMR and the DL SOT, we also observed that their magnitudes are anti-correlated. For the UMR the largest values are found along the substrate diagonals MgO⟨110⟩, whereas the magnitude of H^{dl} is maximal along the crystal axes MgO⟨100⟩.

This 4-fold variation could be caused by the crystalline anisotropy of the spin Hall conductivity, which has been theoretically predicted in previous studies on other ferromagnetic crystals [70, 121]. However, an overall decrease of the spin polarization should lead to correlated crystalline anisotropies in both the UMR and DL SOTs, as both effects scale with the strength of the spin current.

Another mechanism could be anisotropic dephasing of the spins [122], which for SHE-generated spin currents in Fe is only

possible after scattering at the interface. For magnetic materials, we can naively explain this anisotropy by taking into consideration the direction of the spin polarization σ_z with respect to the magnetocrystalline anisotropy. If the spin polarization is aligned with a hard axis, which is the case for currents along MgO⟨100⟩, the magnetocrystalline anisotropy destabilizes the spin current, thus stronger precession is encouraged, leading to quicker dephasing. For currents injected along MgO⟨110⟩, the spin polarization is aligned with an easy axis, which stabilizes the spins and prevent fast dephasing. But how does this affect the UMR and the SOTs? Rapid dephasing effectively shortens the spin diffusion length [89, 123, 124], which reduces the spin accumulation at the interfaces as a result. Since the UMR is proportional to the spin accumulation, the UMR will become smaller accordingly. The DL SOT however is expected to *increase* in magnitude with increasing dephasing, since the rapid dephasing equates to efficient transfer of angular momentum from the conduction electrons to the local magnetization [89, 123, 124].

Unlike the UMR and the DL SOT, we only observe the crystalline anisotropy of H^{fl} in the MgO system. This is evidence that there should be a significant FL SOT contribution to the FL torque, since the Oersted field is unlikely to exhibit this anisotropy, unless the relative conductivity of the top and bottom layer varies as α is changed. Instead, the anisotropic dephasing discussed above for the other effects also has an impact on the FL SOT. Applying the spin dephasing mechanism to the FL SOT would predict a decrease in magnitude of the FL SOT with increased dephasing in materials with an already short spin diffusion length [123–125]. This is made evident if we examine the extended drift-diffusion model in the case where the dephasing is instantaneous. As demonstrated in Refs. [123–125] in these cases, the FL SOT vanishes and only the DL SOT remains. This relationship between the dephasing and the FL SOT results in anti-correlated SOT

components and a positive correlation with the UMR.

For that to be the case however, the FL SOT in the MgO system would have to be negative, with an Oersted field strong enough to result in the positive offset of the total FL torque. A positive Oersted field would require a higher conductivity at the top interface compared to bottom interface, for which we could argue considering the resistivity measured on the two systems. The overall lower resistivity of the MgO compared to the AlO_x sample can be an indicator for an underoxidized MgO layer. The underoxidized MgO at the interface could then add to the conductivity. Using a parallel resistor model we estimate that $\approx 10\,\%$ of the total current would have to pass through the top interface to generate an Oersted field strong enough to positively offset a barely negative FL SOT.

Another factor that supports the notion of a positive Oersted field offset is the reversal of the CMR between the two systems. In GaAs/Fe single layers the reversal of the CMR was attributed to an increase of the FL SOTs. If the same mechanism applies for to our Fe single layers, considering the sign of the CMR in the respective systems, the average magnitude of the FL SOTs in the AlO_x system must be larger, which is only the case if $H^{\mathrm{fl}}_{\mathrm{mgo}}$ is offset by an Oersted field. However, this interpretation of H^{fl} is based on many assumptions and thus should be taken with caution.

The comparison between the crystalline anisotropy of the MgO and AlO_x system shows that the crystalline anisotropy of the SOTs is much less pronounced in the AlO_x system. This is also consistent with our expectation of the Fe/AlO_x interface to possess a more disordered interface compared to the Fe/MgO interface, which grows epitaxially. The sensitivity to a change of the top surface also indicates that the SOTs are generated mostly at the top interface. On the other hand, the crystalline anisotropy

of the UMR is maintained regardless of the top interface, which suggests that for the UMR, the bottom interface significantly contributes to the UMR. Interestingly, the crystalline anisotropy of the UMR in the AlO_x sample is much stronger than in the MgO system. We interpret that as the UMR being generated at both interfaces, with the total UMR being the result of the competition between the signals generated at the two interfaces. In the MgO system, both interfaces generate an anisotropic UMR with opposite signs and correlated magnitudes, which suppresses the anisotropy of the total UMR. In the AlO_x system on the other hand, only the bottom interface contributes to the crystalline anisotropy, which results in no suppression and a stronger anisotropy.

6.6. Conclusions

To summarize, we investigate epitaxial ferromagnetic single layers, namely MgO(001)/Fe/AlO_x and MgO(001)/Fe/MgO, using electrical transport measurements and harmonic voltage analysis, with the goal of bringing to light the crystalline anisotropy of current-induced effects, in particular, the CMR, UMR and the SOTs. By expanding existing analysis techniques and adapting models of the magnetoresistance and current-induced effects to include the CMR and strong magnetocrystalline anisotropies, we manage to quantify these effects with high precision using a single measurement technique. Our findings show that the UMR and SOTs are substantial even in the absence of external injection of spin currents, as the spin current generation by the Fe and its interfaces can induce these effects, as long as the inversion symmetry is broken to some degree, such as through chemical composition or morphology. But not only do these spin current effects exist in these samples, they also exhibit a 4-fold

crystalline anisotropy. The relationship between the anisotropy of UMR and one of the DL SOT allows us to glimpse into the spin dynamics in systems with strong magnetocrystalline anisotropy. The magnetocrystalline anisotropy was also found to impact the the magnon related component of the UMR, namely the sf-UMR, in that in mostly suppressed the excitation of magnons required for the manifestation of the sf-UMR.

This project also shows the difficulty that comes with the investigation of highly sensitive interface effects. Completely unraveling the delicate balance of multiple effects, in conjunction with the separation of parasitic effects that occlude the data, has proven to be a difficult task. If anything, these Fe/oxide systems demonstrate that every interface must be taken into account and should not be assumed to be inert.

Nevertheless, our results expose the effects of the intrinsic spin current generation in single layer FMs. Furthermore, the presented measurement and analysis methodology provide a useful tool for future investigations of spin-current-induced effects in single-crystal epitaxial layers.

7. Chiral Coupling: From Nanomagnets to Domain Wall Conduits

Nature is unequivocally chiral, the most prominent example of this being the homochirality of the chemistry of life. The discrimination of chiralities does not end with what might be considered the whims of evolution, but can be traced back to the laws that govern physics, or specifically of interest to this work, the laws that govern magnetism.

This part of my thesis encompasses two projects, in which we explored the DMI, a chiral exchange interaction observed in systems lacking inversion symmetry. With state of the art fabrication techniques that myself and my collaborators developed, we designed structures and devices that exploit the chirality induced by the DMI to invoke new functionalities. To be more precise, we use the DMI to laterally couple in-plane and out-of-plane magnetized regions in a thin film, which induces an exchange bias between these regions. This exchange bias is then exploited to achieve lateral antiferromagnetic coupling and forms the base of chiral domain injectors.

The two projects were led by Zhaochu Luo and myself, respectively, under the supervision of Laura Heyderman and Pietro Gambardella. Zhaochu Luo and myself fabricated the samples and developed the fabrication techniques for the respective projects, with the support of Manuel Baumgartner, Eugenie Kirk, Hanu Arava, Vitaliy Guzenko and Anja Weber. The fabrication was done mainly in the clean room at the PSI Villigen, in addition to depositions in the sputtering setup in the

Magnetism and Interface Physics group. The X-PEEM measurements were taken at the SIM beamline of the Swiss Light Source by Zhaochu Luo, Aleš Hrabec, Jizhai Cui, Gunasheel Krishnaswamy and myself with the help of the beam line staff consisting of Jaianth Vijayakumar, Tatiana Savchenko and Armin Kleibert. The MFM images were taken by Zhaochu Luo at the PSI Villigen. Electrical measurements were conducted by Zhaochu Luo and myself on the electronic transport setups of the Magnetism and Interface Physics group. MOKE images were taken by Marvin Müller and myself with the wide field MOKE of the Magnetism and Interface Physics group. Aleš Hrabec, Manuel Baumgartner and myself were responsible for the micromagnetic simulations. Data analysis and interpretation were led by Zhaochu Luo and myself, with input from and discussions with the rest of the team.

This chapter starts with the adapted content from the manuscript "Chirally Coupled Nanomagnets", Luo et al., Science 363, 1435-1439 (2019) [17], which concerns the first evidence of the chiral coupling in IP-OOP boundaries. The second half of this chapter focuses on the investigation of the IP-OOP boundaries used as nucleation sites built into DW conduits, which resulted in the publication "Chiral Domain Wall Injector Driven by Spin–Orbit Torques", Dao et al. Nano Lett. 2019, 19, 5930-5937 [25].

7.1. Chiral Coupling in Nanomagnets

An essential tool in the design of functional spintronic devices is the control over the coupling of separate magnetic components. Prime examples of this are the giant magnetoresistance and the latest generation of racetrack memory [24], which make use of the RKKY coupling between separate magnetic layers, as well as spin valves and magnetic tunnel junctions [126, 127], which rely on the exchange bias between coupled ferromagnetic/antiferromagnetic layers to control the magnetization [128]. While these interactions

have been widely exploited in multilayer structures, they have not been used in structures where magnetic components need to couple laterally, such as artificial spin ices [129–132]. Thus for the lateral coupling of nanomagnets, the long-range dipolar interaction has been utilized instead with great success. However, the dipolar interaction is intrinsically long-range, and decreases as the magnets are miniaturized further.

In this work, we address the lateral coupling of nanomagnets using the DMI [9, 10]. The DMI, being the antisymmetric exchange interaction, promotes orthogonal configurations of magnetic moments, as shown in Fig. 7.1, which leads to the spontaneous formation of non-collinear magnetization patterns such as spin spirals [11] and skyrmions [12, 13]. In magnetic thin film systems with perpendicular magnetic anisotropy, the DMI forces the formation of chiral Néel DWs [11, 14–16]. In owing to the DMI, the degeneracy of DWs with opposite in-plane magnetization components is lifted, leading to a preferential rotational sense of the magnetization from one domain to the next. Here, we artificially stretch out the magnetic configuration of a Néel DW in laterally coupled in-plane and out-of-plane magnetized regions. We demonstrate that the DMI couples the IP and OOP magnetization and we explore the various phenomena that emerge in these structures.

7.1.1. In-plane/Out-of-plane Nanomagnets

The fabrication of laterally coupled IP and OOP regions requires precise local control over the magnetic anisotropy. Spatial engineering of the magnetic anisotropy has previously been achieved using ion irradiation [133–139] and electric gating [140–143]. In this work, we utilize selective oxidation in order to modify the magnetic anisotropy of Pt/Co/(Al)/AlO_x layers, specifically Pt 6 nm/Co 1.6 nm/AlO_x. The underoxidized Pt/Co/Al/AlO_x sys-

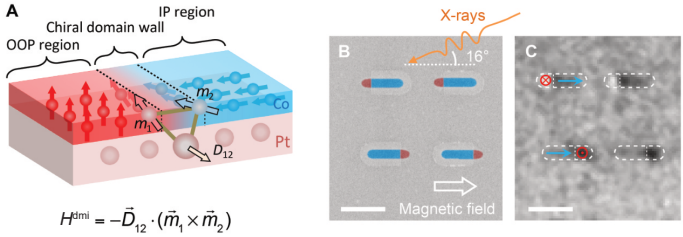

Figure 7.1.: (A) Schematics of the coupled magnetization states favored by the DMI in adjacent OOP and IP regions of a Pt/Co/AlO_x trilayer. (B) Scanning electron micrograph of coupled OOP-IP elements fabricated by means of electron beam lithography. Red and blue colors indicate regions with OOP and IP magnetization, respectively. (C) X-PEEM image with bright and dark magnetic contrast in the OOP regions corresponding to ⊗ and ⊙ magnetization, respectively. The dark gray contrast in the IP regions corresponds to → magnetization, determined by taking images at different sample orientations with respect to the x-ray direction. The direction of the incident x-rays and the IP magnetic field used for prealignment are indicated with arrows. Scale bars correspond to 500 nm.

tem is known to exhibit IP anisotropy, whereas the oxidized Pt/Co/AlO_x system possesses perpendicular magnetic anisotropy, induced by the formation of Co-O bonds at the Co/AlO_x interface [143–149]. Compared to ion irradiation, oxidation provides a way to change the anisotropy by only modifying the top interface of the magnetic layer leaving the magnetic material pristine. By locally tuning the oxidation, we can freely define regions with different anisotropy. We achieve this selective oxidation by locally protecting the structures from the oxidation with patterned

Ta masks. We use electron beam lithography for the fabrication of the IP-OOP nanomagnets, which has a lateral resolution at the nanometer scale.

The first evidence of the chiral coupling is shown in the x-ray photo emission electron microscopy (X-PEEM) images in Fig. 7.1. Here, the IP-OOP nanomagnets were saturated with an in-plane external field aligning all IP regions. The direction of the OOP magnetization $\boldsymbol{M}^{\mathbf{oop}}$, following the application of the external field, was found to depend on the position of the OOP region relative to the IP magnetization $\boldsymbol{M}^{\mathbf{ip}}$. Particularly, the $\boldsymbol{M}^{\mathbf{oop}}$ is up ("$\odot$") if the $\boldsymbol{m}^{\mathbf{ipp}}$ points towards the OOP region and down ("$\otimes$") for the opposite case. The resulting configurations $\leftarrow \otimes$ and $\rightarrow \odot$ follow the expected chirality imposed by the DMI in the Pt/Co/AlO_x system [150].

7.1.2. Lateral Exchange Bias

Next, we conducted electric measurements for which we fabricated an IP-OOP nanomagnet on top of a Hall cross, see Fig. 7.2. By probing the AHE, which scales with the z-component of the magnetization in an OOP-IP nanomagnet, we gain access to $\boldsymbol{M}^{\mathbf{oop}}$ during the OOP hysteresis loops. In the absence of exchange bias, the hysteresis would be centered around $H = 0\,\mathrm{mT}$, which is not the case in our nanomagnets. Instead the hysteresis is shifted towards positive fields when $\boldsymbol{M}^{\mathbf{ip}}$ points towards the OOP region and a negative shift is observed if $\boldsymbol{M}^{\mathbf{ip}}$ points in the opposite direction, as presented in Fig. 7.2. Indeed this exchange bias in either direction was larger than the coercive field of the OOP region, which causes the nanomagnet to always adapt the chiral configurations preferred by the DMI in the absence of external fields, confirming that our observations of the chirality in the X-PEEM were not a coincidence. Consequently, we can also switch $\boldsymbol{M}^{\mathbf{oop}}$ with an IP hysteresis loop, since upon reversal of

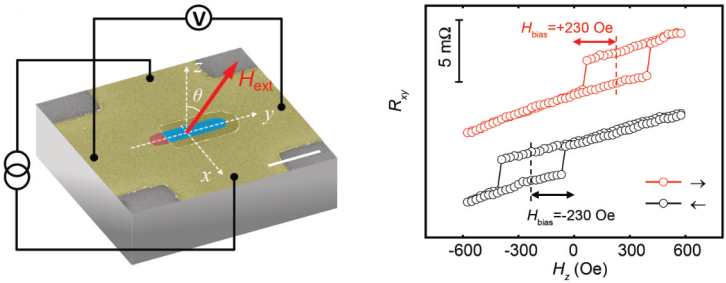

Figure 7.2.: (left) Schematic of an OOP-IP element fabricated on top of a Hall cross for electrical measurements. (right) OOP magnetization as a function of H_z for the IP-OOP element. In the top graph the IP region was set to →. For the bottom graph the IP region was set to ←. The hysteretic jumps of the anomalous Hall resistance R_{xy} indicate switching of the OOP magnetization. The linear increase of R_{xy} with field is caused by the gradual tilt of the IP magnetization toward the z-axis. Scale bars correspond to 500 nm.

$\boldsymbol{M}^{\mathbf{ip}}$, $\boldsymbol{M}^{\mathbf{oop}}$ follows suit.

7.1.3. Lateral Antiferromagnetic Coupling

With the first demonstration of the lateral chiral coupling in hand, we proceed with the exploration of more complex applications of this phenomenon, starting with an increase of the number of magnetic regions, see Fig. 7.3A. As we have shown in Fig. 7.1, for a fixed IP external field, $\boldsymbol{M}^{\mathbf{oop}}$ depends on which side of the elongated IP region the OOP region is attached to, which opens up the question of whether this still holds true for nanomagnets with OOP regions on both sides of the IP region. Predictably, we observe that the chirality is still preserved on both sides, as

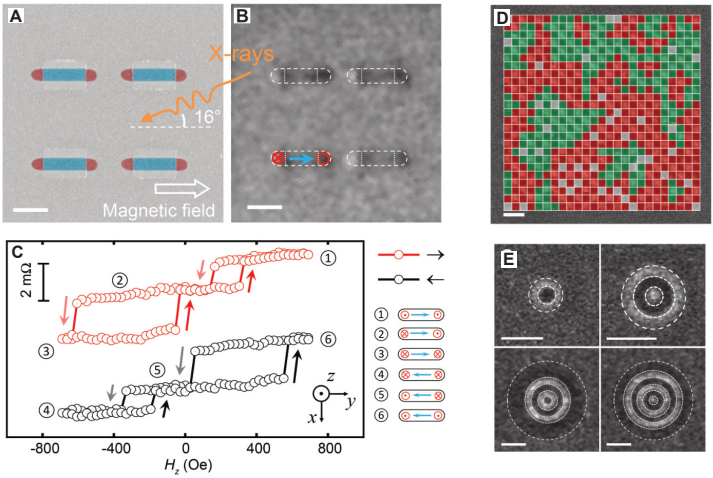

Figure 7.3.: (A) Scanning electron micrograph of coupled OOP-IP-OOP elements and (B) corresponding X-PEEM image. The stable magnetic configuration of the OOP-IP-OOP element is $\otimes \rightarrow \odot$ after prealignment of the IP region to $\rightarrow$ with an external field. (C) Magnetic hysteresis of an OOP-IP-OOP element as a function of H_z for two opposite orientations of the IP spacer. The six possible magnetic configurations are shown. (D) MFM images of synthetic skyrmions with one, two, four, and five IP rings after saturation with a magnetic field $-H_z$. (E) MFM image of an artificial spin system consisting of OOP elements on a square lattice acting as Ising-like moments coupled by means of IP spacers after saturating with a magnetic field $-H_z$. Antiferromagnetic domains are shaded in green and red. Scale bars correspond to 500 nm.

shown in Fig. 7.3B, causing the configurations $\odot \leftarrow \otimes$ and $\otimes \rightarrow \odot$ to be stabilized. Again, we confirm the X-PEEM images with electrical measurements, for which we fabricated OOP-IP-OOP nanomagnets, where one OOP region was made smaller in order to be able to differentiate their contribution to the AHE. The AHE measurements in Fig. 7.3C reveal that the exchange bias induced by the chiral coupling is opposite for the two OOP regions, causing the large and small AHE step to switch sides if the IP region is flipped. We also see that the exchange bias is strong enough to force the chiral configurations, such that in the absence of external fields, the OOP regions will always oppose each other, meaning that by daisy-chaining IP-OOP nanomagnets, we can induce antiferromagnetic coupling of the OOP regions. While this observation might seem trivial given that the DMI promotes spin spiral configurations, from a device design point of view, this opens up an abundance of avenues we can venture out into, two of which we present in Fig. 7.3D/E.

In Fig. 7.3D, we demonstrate the antiferromagnetic coupling in a square lattice of OOP regions separated by grid lines made of narrow IP regions after saturation along $-z$. In this square pattern of chirally coupled Ising-like moments, large antiferromagnetic domains spontaneously form, presented as shaded regions, in which an alternating checkerboard pattern prevails. Between the domains, neighboring OOP regions are parallel leading to frustrated states.

For the structures shown in Fig. 7.3E, we fabricated concentric OOP magnetized rings separated by thin IP regions and saturated the system along $-z$. The outermost ring, having the largest area, forces the inner rings to reverse to in order to adhere to the chirality, resulting in target skyrmionic magnetization configurations.

Both examples demonstrate how the chiral coupling can be used to precisely sculpt the energy landscape in order to create

artificial spin systems.

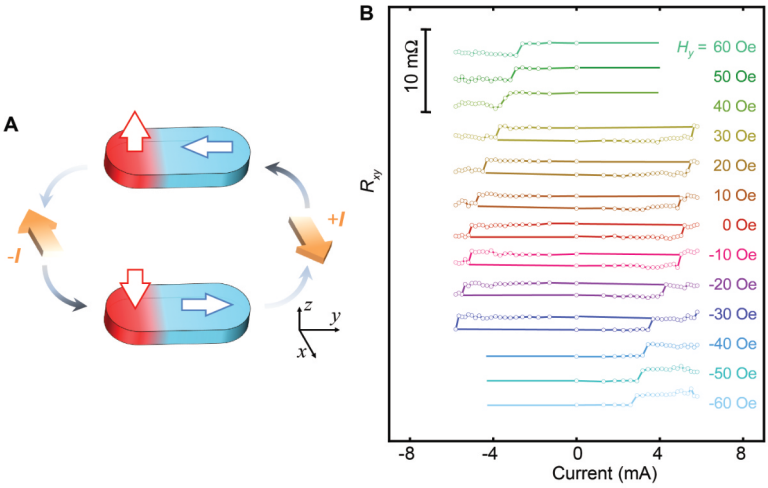

Figure 7.4.: (A) Schematic of the current-induced switching of an OOP-IP element. The device geometry is shown in Fig. 7.2A. The area of the OOP region is about 120 by 120 nm. (B) Magnetization loops as a function of applied current for different values of H_y. The measurements are performed by injecting 50 ms long current pulses and measuring the anomalous Hall resistance R_{xy} after each pulse. Changes in R_{xy} indicate switching of the OOP region. The switching at zero field is symmetric with respect to the current, whereas $H_y > 0$ helps to switch the OOP region $\otimes$ and decrease the negative switching current, and $H_y < 0$ helps to switch the OOP region $\odot$ and decrease the positive switching current.

7.1.4. Current-induced Switching

Finally, we test the current-induced switching behavior of these IP-OOP nanomagnets. Current-induced switching using spin orbit torques is a cutting edge technique, which has been shown to enable extremely fast magnetization reversal. A caveat of SOT switching is however, that in nanoscale magnetic dots with OOP magnetization, generally a magnetic bias field parallel to the current is required to achieve deterministic magnetization reversal [21]. Here we show that this problem can be circumvented using chirally coupled nanomagnets, as schematically shown in Fig. 7.4A.

The current-induced switching in the absence of external fields is demonstrated in the middle graph of Fig. 7.4B. The difference to the usual SOT switching scheme is that here, we are reversing the IP region using the current, which does not require any external fields [96]. The chiral coupling subsequently forces the OOP region to reverse This is further illustrated by the application of an external field along the y-axis. This field effectively puts a bias on the switching of the IP region, resulting in a shift of the switching current, which is strong evidence for the fact that the reversal of the OOP region is indeed coupled to the current-induced reversal of the IP region.

7.1.5. Size Limitations of the Chiral Coupling

For the chiral coupling to work as demonstrated above, two conditions must be met. First, the energy cost of maintaining configurations unfavored by the DMI must be higher than the energy cost of reversing the one of the chirally coupled regions. The energy associated with the DMI roughly scales with size of the IP-OOP interface, or the cross section of the nanomagnet, such that $E^{\mathrm{dmi}} \propto tw$, where w is the width of the nanomagnet

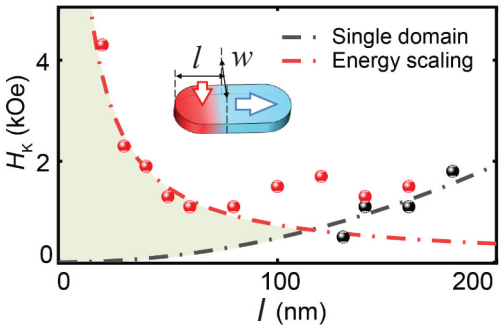

Figure 7.5.: Boundaries of the single-domain behavior (black line) and chiral-coupling (red line) as a function of the OOP magnetic anisotropy field H_k and element size l. The red and black points are determined from micromagnetic simulations. The shaded area indicates the range of parameters for which chiral coupling determines the magnetic configuration.

and t is the thickness of the Co layer. The energy to reverse one of the magnetic regions on the other hand scales with its volume ($E^{ip/oop} \propto twl$), where l is the length of the nanomagnet perpendicular to the IP-OOP boundary. The ratio $E^{dmi}/E^{ip/oop} \propto 1/l$ shows how the chiral coupling works better as the device size is scaled down. Although this suggest that for vanishing $E^{ip/oop}$ the length of the region can be increased indefinitely, this is not the case because of the second condition that has to be met, which is that the IP and OOP regions must be single domain. This is especially true for extended antiferromagnetically coupled structures where multidomain states in a single region would break the chain of the coupling. The single domain condition can be boiled down to $l < l_{sd} \propto \sqrt{H_k}$, where l_{sd} is the critical single domain dimension and H_k is the effective uniaxial anisotropy along $\boldsymbol{y}$ or $\boldsymbol{z}$ for the IP or OOP region, respectively. In contrast

to the first condition, the single domain condition allows for larger devices dimension l for stronger magnetic anisotropies. In Fig. 7.5, we show the effect of the two conditions on the ideal size regime for the chiral coupling. The two boundaries represent the size limits set by the two conditions leaving the shaded region in which chiral coupling dominates. For the DMI in our Pt/Co layers, namely $D = -0.9\,\mathrm{mJ/m^2}$, this sets an upper limit of around 120 nm on the length of the OOP region. The symbols correspond to the boundary observed in micromagnetic simulations of these nanomagnets and match our estimations of the size limitations.

For larger devices, we observe one of two cases upon reversal of the IP region from the favored $\rightarrow \odot$ to the unfavored $\leftarrow \odot$. If the DMI is very strong compared to the anisotropy, the OOP region will reverse, however only partially at the interface, introducing a DW into the OOP region. If the OOP anisotropy cannot be overcome, the unfavored configuration will remain, leaving the interface in a metastable state. In the next section we will explore these metastable states, which can be used to design chiral DW injectors.

7.2. Chiral Domain Wall Injectors

Memory and logic devices that encode information in magnetic domains rely on the controlled injection of DWs to reach their full potential. In this project, we exploit the chiral coupling induced by the DMI between IP and OOP magnetized regions of a Pt/Co/AlO_x trilayer in combination with current-driven SOTs to control the injection of DWs into magnetic conduits. We demonstrate that the current-induced domain nucleation is strongly inhibited for magnetic configurations stabilized by the chiral coupling and promoted for those that have the opposite chirality. These configurations allow for efficient DW injection using

current densities of the order of $4{\times}10^{11}$ Am^{-2}, which are lower than those used in other SOT injection schemes. Furthermore, by setting the orientation of the in-plane magnetization using an external field, we demonstrate the use of a chiral DW injector to create a controlled sequence of alternating domains in a DW conduit structure driven by a steady stream of unipolar current pulses.

The nucleation of magnetic domains underpins magnetization reversal processes and, consequently, the functioning of most types of magnetic storage devices. DW racetrack memory and logic devices, in particular, require reliable control over domain nucleation and current-induced DW propagation in order to work efficiently [151–153]. The problem of domain nucleation was first addressed by modifying the magnetic anisotropy of the nucleation sites using altered shapes [154–156] or ion irradiation of magnetic structures [133–136, 157, 158], which favor magnetization reversal at specific locations. These methods are commonly used in field-induced domain nucleation and DW propagation studies [159–162]. Current-induced domain nucleation techniques based on the Oersted field produced by a narrow write line [163], spin-transfer torque switching using magnetic tunnel junctions [164] and using magnetization boundaries where the magnetization of the two adjacent regions are orthogonally aligned [165] have been shown to mitigate the shortcomings of field nucleation. These methods offer faster and more localized domain nucleation at the cost of higher device complexity.

A significant leap forward in magnetic writing was made with the advent of SOTs [166–170], which emerge at heavy metal/ferromagnet interfaces [20]. Ever since the pioneering demonstration of DW propagation using SOTs [19], steady advancements have led to record DW velocities [171, 172], higher reversal speed and reliability [21, 23, 173], as well as to a deeper understanding of the DW dynamics. In particular, it was found that, in asymmetric

ferromagnet/heavy metal bilayer films, the DMI plays a key role in the current-induced propagation of DWs [15, 22, 52, 174–176]. As a result of the DMI, DWs in ferromagnet/heavy metal layers with perpendicular magnetization have a chiral Néel structure, which ultimately defines the direction of the DW propagation driven by SOTs and their terminal velocity in the DW flow regime. Prior studies have shown that the chirality of DWs can be modified by tuning the strength of the DMI, magnetic anisotropy, and Zeeman interaction via external magnetic fields, which also affects the field-induced and current-induced DW depinning efficiency [137, 138]. Moreover, the DMI also favors domain nucleation at the edges of magnetic stripes and dots [21, 176–178].

In this chapter, we demonstrate a novel mechanism to control the injection of chiral DWs in perpendicularly magnetized Pt/Co/AlO_x wires, which exploits the DMI at the boundary between adjacent IP and OOP magnetic regions. Unlike previous investigations based on boundaries with orthogonal magnetization alignment, which have been employed for DW injection using SOTs [139] and spin-transfer torques [165], our method combines the SOTs with the chiral coupling between IP and OOP regions induced by the DMI [17]. This coupling is found to strongly affect the DW nucleation process. By setting the magnetization of the IP region ($\boldsymbol{M}^{\mathrm{ip}}$) relative to the magnetization of the OOP region ($\boldsymbol{M}^{\mathrm{oop}}$), we either enable or disable the nucleation and injection of domains in the OOP region, depending on the chirality of the IP-OOP magnetic configuration. Once enabled, the nucleation of a domain at these boundaries requires current densities of the order of 10^{11} Am^{-2}, which we will show is lower than for nucleation at defects or edges of magnetic stripes. Furthermore, the injection automatically disables itself after nucleation, as nucleation process changes the magnetic configuration at the boundary. This allows for further current

pulses to be applied to freely propagate the injected DWs as additional injections are prevented. Therefore, chirally coupled injectors can be used to enable or disable the generation of DWs in a DW conduit driven by a steady stream of clocking pulses.

7.2.1. Structure of Chiral Domain Wall Injectors

In Figure 7.6a, we show the basic structure of the chiral DW injector, namely a Pt/Co/AlO_x wire consisting of two regions with IP and OOP magnetization, respectively. At the IP-OOP boundary between the two regions, the magnetic configuration is determined by the interplay between the exchange interaction, magnetic anisotropy, and DMI. The effect of the DMI can be described by an effective field, $\boldsymbol{H}^{\mathrm{dmi}}$, which acts on the local magnetization direction $\boldsymbol{M}$. Considering for simplicity a one-dimensional wire elongated along $\boldsymbol{x}$, the effective DMI field is given by [12, 15]:

$$\boldsymbol{H}^{\mathrm{dmi}} = \frac{2D}{\mu_0 M_{\mathrm{s}}}\left(-\frac{dm_{\mathrm{z}}}{dx},\quad 0,\quad \frac{dm_{\mathrm{x}}}{dx}\right), \tag{7.1}$$

where D is the material-dependent DMI constant in units of Jm^{-2}, μ_0 is the vacuum permeability, M_{s} the saturation magnetization, and m_{x} and m_z are the components of the normalized magnetization vector $\boldsymbol{m} = \boldsymbol{M}/M_{\mathrm{s}}$. The sign of D determines the favored chirality of the IP-OOP boundary, namely the sense of rotation of $\boldsymbol{m}$ in the xz-plane. In Pt/Co/AlO_x, D is negative, which corresponds to a counterclockwise chirality [43]. Since $\boldsymbol{M}^{\mathrm{ip}}$ can point along $+\boldsymbol{x}$ ($\rightarrow$) or $-\boldsymbol{x}$ ($\leftarrow$) and $\boldsymbol{M}^{\mathrm{oop}}$ can point along $+\boldsymbol{z}$ ($\odot$) or $-\boldsymbol{z}$ ($\otimes$), we can identify four distinct configurations in our devices. These configurations differ in the energy density

$$E^{\mathrm{dmi}} = -\boldsymbol{M}\cdot\boldsymbol{H}^{\mathrm{dmi}} = -2D\left(-\frac{dm_{\mathrm{z}}}{dx}m_{\mathrm{x}} + \frac{dm_{\mathrm{x}}}{dx}m_{\mathrm{z}}\right) \tag{7.2}$$

integrated over the direction perpendicular to the IP-OOP boundary. The configurations $(\rightarrow\odot)^+$, illustrated in Figure 7.6a, and $(\leftarrow\otimes)^+$ have a low energy and are stabilized by the chiral coupling, which is denoted by "$^+$", whereas the $(\rightarrow\otimes)^-$ and $(\leftarrow\odot)^-$ configurations are destabilized by the chiral coupling, which is denoted by "$^-$".

Taking $D \approx -1.2\,\mathrm{mJm^{-2}}$ [17, 43], the magnitude of $\left\|\mu_0 \boldsymbol{H}^{\mathrm{dmi}}\right\|$ can be estimated by employing micromagnetic simulations to determine the profile of the magnetization across the IP-OOP boundary, as required by Equation 7.1. Using this method, we estimate an average effective field $\left\|\mu_0 \boldsymbol{H}^{\mathrm{dmi}}\right\| \approx 100\,\mathrm{mT}$ for Pt/Co/AlO_x. In the absence of external magnetic fields, $\boldsymbol{H}^{\mathrm{dmi}}$ can be strong enough to revert the unstable configurations $(\rightarrow\otimes)^-$ and $(\leftarrow\odot)^-$ back into the stable configurations $(\rightarrow\odot)^+$ or $(\leftarrow\otimes)^+$, which is generally the case in nanomagnets [17]. $(\rightarrow\otimes)^-$ and $(\leftarrow\odot)^-$ can be made metastable by increasing the dimension l perpendicular to the boundary, which in turn increases the energy barrier for magnetization reversal. For $l \gtrsim 125\,\mathrm{nm}$ in Pt/Co/AlO_x, the energy barrier is determined by the energy required to nucleate a new DW. In this work, we study the SOT-induced DW injection at IP-OOP boundaries and make use of the difference in energy between the stable and metastable configurations to enable and disable the current-induced injection.

7.2.2. Magnetic Anisotropy Characterization

The chiral domain injectors were produced using the selective oxidation technique as described in Section 7.1.1, however, instead of a Ta mask, we used a resist mask instead. The resist mask will generally be thicker than a hard mask, potentially leading to shadowing up to 20 nm during the oxidation, but can be removed without a trace after the oxidation. Using this, we fabricated a magnetic wire consisting of two regions with

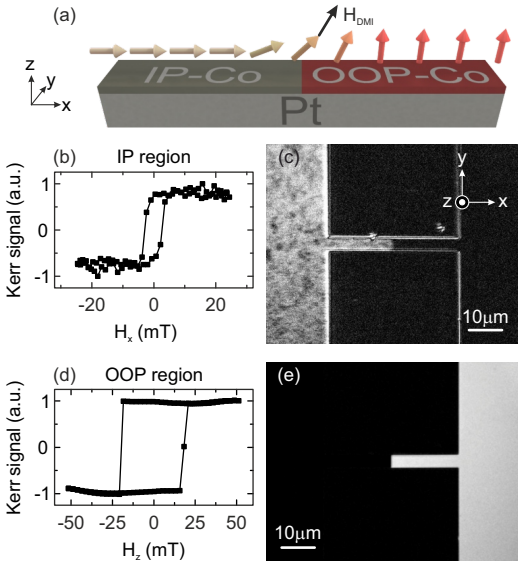

Figure 7.6.: (a) Illustration of the magnetic configuration $(\rightarrow\odot)^+$ at an IP-OOP boundary in a Pt/Co/AlO_x wire. (b) In-plane hysteresis loop and (c) corresponding differential MOKE image recorded with a MOKE microscope in longitudinal mode. (d) Out-of-plane hysteresis loop and (e) corresponding differential MOKE image recorded with a MOKE microscope in polar mode. The IP-OOP boundary is located at the border between the black and white regions. Here, the magnetization is strongly influenced by the DMI, which favors the $(\rightarrow\odot)^+$ or $(\leftarrow\otimes)^+$ configurations.

different anisotropies, as shown in Figure 7.6a where the left half is IP and the right half is OOP. These wires were then examined using a home-built wide field MOKE microscope.

The longitudinal MOKE measurements, which are sensitive to the m_x component, are shown in Figure 7.6b and 7.6c. The IP

region has uniaxial anisotropy that favors the direction parallel to the wire axis ($\pm x$), as shown by the almost square hysteresis curve in Figure 7.6b measured as a function of in-plane magnetic field H_x. The differential MOKE image (Figure 7.6c) was obtained by taking the difference between the images of the remanent states taken at zero field after saturating along $+x$ and $-x$, respectively. The contrast in the image indicates that the IP signal originates from the left half of the wire. The uneven contrast in the IP region is a result of the region breaking into domains and the low signal to noise ratio of the longitudinal MOKE. To measure the OOP component of the magnetization, m_z, we switch the microscope to the polar mode and repeat the hysteresis measurement but now with a magnetic field H_z along $\pm z$. The square hysteresis loop, shown in Figure 7.6d, implies a uniaxial OOP anisotropy and, from the differential MOKE image in Figure 7.6e, we can confirm that the signal is coming from the right half of the wire. Furthermore, this observation confirms that the IP region is fully IP, as small OOP domains would be clearly visible due to strong contrast in the polar MOKE. This demonstrates that our fabrication method succeeds in sharply defining regions of different anisotropies.

7.2.3. Asymmetric Domain Nucleation

To investigate the current-induced domain nucleation in the OOP region we used the MOKE microscope in polar mode to locate the domain nucleation sites in a 4 μm wide magnetic wire. Examples of the differential MOKE images, which show the difference between an image taken before and after nucleation attempts, are shown in Figure 7.7a and 7.7b. As can be seen, the nucleation generally occurs not only at the IP-OOP boundary but also elsewhere on the sample due to random defects in the film. We elucidate the difference between the thermally induced

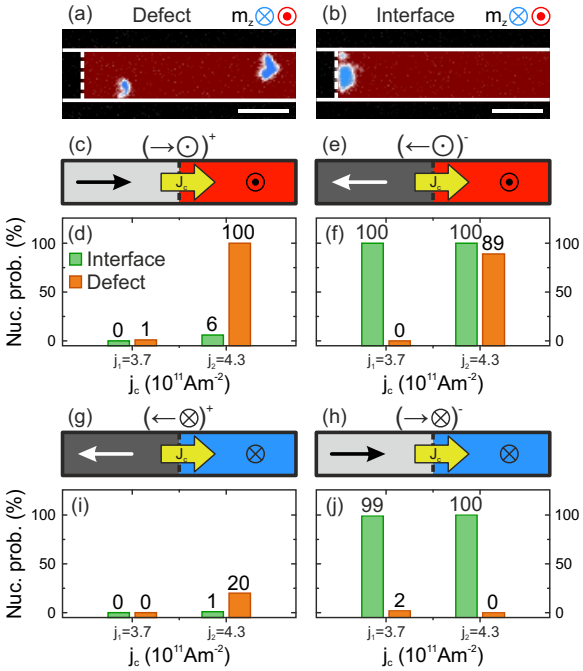

Figure 7.7.: Differential MOKE images of IP-OOP boundaries showing current-induced domain nucleation at defect sites (a) or at the boundary itself (b). The scale bars correspond to 4 μm. (c) Illustration of the magnetic configuration $(\rightarrow\odot)^+$ before the indicated current pulse j_c was applied. (d) The nucleation probability at defects (orange) and at the boundary (green) for $(\rightarrow\odot)^+$, measured for two different current densities. (e-j) Remaining configurations and associated nucleation probabilities. For $(\rightarrow\odot)^+$ and $(\leftarrow\otimes)^+$, the nucleation at the boundary is strongly suppressed, whereas for $(\leftarrow\odot)^-$ and $(\rightarrow\otimes)^-$ it is promoted. The nucleation at defects displays no dependence on the magnetic configurations.

nucleation at defects and the deterministic nucleation at the IP-OOP boundary by probing both the current dependence and field dependence of the domain nucleation.

We begin with the domain nucleation in the $(\rightarrow\odot)^+$ configuration as shown in Figure 7.7c. This configuration was set with two short, external magnetic field pulses, first $\mu_0 H_z = 100\,\mathrm{mT}$ in $+z$ direction and then $\mu_0 H_x = 50\,\mathrm{mT}$ in $+x$ direction. We then sent the current pulse in the $+x$ direction to nucleate a $\otimes$ domain, with no applied magnetic field, and compared the images before and after the current pulse. This procedure was repeated one hundred times for two current densities, namely $j_1 = 3.7 \times 10^{11}\,\mathrm{Am}^{-2}$ and $j_2 = 4.3 \times 10^{11}\,\mathrm{Am}^{-2}$. The statistics of the domain nucleation can be found in Figure 7.7d, where the green bars represent the nucleation that occurred at the boundary. For j_1, we observe almost no nucleation in the wire, neither at the IP-OOP boundary nor at defects. For the higher current density j_2, the nucleation at the boundary increases slightly to 6 % while defect-mediated nucleation increases to 100 %. So far, the data indicate that domain nucleation at the IP-OOP boundary is much less likely than nucleation at defects.

We then repeated the nucleation experiment for $(\leftarrow\odot)^-$ as illustrated in Figure 7.7e. We now saturate with H_z and $-H_x$ field pulses, while keeping the same current direction. For this configuration, unlike for $(\rightarrow\odot)^+$, the nucleation at the IP-OOP boundary was achieved even with the lower current density j_1 as shown in Figure 7.7f. The defect-mediated nucleation on the other hand, is still rare. For j_2, the boundary-mediated nucleation probability stays at 100 % while the nucleation probability at defects increases dramatically, as was observed in the $(\rightarrow\odot)^+$ configuration. The nucleation probability of the remaining two configurations $(\leftarrow\otimes)^+$ and $(\rightarrow\otimes)^-$, see Figure 7.7g and 7.7h, respectively, agrees with the asymmetry of the domain nucleation. The juxtaposition of the boundary-mediated nucleation probabil-

ities of stabilized and destabilized configurations reveals the role of the DMI in suppressing or promoting the domain nucleation in the OOP region, especially when we take into account how little the nucleation at defects changes between the different chiralities. Furthermore, the boundary-mediated nucleation consistently requires less current in the destabilized states $(\leftarrow\odot)^-$ and $(\rightarrow\otimes)^-$ compared to the nucleation at defects or at the edge of the wire.

The asymmetric domain nucleation probabilities of $(\rightarrow\odot)^+$ and $(\leftarrow\odot)^-$ can be explained by considering the action of the effective field $\boldsymbol{H}^{\mathrm{dmi}}$, and more specifically of its z-component. As stated in Equation 7.1, the z-component of $\boldsymbol{H}^{\mathrm{dmi}}$ depends on the change of m_{x} and D, which is negative for our system. Evidently, m_{x} always goes to zero in the OOP region whether it is $\odot$ or $\otimes$, so the z-component of $\boldsymbol{H}^{\mathrm{dmi}}$ is entirely determined by M^{ip}. For $(\rightarrow\odot)^+$, where $\boldsymbol{M}^{\mathrm{ip}}$ points along $+\boldsymbol{x}$, the z-components of both $\boldsymbol{H}^{\mathrm{dmi}}$ and $\boldsymbol{M}^{\mathrm{oop}}$ are positive. As a consequence, the DMI opposes the reversal and strongly inhibits domain nucleation. When $\boldsymbol{M}^{\mathrm{ip}}$ is reversed, as in the $(\leftarrow\odot)^-$ configuration, $\boldsymbol{H}^{\mathrm{dmi}}$ is also reversed and has a negative z-component opposing $\boldsymbol{M}^{\mathrm{oop}}$, which destabilizes this configuration and greatly facilitates the reversal of $\boldsymbol{M}^{\mathrm{oop}}$ by SOTs. The domain nucleation in the remaining configurations $(\leftarrow\otimes)^+$ and $(\rightarrow\otimes)^-$ follows the same logic, where $\boldsymbol{H}^{\mathrm{dmi}}$ inhibits and promotes the nucleation, respectively.

Finally, we note that the boundary-mediated nucleation in the OOP region was only observed for a current flowing along $+\boldsymbol{x}$, i.e., from the IP to the OOP region. This is a natural consequence of the DW propagation direction being parallel to the injected current in Pt/Co/AlO_x [19]. For the opposite current direction, the nucleation should occur in the IP region, but this was not observed. We ascribe the absence of nucleation in the IP region to the combination of the different magnetic anisotropy and switching geometry, which lead to different dynamics [96].

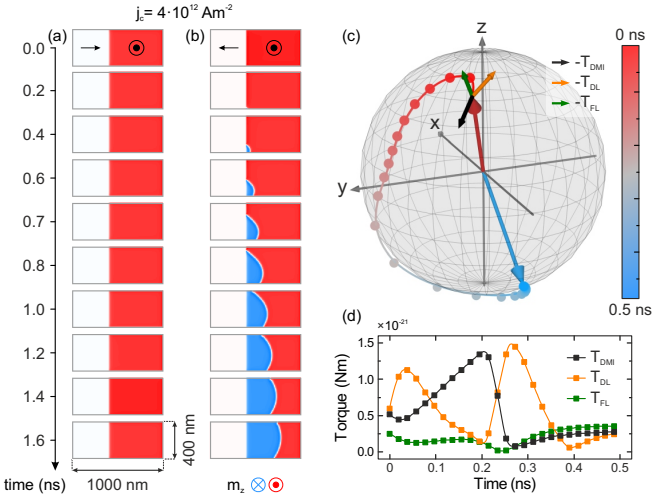

Figure 7.8.: Micromagnetic simulation of the domain nucleation at IP-OOP boundaries for two different magnetic configurations. For $j_c = 4 \times 10^{12}\,\mathrm{Am}^{-2}$, no nucleation is observed in (a) for $(\rightarrow\odot)^+$. For $(\leftarrow\odot)^-$ in (b), however, the nucleation is facilitated and a domain is injected into the wire. This leads to a full reversal of the OOP region resulting in a stable $(\leftarrow\otimes)^+$ configuration. (c) Combining the trajectory of the magnetization in (c) with the temporal evolution of the SOTs and DMI-induced torques in (d), we can deduce that the nucleation is induced by SOTs in the first 0.1 ns, but that afterwards, the main driving force for the reversal is the chiral coupling induced by the DMI. Once the z-component of the magnetization changes sign, the magnetic configuration follows the chirality imposed by the DMI and the torque exerted by the DMI quickly falls off.

7.2.4. DMI-driven Domain Nucleation

To shed more light on the asymmetric domain nucleation and the influence of the DMI on the configuration at the IP-OOP boundary, we performed micromagnetic simulations using OOMMF [179] (Figure 7.8). The simulated sample consists of a square 400 nm $\times$ 400 nm IP region, which was kept small to save computing time, and a 400 nm $\times$ 600 nm OOP region with a sharp IP-OOP boundary. The uniaxial anisotropy of the OOP (IP) region was set to $K^{\mathrm{oop}} = 625\,\mathrm{kJm^{-3}}$ ($K^{\mathrm{ip}} = 650\,\mathrm{kJm^{-3}}$). Note that, in our convention, K^{ip} is positive, reflecting the IP uniaxial anisotropy along the wire axis found in the longitudinal MOKE measurements. In order to simplify the model and reduce the parameter space, other interface-dependent quantities, such as the DMI constant $D = -1.2\,\mathrm{mJm^{-2}}$, field-like torque $T^{\mathrm{fl}} = 7\,\mathrm{mT}$ per $10^{12}\,\mathrm{A/m^2}$, and damping-like torque $T^{\mathrm{dl}} = 18\,\mathrm{mT}$ per $10^{12}\,\mathrm{A/m^2}$ [21, 22], are assumed to be constant across the IP-OOP boundary. In general, however, these parameters may vary with the oxidation profile. Similarly, we assumed the same bulk material parameters for the two regions, namely $M^{\mathrm{s}} = 900\,\mathrm{kAm^{-1}}$ and exchange coupling $A^{\mathrm{ex}} = 1.1 \times 10^{-11}\,\mathrm{Jm^{-1}}$. In Figure 7.8a and b, we show the results of the simulations of the nucleation and propagation processes for the $(\rightarrow\odot)^{+}$ and $(\leftarrow\odot)^{-}$ configurations, respectively. In both simulations, a current density of $4 \times 10^{12}\,\mathrm{Am^{-2}}$ was applied and no external magnetic field was present. In Figure 7.8a, the first frame at 0 ns represents the relaxed configuration $(\rightarrow\odot)^{+}$ with no current applied. In agreement with our measurements, we observe no switching in this case. We do however observe a small tilt of $\boldsymbol{M}^{\mathrm{oop}}$ towards the y-direction due to the SOTs, $\boldsymbol{H}^{\mathbf{dmi}}$ has a positive z-component opposing magnetization reversal. In contrast, for the $(\leftarrow\odot)^{-}$ configuration shown in Figure 7.8b, a $\otimes$ domain nucleates in the OOP region after 0.25 ns as $\boldsymbol{H}^{\mathrm{dmi}}$ now assists the magnetization reversal. The nucleated domain

quickly grows until the DW eventually spans the whole width of the wire at 1.2 ns and then continues to propagate in the direction of the current. Interestingly, the nucleation always occurs at the bottom edge of the wire for this configuration. This behavior is the result of the canting of the magnetization at the edge of the sample due to the DMI [21]. For the $(\leftarrow\odot)^-$ configuration, the initial tilt of the magnetization at the bottom edge favors its rotation in the same sense as that promoted by the SOTs, whereas at the top edge the tilt is in the opposite direction, inhibiting the effect of the SOTs. In the other metastable configuration $(\rightarrow\otimes)^-$, the canting is reversed and nucleation always starts at the top edge.

To gain deeper insight into the dynamics of the nucleation process, we analyze the trajectory of $\boldsymbol{M}^{\text{oop}}$ in a single cell of the OOMMF simulation, located at the bottom edge of the wire, 8 nm away from the IP-OOP boundary. In Figure 7.8c, we show the directions of the torques that act on $\boldsymbol{M}^{\text{oop}}$ at the start of the reversal, i.e., the damping-like torque, $\boldsymbol{T}^{\text{dl}} \propto \boldsymbol{M} \times (\boldsymbol{y} \times \boldsymbol{M})$, field-like torque, $\boldsymbol{T}^{\text{fl}} \propto \boldsymbol{y} \times \boldsymbol{M}$ and $\boldsymbol{T}^{\text{dmi}}$ exerted by the chiral coupling. In the resulting trajectory of $\boldsymbol{M}^{\text{oop}}$ in Figure 7.8c, it can be seen how the magnetization first tilts toward the z-axis and then rapidly reverses by tilting towards the y-direction. The temporal evolution of the torques, presented in Figure 7.8d, demonstrates that the initial tilt is induced by the SOTs but, once $\boldsymbol{M}^{\text{oop}}$ has moved sufficiently away from its metastable position, the effect of the DMI rapidly increases, eventually pulling the magnetization towards $-z$. At the same time, the SOTs decrease, showing that the DMI becomes the main driver of magnetization reversal, whereas the SOTs are responsible for starting the process. This is in agreement with the experimentally observed reduction of the critical current density for the nucleation at the IP-OOP boundary, which is mainly just required to start the reversal.

In our experiments, the boundary-mediated nucleation in the

4 µm wide wires shown in Figure 7.7a was generally more heterogeneous compared to the nucleation observed in the simulations. In particular, bubble-like domains formed at the boundary and merged with further application of current pulses. We ascribe this behavior to the quality of the IP-OOP boundary. If, instead of a perfectly straight boundary, we consider a boundary with a notch, a small OOP area next to the notch will be associated with a longer IP-OOP boundary, which increases the chiral coupling and, as a consequence, the nucleation efficiency in that area. For narrower lines we generally observed more homogeneous nucleation and a stronger asymmetry in the nucleation probability.

7.2.5. Driving Domain Wall Conduits

As the next step, we utilize the asymmetric domain nucleation probabilities to deterministically inject and propagate DWs into a 800 nm wide conduit (see Figure 7.9a) using a stream of current pulses of fixed amplitude and direction. We used a relatively high current density of $j_c = 7 \times 10^{11}\,\mathrm{Am}^{-2}$, which is not needed for the nucleation but to overcome the pinning for DW propagation. Since the higher j_c also increases the DW velocity, we shortened the pulse length to 35 ns in order to maintain a fine level of control over the propagation. The first differential MOKE image shown in Figure 7.9a corresponds to the initial magnetization configuration $(\leftarrow\otimes)^+$ of the DW conduit, which we set with two consecutive external magnetic field pulses, $-\mu_0 H_z = -80\,\mathrm{mT}$ followed by $-\mu_0 H_x = -80\,\mathrm{mT}$. As this is a stable configuration, we first prime the DW injection by reversing $\boldsymbol{M}^{\mathrm{ip}}$ with an external field pulse H_x. After changing the configuration to $(\rightarrow\otimes)^-$, the first current pulse injects an $\odot$ domain into the conduit, as shown in the second frame in Figure 7.9a. Every subsequent current pulse only causes the DW to propagate since the configuration

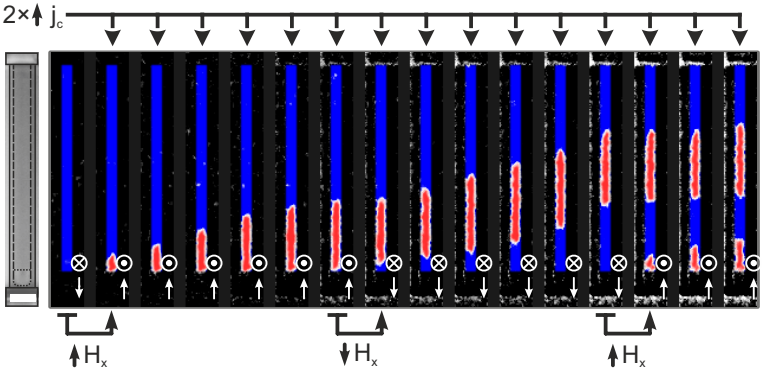

Figure 7.9.: Optical microscope image of an 800 nm wide DW conduit (left) and differential polar MOKE images of domain injection in the conduit. Starting from a saturated state, we make use of the asymmetric domain nucleation probabilities to inject a controlled sequence of alternating ⊙ and ⊗ domains. Two current pulses j_c were injected between each frame shown. The domain nucleation was enabled with a short external field pulse H_x as indicated below the frames. The scale bar corresponds to 2 μm.

was changed to $(\rightarrow\odot)^+$ after the injection, which is stable. The somewhat uneven DW velocity between the frames is caused by the pinning in Pt/Co/AlO_x. Nevertheless, the length of the injected domain can be precisely controlled and, once the desired domain size is reached, the nucleation can be once again enabled by reversing $\boldsymbol{M}^{\mathrm{ip}}$ with an external field pulse $-H_x$ to give the $(\leftarrow\odot)^-$ configuration. After the injection of another ⊗ domain of arbitrary length, we cycled back to the starting configuration $(\leftarrow\otimes)^+$. This whole process can be repeated to obtain sequences of domains with arbitrary domain lengths.

To further demonstrate the injection process in miniaturized

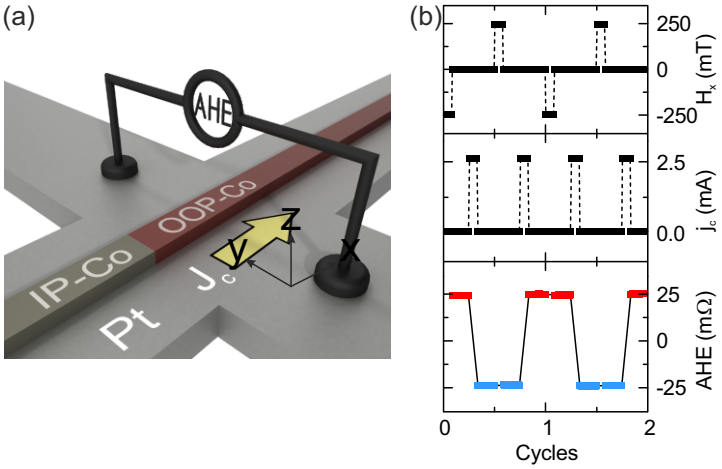

Figure 7.10.: (a) Illustration of a 100 nm wide DW conduit on top a Pt Hall cross. In this device, the injection can be measured electrically using the anomalous Hall effect. The top two plots in (b) are the field and current protocols, where each peak represents one corresponding pulse. After each current pulse, the AHE shown in the bottom plot changes sign indicating that $\boldsymbol{M}^{\text{oop}}$ reversed. The domain nucleation in the OOP region is enabled by reversing the IP region with an external field H_x between each current pulse.

structures, we fabricated DW conduits with a width of 100 nm and used the same nucleation protocol but with longer pulses, namely 100 ms, to reverse the entire length of the conduit (10 μm). Since the width is below the optical resolution of MOKE, the conduits were fabricated on a Hall cross to measure $\boldsymbol{M}^{\text{oop}}$ electrically using the AHE, as shown in Figure 7.10a. As the AHE is proportional to m_z, an inversion of the Hall signal signifies the passage of a

DW and the subsequent reversal of the magnetization of the wire. In Figure 7.10b, we demonstrate how two cycles of switching, from ⊙ to ⊗ and back again, are achieved using the asymmetric domain nucleation probabilities. Each cycle starts with a high AHE signal for the configuration $(\rightarrow\odot)^{+}$. Nucleation is then enabled by applying $-H_x$. The AHE remains positive indicating that $\boldsymbol{M}^{\mathrm{oop}}$ has not yet changed but, once a current j_c is applied, $\boldsymbol{M}^{\mathrm{oop}}$ reverses, causing a sharp drop in the AHE. To switch the magnetization back, the same procedure is followed but this time applying $+H_x$ instead of $-H_x$ to go from $(\leftarrow\otimes)^{+}$ to $(\rightarrow\otimes)^{-}$.

7.3. Summary

In conclusion, we discovered the lateral chiral coupling, which governs the properties of the magnetization at IP-OOP boundaries. These IP-OOP boundaries were created by engineering the magnetic anisotropy of Pt/Co/AlO_x using selective oxidation of the IP magnetized regions to induce perpendicular magnetic anisotropy. We found that the magnetization configuration and dynamics at the IP-OOP boundary are strongly influenced by the chiral coupling, which we can express as an average effective field $\left\|\mu_0 \boldsymbol{H}^{\mathrm{dmi}}\right\| \approx 100\,\mathrm{mT}$ across the DW, which stabilizes configurations that follow the chirality imposed by the DMI and destabilizes configurations with the opposite chirality.

In IP-OOP nanomagnets, the chiral coupling was found to induce an exchange bias strong enough to force chiral magnetization configurations even in the absence of external fields. Furthermore, we demonstrate that these nanomagnets can be daisy-chained. In such chains of alternating IP and OOP nanomagnets, the chirality at the boundaries causes the OOP regions to couple antiferromagnetically. The antiferromagnetic coupling is not limited to a one dimensional chain though. This was

demonstrated with the fabrication of an antiferromagnetically coupled square lattice of nanomagnets, where the coupling led to the spontaneous formation of antiferromagnetic domains. Lastly, we also explored the usage of curved IP-OOP boundaries in synthetic skyrmion.

Not only does the chiral coupling impact the static magnetization, it also changes the dynamic properties as was observed in the SOT-induced magnetization reversal of IP-OOP nanomagnets. Whereas in OOP nanodots the deterministic SOT-induced reversal requires a magnetic bias field, in our IP-OOP nanomagnets we achieved field-free switching. Our measurements indicate that instead of reversing the OOP region directly, the SOTs reverse the IP region, which reverses the OOP region through the chiral coupling.

We then left the size regime in which the chiral coupling dominates the magnetization configurations and investigated the usage of IP-OOP boundaries in nano/microwires. Here, we exploit the reconfigurable energy landscape induced by the IP-OOP boundary to design chiral DW injectors for the use in DW conduits. For current-induced nucleation, the consequence of $\boldsymbol{H}^{\mathrm{dmi}}$ is that switching from metastable to stable configurations is greatly facilitated, lowering the required current density, whereas switching from stable to metastable configurations is strongly inhibited. Micromagnetic simulations show that current-induced nucleation at these IP-OOP boundaries is initiated by SOTs, but that the main driving force for the magnetization reversal is $\boldsymbol{H}^{\mathrm{dmi}}$. This is in agreement with the lower critical current densities systematically observed for domain nucleation at the destabilized boundary compared to nucleation at defects or at the edges of the device.

Finally, we explore the possibility of integrating these IP-OOP boundaries into DW conduits of different widths in order to exploit the chiral coupling for DW injection. Using a simple

field and current pulse scheme, we successfully demonstrate the injection of an alternating sequence of ⊙ and ⊗ domains into conduits as narrow as 100 nm. The inherent asymmetry in the nucleation probability for different chiralities provides a means to freely configure the length of the injected domains by controlling the magnetization of the IP region. Our devices have an inherent one-dimensional design with only two contacts, making their implementation simpler than Oersted-field or magnetic tunnel junctions. The injector is also insensitive to OOP magnetic fields, making it very flexible for DW studies. If required, the need for an external IP field to set the initial state of the injector can be overcome by adopting one of the following solutions: i) switching of the IP magnetization by SOTs using an IP region patterned at an angle with respect to the current direction (two-terminal device), ii) switching of the IP magnetization by SOTs using a four-terminal geometry, and iii) using a Y-shaped injector with two IP regions with opposite magnetization and toggling the current between the two arms of the Y (three-terminal device). Compared to DW injectors based on spin-transfer torques at IP-OOP boundaries in the absence of DMI [165], the application of SOTs in combination with the chiral coupling lowers the critical current density for deterministic injection in nanoscale devices by an order of magnitude, down to 10^{11} Am^{-2} without putting an upper limit on the current density to reach higher DW velocities. Moreover, the asymmetric domain nucleation probability using chirally coupled IP-OOP boundaries gives complete control over the length of the injected domains using a stream of unipolar current pulses with a single current density and pulse length.

8. Summary and Outlook

In this thesis we set out to explore two facets of FM/oxide interfaces. One are MR and current-induced effects and the other are the magnetic anisotropies that arise at these interfaces, and how they can be used to induce lateral chiral coupling.

Crystalline MR and Current-induced Effects We developed a measurement and data analysis methodology for the characterization of the crystalline MR, SOTs and UMR. The first step in this process was to improve the data acquisition by implementing a proper triggering scheme, which lowered jittering in digital signal processing and allowed for more precise measurements of much smaller signals. Next, we built a data analysis framework that allowed for more structured and convenient data handling and exploration. Using this framework, we wrote an all-in-one SOT extraction code based on an iterative fit. In this fit, we employed parallelized LLG-simulations and highly efficient linear equation solvers to quantify the MR and current-induced effects and magnetic anisotropies. Despite the large collection of measurements required to quantify these effects, which includes field, current and angular dependencies, the code was optimized to allow for the total iterative fit process to complete in a few minutes.

These advances in data acquisition and processing opened the door to the observation of the UMR and SOTs in epitaxial MgO(001)/Fe/oxide layers. These effects are usually associated with the presence of external spin current sources, such as a

neighboring HM layer. Instead, our measurements indicate that the spin current intrinsically produced by the Fe and its interfaces suffice to generate these effects. The strength of these effects was found to be one to two orders of magnitude smaller than in the HM/FM reference systems. However, unlike in these systems, the epitaxy in our Fe layers imprinted a crystalline anisotropy on all phenomena that we observed. By correlating the crystalline anisotropy of the SOTs and the UMR, we gained insight into the spin dynamics of the system. Furthermore, exchanging the top oxide interface from a nominally epitaxial Fe/MgO interface to a more disordered Fe/AlO_x interface was shown to have a direct impact on the crystalline anisotropy of the current-induced effects. In particular, the 4-fold symmetry in SOTs deteriorated, whereas the anisotropy of the UMR was enhanced, which indicates different interfacial contributions. This demonstrates that the crystalline anisotropy can provide us with valuable information that is difficult to extract from a single current direction.

The fact that we observe the CMR, UMR and SOTs even in the nominally symmetric MgO/Fe/MgO structure is attributed to the sensitivity of these effects to miniscule changes in the interface properties. However, this sensitivity proved problematic in conclusively determining the sign and strength of the SOTs as well as in identifying microscopic origin of the current-induced effects. To unravel the different contributions to the SOTs in single FM layers, future studies shall ensure a high level of control over the quality of the top interface in terms of morphology and oxidation. One way to do this is to grow sets of nominally identical FM layers with different levels of interfacial oxidation. Alternatively, one might perform resistivity, MR, and SOT measurements in-situ, during the oxidation process in a dedicated vacuum system. In this way, one would eliminate any change of the MR and SOTs due to unintentional variations of the bottom interface and FM

thickness.

Another path to follow is to overpower spurious effects by investigating FM single layers in which the current-induced effects are stronger. One material option would be CoFe alloys, for which our preliminary measurements indicate that the CMR is very strong. In the Fe single layers studied here and prior studies on GaAs/Fe, it was shown that through an increase in the FL SOTs the ratio between the CMR parameters b and c can change to a point where the α-dependence reverses sign. In CoFe, the ratio between the CMR parameters is skewed even more, resulting not only in a sign reversal of the CMR but also a sign reversal of the apparent angular dependence $R^{\mathrm{cmr}}_{\mathrm{L/H}}$ in the xy-plane. Additionally, any material with high spin polarization such as Heusler half metals [180] could amplify the sd-UMR response and facilitate its study.

Chiral Coupling Not only do oxide interfaces play a role in the electrical and spin transport properties, they also have an impact on the magnetic anisotropy of FMs and the DMI. We leveraged this fact in Pt/Co/AlO_x to induce and control lateral coupling between nanomagnets with IP and OOP magnetization mediated by the DMI. For this, we expanded our device fabrication tool set and combined nanolithography techniques with ex-situ oxidation to produce IP-OOP magnetization patterns in Pt/Co/AlO_x with a spatial resolution better than 50 nm. We demonstrate how the DMI at these boundaries manifests as a an exchange bias, coupling adjacent IP and OOP regions to each other. Furthermore, in arrays of coupled IP-OOP nanomagnets, the chiral coupling was shown to induce in antiferromagnetic arrangement of the nanomagnets [181].

In larger magnetic structures, such as magnetic DW conduits, the chiral coupling is not the dominant factor in determining

the magnetization direction of the magnetic components. Nevertheless, its influence is still present at the IP-OOP boundary, which we exploited to fabricate chiral DW injectors using SOTs [25]. We discovered that these IP-OOP boundaries can serve as efficient nucleation sites and that the nucleation energy barrier in these boundaries can be controlled via the chirality of the IP-OOP magnetic configuration in the boundary. Using this discovery, we demonstrated a domain injection scheme to drive DW conduits using a stream of unipolar current pulses. While for this demonstration we applied short external magnetic field pulses to control the chirality of the IP-OOP configuration, we also propose several all-electrical chiral injector designs. The realization of the all-electrical chiral injector would be an important next step to take for these devices.

The demonstration of the lateral chiral coupling and the chiral domain injector was followed by the design of DW logic devices based on chirally coupled DW conduits [18]. Unlike previous implementations of DW logic [151], this new implementation builds on the use of SOTs to propagate DWs, which in principle allows for all-electrical operation. In these devices, the antiferromagnetic coupling between OOP magnetized DW conduits through a narrow IP magnetized section was shown to function as a DW inverter. As a DW passes through this inverter, the IP component of the Néel DW reverses, which essentially flips the information contained in the DW. Basic logic functions, such as NAND and NOR, were achieved by coupling multiple IP-OOP boundaries to a single output. Since these logic gates are based on DW conduits, they can be cascaded simply by daisy-chaining the individual gates. This culminated in the demonstration of XOR and full adder gates, which lays the foundation for memory-in-logic applications.

Although the domain nucleation dynamics at IP-OOP boundaries was explored in this thesis, the mechanism behind the

transmission of DWs through inverters is still in question. First indications suggest that the straight IP-OOP boundary is not the most efficient geometry to induce the chiral coupling. Thus, a thorough investigation of the IP-OOP boundary shape on the dynamics could provide us with new techniques to engineer the energy landscape, and consequently improve the nucleation and transmission of DW through these barriers.

In Pt/Co/AlO_x , the operation of DW conduits has also shown suffer from pinning sites, which slow down the DW propagation. This problem could be solved by moving towards materials in which the DW propagation was proven to be more efficient, such as CoFeB.

To further increase the DW velocity in DW conduits we can also consider to make use of the interlayer coupling, as was done in synthetic antiferromagnetic DW conduits [171]. Here, the antiferromagnetic coupling of two stacked OOP DW eliminates the net magnetic moment of the structure and the demagnetizing field of DWs, resulting in up to five times faster DW velocities and the potential of much denser packing of domains in the conduit. The first step in combining the lateral chiral coupling with the interlayer coupling could be to stack a chirally coupled DW conduit on top of an ordinary OOP magnetized DW conduit in a structure such as Ta/Co/Pt/Co/AlO_x . To induce the IP-OOP coupling in both conduits, the ex-situ plasma oxidation by itself is not a sufficient, as it does not affect the bottom conduit. To achieve that, fabrication techniques to locally control the OOP anisotropy through the bottom interface have to be developed.

For now we have treated the DMI as a material parameter that is set at the sample fabrication stage. However, the voltage-tuning of the DMI has been demonstrated in recent years to be a powerful tool to control the DMI during the operation of the device [182]. Essentially, this would give us control over the strength of the antiferromagnetic coupling in OOP-IP-OOP inverter gates, which

allows us to enable and disable the transmission of DWs through the gate at will.

Finally, the device designs we presented in this thesis are only one of several building blocks that would make up a fully functional logic device. Thus a major next step, would be to test compatibility and combine our building blocks with established device components, such as with the magnetic tunnel junction on top of the conduit to read the information stored in the conduit.

Curriculum Vitae

Name	Trong Phuong Dao
Birth	June 17, 1989, in Sursee, Switzerland
Nationality	Swiss

Education

2015–2021	PhD studies
2008–2015	Master of Science ETH, ETH Zürich Master thesis: *Deposition of Heavy Metal / Ferromagnet Bilayers* Master project: *Orbital Magnetism in Cr_2O_3* Master project: *Optimization of Manufacturing Processes of Amorphous Metals* Industry project: *Corrosion Behavior and Mechanical Properties of Nickel-free, High-nitrogen Stainless Steels*
2003–2008	Kantonsschule Sursee
1996–2003	Primarschule Kotten / Primarschule St. Martin

Teaching experience

Lab courses

2018 "Reflexionsspektrometrie"

2018 "Kalorimetrie"

2017 "Forschungslabor"

Outreach programs

2018 "TecDay an der Kantonsschule Olten"

2018 "Studienwoche, Freies Gymnasium Zürich"

Student supervision

2018, Master thesis (Co-supervision), M. Müller, Ludwig Maximilian University Munich, "Dynamics of magnetic domain walls in ultrathin heterostructures studied by magneto-optical Kerr microscopy"

2017, Bachelor thesis, F. Bernasconi, ETH Zürich, "Investigation of anisotropic magnetoresistance's and planar Hall effect's magnetocrystalline anisotropy in epitaxially grownth in film of iron-cobalt 50/50 alloy in single layers and in bilayers with tungsten".

2016, Master project, J. Zhou, ETH Zürich, "Magnetoresistance and Spin-orbit Torques in Single-crystal and Polycrystalline Ferromagnetic Layers".

2015, Master thesis (Co-supervision), F. Gygax, ETH Zürich, "Deposition and Characterization of Epitaxial Ferromagnetic Heterostructures on GaAs(001)"

Publications

Published in peer-reviewed journals

(4) Current-driven magnetic domain-wall logic; Z. Luo, A. Hrabec, T.P. Dao, G. Sala, S. Finizio, J. Feng, S. Mayr, J. Raabe, P. Gambardella, L.J. Heyderman; Nature 579, 214–218 (2020)

(3) Chiral Domain Wall Injector Driven by Spin–orbit Torques; T.P. Dao, M. Müller, Z. Luo, M. Baumgartner,

A. Hrabec, L.J. Heyderman, P. Gambardela Nano Lett. 2019, 19, 9, 5930–5937

(2) Chirally coupled nanomagnets Z. Luo, T.P. Dao, A. Hrabec, J. Vijayakumar, A. Kleibert, M. Baumgartner, E. Kirk, J. Cui, T. Savchenko, G. Krishnaswamy, L.J. Heyderman, P. Gambardella Science 29 Mar 2019: Vol. 363, Issue 6434, pp. 1435-1439

(1) Magnetic properties and domain structure of ultrathin yttrium iron garnet/Pt bilayers J. Mendil, M. Trassin, Q. Bu, J. Schaab, M. Baumgartner, C. Murer, T.P. Dao, J. Vijayakumar, D. Bracher, C. Bouillet, C.A.F. Vaz, M. Fiebig, P. Gambardella Phys. Rev. Materials 3, 034403 – Published 8 March 2019

In preparation

(1) Magnetotransport in Epitaxial Fe Single Layers; T.P. Dao, S.F. Alvarados, P. Gambardella;

Conference Contributions

(4) SPS Meeting, Lausanne, Switzerland, 2017 *Asymmetric domain wall nucleation in DMI coupled in-plane and out-of-plane magnetic wire (Talk)*;

(3) SPS Meeting, Lugano, Switzerland, 2016 *Crystalline Magnetoresistance in epitaxial $Co_{50}Fe_{50}$ grown on GaAs[110] (Poster)*;

(2) European School of Magnetism, Cluj-Napoca, Romania, 2015 *Spin-orbit Torques in Au(x)W(1-x)/CoFe Bilayers (Poster)*

(1) CCMX Meeting, Bern, Switzerland, 2015 *Electrical and Magnetic Properties of Ultrathin Heavy Metal/Ferromagnet Bilayers (Poster)*

A. Device Fabrication

A.1. Fabrication of MgO(001)/Fe/Ox Hall bars

The first set of samples studied in this work are epitaxial single layer ferromagnets sandwiched between oxides, specifically

$$\mathrm{MgO(001)/Fe}(t^{\mathrm{fe}})/\mathrm{MgO}(t^{\mathrm{mgo}})/\mathrm{AlO_x}(t^{\mathrm{alox}}) \tag{A.1}$$

and

$$\mathrm{MgO(001)/Fe}(t^{\mathrm{fe}})/\mathrm{AlO_x}()t^{\mathrm{alox}}). \tag{A.2}$$

The thickness of the Fe layers was $t^{\mathrm{fe}} = 2\,\mathrm{nm}$, the MgO thickness was $t^{\mathrm{mgo}} = 2\,\mathrm{nm}$ and the $\mathrm{AlO_x}$ thickness was $t^{\mathrm{AlOx}} = 2\,\mathrm{nm}$. Our focus with these sets of samples was to measure magneto-transport phenomena as a function of the current direction vs. crystal axes. For this purpose we need densely packed Hall Bars which rotate with respect to the crystal axes, contact pads both for visibility and facilitated microwire bonding and support structures such as labels and alignment marks. The layer by layer fabrication process is illustrated in Figure A.1 and the rest of this section will list the recipe used for the fabrication of these samples starting from an empty 1 cm MgO crystal substrate. The fabrication of these samples require a MBE setup, which we have in-house, an EBL tool, a thermal evaporator and an ion miller, which were located at the cleanroom facilities of the PSI.

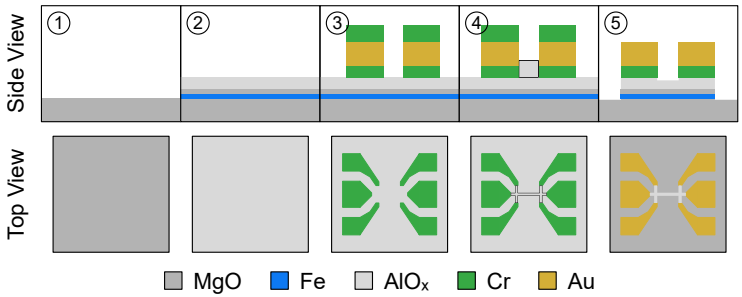

Figure A.1.: Illustration of the device fabrication of epitaxial Fe devices. (1) MgO(001) substrate. (2) Fe/MgO/AlO_x deposited by MBE. (3) Cr/Au/Cr contact pads added, where Cr layers were used on the bottom for better wetting and on top as an etch protection. (4) AlO_x etch mask added to form Hall bar. (5) Final device after etch. The illustration is not to scale.

(1) Summary and template of common steps

- [1] General cleaning
  - 10 min ultrasound sonication in Acetone at 50 °C
  - 10 min ultrasound sonication in IPA at 50 °C
  - Dry with nitrogen spray gun
  - Heat to 100 °C for 5 min on a hotplate
- [2] Spin coat (resist) at (rotation) and bake for (time) at (temperature)
  - Place in spin coater and clean surface from debris with nitrogen spray gun
  - Apply one three droplets of (resist) in the center of the substrate
  - Spin at (rotation) without a lid

  - Clean the back of the substrate with acetone soaked cleanroom tissue to prevent sticking and retain a flat surface
  - Bake resist at (temperature) for (time) on a hot-plate
- [3] Lift-off
  - Place sample in Acetone overnight
  - Heat acetone to 50 °C and leave sample in it for 10 min
  - Ultrasound sonication in hot Acetone for 10 min
  - Place sample into a new hot Acetone bath and continue sonication for 5 min
  - Ultrasound sonication in hot IPA for 10 min
  - Dry with nitrogen spray gun

(2) Growth of epitaxial Fe layer and oxide cap using MBE

- Fe 2 nm deposition
  - Clean sample[1]
  - Mount into MBE system
  - Bake in UHV at 600 °C
  - Measure Fe deposition rate ($\approx 1\,\text{Å}\,\text{min}^{-1}$) with quartz balance where the sample will positioned for the deposition
  - Swap sample and quartz and deposit 1 nm presuming constant deposition rate
  - Swap and measure the deposition rate again
  - Deposit remaining 1 nm and compensate change of deposition rate between first and second measurement.
- Optional MgO 2 nm deposition
  - Deposit a few monolayers of Mg in UHV and stop deposition with a shutter
  - Introduce 10^{-7} mbar of oxygen gas to the deposition chamber and oxidize the already deposited Mg over 1 min
  - Open shutter and finish reactive deposition of 2 nm MgO
- Initial AlO_x growth (Only done if no MgO was deposited)
  - Deposit a few monolayers of Al in UHV and stop deposition with a shutter
  - Introduce 10^{-7} mbar of oxygen gas to the deposition chamber and oxidize the already deposited Al over 1 min

- AlO_x deposition on Fe/Ox as protection layer
  - Introduce 10^{-7} mbar of oxygen gas to the deposition chamber
  - Deposit 5 nm of AlO_x reactively

(3) Fabrication of alignment markers, labels and contact pads

- Spin coating MMA/PMMA double layer resist with total thickness of ≈ 300 nm
  - Clean sample[1]
  - Spin coat 4 % MMA at 1500 rpm and bake for 5 min at 180 °C[2]
  - Spin coat 1 % 950 k PMMA at 1500 rpm and bake for 5 min at 180 °C[2]
- EBL
  - Clean the back of the substrate with acetone soaked cleanroom tissue
  - Mount sample with two metal clamps and make sure they go through the resist and touch the conducting layer
  - Manually align exposure using the corners of the sample
  - Expose a dose of 700 μC/cm^2 using 100 nA at 100 keV
  - Develop in 3:7 water/IPA solution for 30 s, constantly moving the sample
  - Stop development in IPA
  - Dry with nitrogen spray gun
- Thermal deposition of Cr/Au/Cr
  - Mount sample and pump down to base pressure (≈ 10^{-6} mbar)
  - Deposit Cr 5 nm as a seed layer
  - Deposit Au 50 nm
  - Deposit Cr 20 nm to protect from etching

- Lift-off[3]

(4) Fabrication of Hall bars

- Spin coating MMA/PMMA double layer resist with total thickness of ≈ 100 nm
  - Clean sample[1]
  - Spin coat 4 % MMA at 4000 rpm and bake for 5 min at 180 °C[2]
  - Spin coat 1 % 950 k PMMA at 4000 rpm and bake for 5 min at 180 °C[2]
- EBL
  - Clean the back of the substrate with acetone soaked cleanroom tissue
  - Mount sample with two metal clamps and make sure they go through the resist and touch the conducting layer
  - Automatically align exposure with alignment markers
  - Expose dose of 700 $\mu C/cm^2$ using 1 nA at 100 keV
  - Develop in 3:7 water/IPA solution for 30 s, constantly moving the sample
  - Stop development in IPA
  - Dry with nitrogen spray gun
- Thermal evaporation of AlO_x etch mask
  - Mount sample and wait until the pressure reaches 10^{-5} mbar
  - Deposit 1 nm Al with low power/rate in moderate vacuum to reactively oxidize
  - Vent system to expose the deposited Al to more oxygen

  - Repeat deposition and venting until a total of $\approx 10\,\text{nm}$ grown
- Lift-off[3]
- Ar^+ ion milling
  - Etch for 30 s at an angle of incidence of 30° while rotating at 15 rpm
  - Check resistance of the sample with a voltmeter from corner to corner
  - If sample still conducts, continue etching in 10 s steps

A.2. Fabrication of Pt/Co/AlO$_x$ domain wall injectors

In these Pt/Co/AlO$_x$ we are aiming to control the PMA of the system by engineering the oxidation of the Co/AlO$_x$ interface. By selectively oxidizing areas we can create lateral interfaces between IP and OOP magnetized areas. To study the properties of these chirally coupled interfaces, we fabricated two types of devices. First are IP/OOP nano islands, in which the effects of the chiral coupling are strongly highlighted, and second are magnetic domain wall racetracks in which we employ the IP/OOP interfaces as domain wall injectors. While the device geometry between the two systems are very different, the fabrication process remains similar. The sputter deposition and DC plasma oxidation were conducted in our in-house setup, while the EBL tool and ion miller were situated in the cleanroom facilities at the PSI. The fabrication process is detailed below.

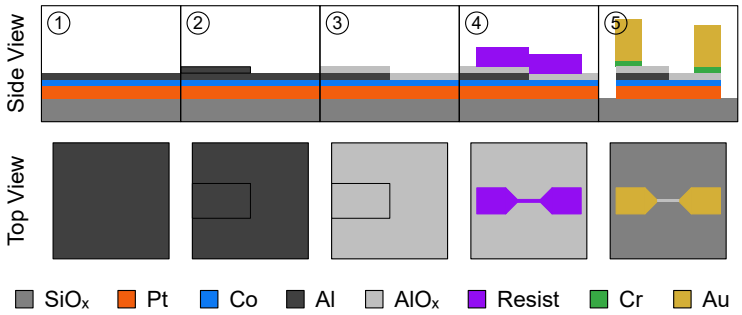

Figure A.2.: Device fabrication Pt/Co/AlO_x domain injectors. (1) As grown Pt/Co/Al with naturally oxidized Al. (2) Al oxidation mask added. (3) Ex-situ oxidation with oxygen RF-plasma to induce PMA in unmasked area. (4) Resist etch mask applied. (5) Final device after etch and addition of contact pads. The illustration is not to scale.

(1) Summary and template of common steps

- [1] General cleaning
  - 10 min ultrasound sonication in Acetone at 50 °C
  - 10 min ultrasound sonication in IPA at 50 °C
  - Dry with nitrogen spray gun
  - Heat to 100 °C for 5 min on a hotplate
- [2] Spin coat (resist) at (rotation) and bake for (time) at (temperature)
  - Place in spin coater and clean surface from debris with nitrogen spray gun
  - Apply one three droplets of (resist) in the center of the substrate
  - Spin at (rotation) without a lid

  - Clean the back of the substrate with acetone soaked cleanroom tissue to prevent sticking and retain a flat surface
  - Bake resist at (temperature) for (time) on a hotplate
- [3] Lift-off
  - Place sample in Acetone overnight
  - Heat acetone to 50 °C and leave sample in it for 10 min
  - Ultrasound sonication in hot Acetone for 10 min
  - Place sample into a new hot Acetone bath and continue sonication for 5 min
  - Ultrasound sonication in hot IPA for 10 min
  - Dry with nitrogen spray gun

(2) Growth of IP magnetized Pt/Co/AlO_x

- Sputtering
  - Clean substrate[1]
  - 30 s oxygen plasma treatment in sputtering setup
  - Deposit 5 nm of Pt
  - Deposit 1 nm of Co
  - Deposit 2 nm of Al

(3) Fabrication of alignment marks, labels and contact pads

- Spin coating MMA/PMMA double layer resist with total thickness of $\approx$ 300 nm
  - Clean sample[1]
  - Spin coat 4 % MMA at 1500 rpm and bake for 5 min at 180 °C[2]
  - Spin coat 1 % 950 k PMMA at 1500 rpm and bake for 5 min at 180 °C[2]
- EBL
  - Clean the back of the substrate with acetone soaked cleanroom tissue
  - Manually align exposure using the corners of the sample
  - Expose a dose of 700 $\mu C/cm^2$ using 100 nA at 100 keV
  - Develop in 3:7 water/IPA solution for 30 s, constantly moving the sample
  - Stop development in IPA
  - Dry with nitrogen spray gun
- Thermal deposition of Cr/Au/Cr

  - Mount sample and pump down to base pressure ($\approx 10^{-6}$ mbar)
  - Deposit Cr 5 nm as a seed layer
  - Deposit Au 50 nm
  - Deposit Cr 20 nm to protect from etching
- Lift-off[3]

(4) Patterning of racetrack, Hall cross or nano islands

- Spin coating ma-N resist with total thickness of ≈ 300 nm
  - Clean sample[1]
  - Spin coat ma-N 2403 at 4000 rpm and bake for 1 min at 90 °C[2]
- EBL
  - Clean the back of the substrate with acetone soaked cleanroom tissue
  - Automatically align exposure using alignment markers
  - Expose dose of 300 $\mu C/cm^2$ using 1 nA at 100 keV
  - Develop in ma-D 533s (1 % tetramethylammonium hydroxide in aqueous solution) for 25 s, constantly moving the sample
  - Stop development in flowing water
  - Dry with nitrogen spray gun
- Ar^+ ion milling
  - Etch for 30 s at an angle of incidence of 30° while rotating at 15 rpm
  - Check resistance of the sample with a voltmeter from corner to corner
  - If sample still conducts, continue etching in 10 s steps

(5) Patterning of nano island on Hall cross (only if Hall cross was previously patterned)

- Spin coating ma-N resist with total thickness of ≈ 300 nm
  - Clean sample[1]
  - Spin coat ma-N 2403 at 4000 rpm and bake for 1 min at 90 °C[2]
- EBL
  - Clean the back of the substrate with acetone soaked cleanroom tissue
  - Automatically align exposure using alignment markers
  - Expose a dose of 300 μC/cm^2 using 0.1 nA at 100 keV
  - Develop in ma-D 533s (1 % tetramethylammonium hydroxide in aqueous solution) for 25 s, constantly moving the sample
  - Stop development in flowing water
  - Dry with nitrogen spray gun
- Ar^+ ion milling
  - Etch for 30 s at an angle of incidence of 30° while rotating at 15 rpm

(6) Selective oxidation

- Spin coating PMMA resist with total thickness of $\approx 50\,\mathrm{nm}$
  - Clean sample[1]
  - Spin coat 1 % 950 k PMMA at 4000 rpm and bake for 5 min at 180 °C[2]
- EBL
  - Clean the back of the substrate with acetone soaked cleanroom tissue
  - Automatically align exposure using alignment markers
  - Expose a dose of $700\,\mu\mathrm{C/cm^2}$ using 0.1 nA at 100 keV
  - Develop in 3:7 water/IPA solution for 30 s, constantly moving the sample
  - Stop development in IPA
  - Dry with nitrogen spray gun
- DC plasma oxidation for 45 s
- Clean sample[1]

Bibliography

[1] Eric Masanet et al. "Recalibrating global data center energy-use estimates". en. In: *Science* 367.6481 (Feb. 2020), pp. 984–986. ISSN: 0036-8075, 1095-9203. DOI: 10.1126/science.aba3758. URL: https://science.sciencemag.org/content/367/6481/984 (visited on 12/16/2020) (cit. on pp. 21, 22).

[2] B. Dieny et al. "Opportunities and challenges for spintronics in the microelectronics industry". In: *Nature Electronics* 3.8 (Aug. 2020), pp. 446–459. DOI: 10.1038/s41928-020-0461-5 (cit. on p. 22).

[3] M. N. Baibich et al. "Giant Magnetoresistance of (001)Fe/(001)Cr Magnetic Superlattices". In: *Physical Review Letters* 61.21 (Nov. 1988), pp. 2472–2475. DOI: 10.1103/PhysRevLett.61.2472. URL: https://link.aps.org/doi/10.1103/PhysRevLett.61.2472 (visited on 11/29/2020) (cit. on pp. 23, 55).

[4] G. Binasch et al. "Enhanced magnetoresistance in layered magnetic structures with antiferromagnetic interlayer exchange". In: *Physical Review B* 39.7 (Mar. 1989), pp. 4828–4830. DOI: 10.1103/PhysRevB.39.4828. URL: https://link.aps.org/doi/10.1103/PhysRevB.39.4828 (visited on 11/29/2020) (cit. on pp. 23, 55).

[5] William Thomson. "XIX. On the electro-dynamic qualities of metals: Effects of magnetization on the electric conductivity of nickel and of iron". In: *Proceedings of the*

Royal Society of London 8.8 (Dec. 1857), pp. 546–550. DOI: 10.1098/rspl.1856.0144 (cit. on pp. 23, 28, 48, 73, 104).

[6] E.H. Hall. "XVIII. On the "Rotational Coefficient" in nickel and cobalt". In: *The London, Edinburgh, and Dublin Philosophical Magazine and Journal of Science* 12.74 (Sept. 1881), pp. 157–172. DOI: 10.1080/14786448108627086 (cit. on pp. 23, 28).

[7] P. F. Carcia, A. D. Meinhaldt, and A. Suna. "Perpendicular magnetic anisotropy in Pd/Co thin film layered structures". In: *Applied Physics Letters* 47.2 (July 1985), pp. 178–180. ISSN: 0003-6951. DOI: 10.1063/1.96254. URL: https://aip.scitation.org/doi/10.1063/1.96254 (visited on 12/22/2020) (cit. on p. 24).

[8] S. Monso et al. "Crossover from in-plane to perpendicular anisotropy in Pt/CoFe/AlOx sandwiches as a function of Al oxidation: A very accurate control of the oxidation of tunnel barriers". In: *Applied Physics Letters* 80.22 (May 2002), pp. 4157–4159. ISSN: 0003-6951. DOI: 10.1063/1.1483122. URL: https://aip.scitation.org/doi/abs/10.1063/1.1483122 (visited on 12/22/2020) (cit. on p. 24).

[9] I. Dzyaloshinsky. "A thermodynamic theory of "weak" ferromagnetism of antiferromagnetics". In: *Journal of Physics and Chemistry of Solids* 4.4 (Jan. 1958), pp. 241–255. DOI: 10.1016/0022-3697(58)90076-3 (cit. on pp. 26, 131).

[10] Tôru Moriya. "Anisotropic Superexchange Interaction and Weak Ferromagnetism". In: *Physical Review* 120.1 (Oct. 1960), pp. 91–98. DOI: 10.1103/physrev.120.91 (cit. on pp. 26, 131).

[11] M. Bode et al. "Chiral magnetic order at surfaces driven by inversion asymmetry". In: *Nature* 447.7141 (May 2007),

pp. 190–193. DOI: 10.1038/nature05802 (cit. on pp. 26, 42, 131).

[12] S. Rohart and A. Thiaville. "Skyrmion confinement in ultrathin film nanostructures in the presence of Dzyaloshinskii-Moriya interaction". In: *Physical Review B* 88.18 (Nov. 2013), p. 184422. DOI: 10.1103/physrevb.88.184422 (cit. on pp. 26, 131, 143).

[13] Stefan Heinze et al. "Spontaneous atomic-scale magnetic skyrmion lattice in two dimensions". In: *Nature Physics* 7.9 (July 2011), pp. 713–718. DOI: 10.1038/nphys2045 (cit. on pp. 26, 131).

[14] M. Heide, G. Bihlmayer, and S. Blügel. "Dzyaloshinskii-Moriya interaction accounting for the orientation of magnetic domains in ultrathin films: Fe/W(110)". In: *Physical Review B* 78.14 (Oct. 2008), p. 140403. DOI: 10.1103/PhysRevB.78.140403. URL: https://link.aps.org/doi/10.1103/PhysRevB.78.140403 (visited on 12/15/2020) (cit. on pp. 26, 42, 131).

[15] André Thiaville et al. "Dynamics of Dzyaloshinskii domain walls in ultrathin magnetic films". In: *EPL (Europhysics Letters)* 100.5 (Dec. 2012), p. 57002. DOI: 10.1209/0295-5075/100/57002 (cit. on pp. 26, 42, 131, 142, 143).

[16] J.-P. Tetienne et al. "The nature of domain walls in ultrathin ferromagnets revealed by scanning nanomagnetometry". In: *Nature Communications* 6.1 (Apr. 2015). DOI: 10.1038/ncomms7733 (cit. on pp. 26, 131).

[17] Zhaochu Luo et al. "Chirally coupled nanomagnets". In: *Science* 363.6434 (Mar. 2019), pp. 1435–1439. DOI: 10.1126/science.aau7913 (cit. on pp. 27, 36, 130, 142, 144).

[18] Zhaochu Luo et al. “Current-driven magnetic domain-wall logic”. In: *Nature* 579.7798 (Mar. 2020), pp. 214–218. DOI: 10.1038/s41586-020-2061-y (cit. on pp. 27, 162).

[19] Ioan Mihai Miron et al. “Fast current-induced domain-wall motion controlled by the Rashba effect”. In: *Nature Materials* 10.6 (May 2011), pp. 419–423. DOI: 10.1038/nmat3020 (cit. on pp. 27, 141, 149).

[20] A. Manchon et al. “Current-induced spin-orbit torques in ferromagnetic and antiferromagnetic systems”. In: *Reviews of Modern Physics* 91.3 (Sept. 2019), p. 035004. DOI: 10.1103/RevModPhys.91.035004. URL: https://link.aps.org/doi/10.1103/RevModPhys.91.035004 (visited on 08/27/2020) (cit. on pp. 27, 43, 44, 56, 57, 104, 119, 141).

[21] Manuel Baumgartner et al. “Spatially and time-resolved magnetization dynamics driven by spin–orbit torques”. In: *Nature Nanotechnology* 12.10 (Aug. 2017), pp. 980–986. DOI: 10.1038/nnano.2017.151 (cit. on pp. 27, 46, 138, 141, 142, 151, 152).

[22] Manuel Baumgartner and Pietro Gambardella. “Asymmetric velocity and tilt angle of domain walls induced by spin-orbit torques”. In: *Applied Physics Letters* 113.24 (Dec. 2018), p. 242402. DOI: 10.1063/1.5063456 (cit. on pp. 27, 142, 151).

[23] Kevin Garello et al. “Ultrafast magnetization switching by spin-orbit torques”. In: *Applied Physics Letters* 105.21 (Nov. 2014), p. 212402. DOI: 10.1063/1.4902443 (cit. on pp. 27, 141).

[24] Stuart Parkin and See-Hun Yang. “Memory on the racetrack”. In: *Nature Nanotechnology* 10.3 (Mar. 2015), pp. 195–198. DOI: 10.1038/nnano.2015.41 (cit. on pp. 27, 130).

[25] T. Phuong Dao et al. “Chiral Domain Wall Injector Driven by Spin–Orbit Torques”. In: *Nano Letters* 19.9 (Sept. 2019), pp. 5930–5937. ISSN: 1530-6984. DOI: 10.1021/acs.nanolett.9b01504. URL: https://doi.org/10.1021/acs.nanolett.9b01504 (visited on 12/15/2020) (cit. on pp. 27, 31, 130, 162).

[26] Jairo Sinova et al. “Spin Hall effects”. In: *Reviews of Modern Physics* 87.4 (Oct. 2015), pp. 1213–1260. DOI: 10.1103/RevModPhys.87.1213. URL: https://link.aps.org/doi/10.1103/RevModPhys.87.1213 (visited on 11/23/2020) (cit. on pp. 28, 56, 57, 122).

[27] Can Onur Avci et al. “Unidirectional spin Hall magnetoresistance in ferromagnet/normal metal bilayers”. In: *Nature Physics* 11.7 (2015), pp. 570–575. DOI: 10.1038/nphys3356 (cit. on pp. 28, 64, 70, 104, 105, 117, 119, 120).

[28] H. Nakayama et al. “Spin Hall Magnetoresistance Induced by a Nonequilibrium Proximity Effect”. In: *Physical Review Letters* 110.20 (May 2013), p. 206601. DOI: 10.1103/PhysRevLett.110.206601 (cit. on pp. 28, 60, 73, 104).

[29] Y. M. Lu et al. “Hybrid magnetoresistance in the proximity of a ferromagnet”. In: *Physical Review B* 87.22 (June 2013), p. 220409. DOI: 10.1103/PhysRevB.87.220409. URL: https://link.aps.org/doi/10.1103/PhysRevB.87.220409 (visited on 12/23/2020) (cit. on p. 29).

[30] A. Kobs et al. “Anisotropic Interface Magnetoresistance in Pt/Co/Pt Sandwiches”. In: *Physical Review Letters* 106.21 (May 2011), p. 217207. DOI: 10.1103/PhysRevLett.106.217207. (Visited on 07/06/2020) (cit. on pp. 29, 73).

[31] Steven S.-L. Zhang, Giovanni Vignale, and Shufeng Zhang. “Anisotropic magnetoresistance driven by surface spin-orbit scattering”. In: *Physical Review B* 92.2 (July 2015),

p. 024412. DOI: 10.1103/PhysRevB.92.024412. (Visited on 07/06/2020) (cit. on p. 29).

[32] L. K. Zou et al. "Tunable angular-dependent magnetoresistance correlations in magnetic films and their implications for spin Hall magnetoresistance analysis". In: *Physical Review B* 93.7 (Feb. 2016), p. 075309. DOI: 10.1103/PhysRevB.93.075309. (Visited on 07/05/2020) (cit. on pp. 29, 105).

[33] M. W. Jia et al. "Anomalous Hall magnetoresistance in single-crystal Fe(001) films". In: *New Journal of Physics* 22.4 (Apr. 2020), p. 043014. ISSN: 1367-2630. DOI: 10.1088/1367-2630/ab7d7b. (Visited on 07/05/2020) (cit. on pp. 29, 105).

[34] Yumeng Yang et al. "Anomalous Hall magnetoresistance in a ferromagnet". In: *Nature Communications* 9.1 (June 2018). DOI: 10.1038/s41467-018-04712-9 (cit. on pp. 29, 61, 73).

[35] Woosik Gil et al. "Magnetoresistance anisotropy of polycrystalline cobalt films: Geometrical-size and domain effects". In: *Physical Review B* 72.13 (Oct. 2005), p. 134401. DOI: 10.1103/PhysRevB.72.134401. (Visited on 07/09/2020) (cit. on pp. 29, 73, 105).

[36] A. Philippi-Kobs et al. "Impact of Symmetry on Anisotropic Magnetoresistance in Textured Ferromagnetic Thin Films". In: *Physical Review Letters* 123.13 (Sept. 2019), p. 137201. DOI: 10.1103/PhysRevLett.123.137201. (Visited on 07/05/2020) (cit. on pp. 29, 51, 52, 73, 104, 105).

[37] W. Döring. "Die Abhängigkeit des Widerstandes von Nickelkristallen von der Richtung der spontanen Magnetisierung". In: *Annalen der Physik* 424.3 (1938), pp. 259–276. ISSN: 1521-3889. DOI: 10.1002/andp.19384240306. (Visited on 07/10/2020) (cit. on pp. 29, 51, 52, 104).

[38] Alex Hubert and Rudolf Schäfer. *Magnetic domains: the analysis of magnetic microstructures*. Springer Science & Business Media, 2008 (cit. on pp. 34, 36, 38, 39, 41, 42, 44, 91).

[39] C. Eyrich et al. "Exchange stiffness in thin film Co alloys". In: *Journal of Applied Physics* 111.7 (Apr. 2012), p. 07C919. DOI: 10.1063/1.3679433 (cit. on p. 34).

[40] Tôru Moriya. "Anisotropic Superexchange Interaction and Weak Ferromagnetism". In: *Physical Review* 120.1 (Oct. 1960), pp. 91–98. DOI: 10.1103/physrev.120.91 (cit. on p. 35).

[41] Priyamvada Jadaun, Leonard F. Register, and Sanjay K. Banerjee. "The microscopic origin of DMI in magnetic bilayers and prediction of giant DMI in new bilayers". In: *npj Computational Materials* 6.1 (July 2020). DOI: 10.1038/s41524-020-00351-1 (cit. on p. 35).

[42] A. N. Bogdanov and U. K. Rößler. "Chiral Symmetry Breaking in Magnetic Thin Films and Multilayers". In: *Physical Review Letters* 87.3 (June 2001), p. 037203. DOI: 10.1103/PhysRevLett.87.037203. URL: https://link.aps.org/doi/10.1103/PhysRevLett.87.037203 (visited on 11/13/2020) (cit. on p. 36).

[43] Mohamed Belmeguenai et al. "Interfacial Dzyaloshinskii-Moriya interaction in perpendicularly magnetized Pt/Co/AlO_x ultrathin films measured by Brillouin light spectroscopy". In: *Physical Review B* 91.18 (May 2015). DOI: 10.1103/physrevb.91.180405 (cit. on pp. 36, 143, 144).

[44] Yongsup Park, Eric E. Fullerton, and S. D. Bader. "Growth-induced uniaxial in-plane magnetic anisotropy for ultrathin Fe deposited on MgO(001) by oblique-incidence molecular beam epitaxy". In: *Applied Physics Letters* 66.16

(Apr. 1995), pp. 2140–2142. ISSN: 0003-6951. DOI: 10.1063/1.113929. (Visited on 07/06/2020) (cit. on pp. 38, 109).

[45] O. Durand et al. "Origin of the uniaxial magnetic anisotropy in Fe films grown by molecular beam epitaxy". In: *Journal of Magnetism and Magnetic Materials* 145.1 (Mar. 1995), pp. 111–117. ISSN: 0304-8853. DOI: 10.1016/0304-8853(94)01308-X. URL: http://www.sciencedirect.com/science/article/pii/030488539401308X (visited on 07/06/2020) (cit. on pp. 38, 109).

[46] J. H Wolfe et al. "Roughness induced in plane uniaxial anisotropy in ultrathin Fe films". In: *Journal of Magnetism and Magnetic Materials* 232.1 (June 2001), pp. 36–45. ISSN: 0304-8853. DOI: 10.1016/S0304-8853(01)00016-6. URL: http://www.sciencedirect.com/science/article/pii/S0304885301000166 (visited on 07/06/2020) (cit. on pp. 38, 109, 110).

[47] Qing-feng Zhan et al. "Surface morphology and magnetic anisotropy of Fe/MgO(001) films deposited at oblique incidence". In: *Applied Physics Letters* 94.4 (Jan. 2009), p. 042504. ISSN: 0003-6951. DOI: 10.1063/1.3075847. (Visited on 07/06/2020) (cit. on pp. 38, 109).

[48] C. D. Graham. "Magnetocrystalline Anisotropy Constants of Iron at Room Temperature and Below". In: *Physical Review* 112.4 (Nov. 1958), pp. 1117–1120. DOI: 10.1103/PhysRev.112.1117. URL: https://link.aps.org/doi/10.1103/PhysRev.112.1117 (visited on 12/30/2020) (cit. on p. 39).

[49] A. Manchon et al. "Analysis of oxygen induced anisotropy crossover in Pt/Co/MOx trilayers". In: *Journal of Applied Physics* 104.4 (Aug. 2008), p. 043914. DOI: 10.1063/1.2969711 (cit. on p. 40).

[50] M. D. DeJong and K. L. Livesey. “Analytic theory for the switch from Bloch to N\'eel domain wall in nanowires with perpendicular anisotropy”. In: *Physical Review B* 92.21 (Dec. 2015), p. 214420. DOI: 10.1103/PhysRevB.92.214420. URL: https://link.aps.org/doi/10.1103/PhysRevB.92.214420 (visited on 11/13/2020) (cit. on p. 41).

[51] B. Boehm et al. “Achiral tilted domain walls in perpendicularly magnetized nanowires”. In: *Physical Review B* 95.18 (May 2017), p. 180406. DOI: 10.1103/PhysRevB.95.180406. URL: https://link.aps.org/doi/10.1103/PhysRevB.95.180406 (visited on 11/13/2020) (cit. on p. 42).

[52] Satoru Emori et al. “Current-driven dynamics of chiral ferromagnetic domain walls”. In: *Nature Materials* 12.7 (June 2013), pp. 611–616. DOI: 10.1038/nmat3675 (cit. on pp. 42, 142).

[53] Angie Davidson et al. “Perspectives of electrically generated spin currents in ferromagnetic materials”. In: *Physics Letters A* 384.11 (Apr. 2020), p. 126228. DOI: 10.1016/j.physleta.2019.126228 (cit. on pp. 43, 105, 115).

[54] Kevin Garello et al. “Symmetry and magnitude of spin–orbit torques in ferromagnetic heterostructures”. In: *Nature Nanotechnology* 8.8 (July 2013), pp. 587–593. DOI: 10.1038/nnano.2013.145 (cit. on pp. 43, 70, 104, 119).

[55] I. A. Campbell and A. Fert. “Chapter 9 Transport properties of ferromagnets”. en. In: vol. 3. Elsevier, Jan. 1982, pp. 747–804. DOI: 10.1016/S1574-9304(05)80095-1. URL: http://www.sciencedirect.com/science/article/pii/S1574930405800951 (visited on 11/29/2020) (cit. on pp. 48, 54).

[56] Naoto Nagaosa et al. "Anomalous Hall effect". In: *Reviews of Modern Physics* 82.2 (May 2010), pp. 1539–1592. DOI: 10.1103/RevModPhys.82.1539. URL: https://link.aps.org/doi/10.1103/RevModPhys.82.1539 (visited on 11/29/2020) (cit. on pp. 50, 74).

[57] R. P. van Gorkom et al. "Temperature and angular dependence of the anisotropic magnetoresistance in epitaxial Fe films". In: *Physical Review B* 63.13 (Mar. 2001), p. 134432. DOI: 10.1103/PhysRevB.63.134432. (Visited on 07/09/2020) (cit. on pp. 51, 52, 104).

[58] R. Ramos, S. K. Arora, and I. V. Shvets. "Anomalous anisotropic magnetoresistance in epitaxial Fe_3O_4 thin films on MgO(001)". In: *Physical Review B* 78.21 (Dec. 2008), p. 214402. DOI: 10.1103/PhysRevB.78.214402. (Visited on 07/05/2020) (cit. on pp. 51, 52, 104).

[59] P. Li et al. "Origin of the twofold and fourfold symmetric anisotropic magnetoresistance in epitaxial Fe_3O_4 films". In: *Journal of Applied Physics* 108.9 (Nov. 2010), p. 093921. ISSN: 0021-8979. DOI: 10.1063/1.3499696. (Visited on 07/05/2020) (cit. on pp. 51, 52, 104).

[60] C. R. Hu et al. "Direct comparison of anisotropic magnetoresistance and planar Hall effect in epitaxial Fe_3O_4 thin films". In: *Physics Letters A* 376.45 (Oct. 2012), pp. 3317–3321. ISSN: 0375-9601. DOI: 10.1016/j.physleta.2012.08.009. URL: http://www.sciencedirect.com/science/article/pii/S037596011200895X (visited on 07/05/2020) (cit. on pp. 51, 52, 104).

[61] Z. Ding et al. "Three-dimensional mapping of the anisotropic magnetoresistance in Fe_3O_4 single crystal thin films". In: *Journal of Applied Physics* 113.17 (May 2013), 17B103. DOI: 10.1063/1.4796178 (cit. on pp. 51, 52, 104).

[62] X. Xiao et al. “Four-fold symmetric anisotropic magnetoresistance of single-crystalline Ni(001) film”. In: *Journal of Applied Physics* 118.20 (Nov. 2015), p. 203905. ISSN: 0021-8979. DOI: 10.1063/1.4936175. (Visited on 07/05/2020) (cit. on pp. 51, 52, 104).

[63] T. Hupfauer et al. “Emergence of spin–orbit fields in magnetotransport of quasi-two-dimensional iron on gallium arsenide”. In: *Nature Communications* 6.1 (June 2015). DOI: 10.1038/ncomms8374 (cit. on pp. 52, 76, 104, 113).

[64] J. C. Slonczewski. “Current-driven excitation of magnetic multilayers”. en. In: *Journal of Magnetism and Magnetic Materials* 159.1 (June 1996), pp. L1–L7. ISSN: 0304-8853. DOI: 10.1016/0304-8853(96)00062-5. URL: http://www.sciencedirect.com/science/article/pii/0304885396000625 (visited on 11/29/2020) (cit. on p. 55).

[65] L. Berger. “Emission of spin waves by a magnetic multilayer traversed by a current”. In: *Physical Review B* 54.13 (Oct. 1996), pp. 9353–9358. DOI: 10.1103/PhysRevB.54.9353. URL: https://link.aps.org/doi/10.1103/PhysRevB.54.9353 (visited on 11/29/2020) (cit. on p. 55).

[66] Lars Onsager. “Reciprocal Relations in Irreversible Processes. I.” In: *Physical Review* 37.4 (Feb. 1931), pp. 405–426. DOI: 10.1103/physrev.37.405 (cit. on p. 56).

[67] Genki Okano et al. “Nonreciprocal Spin Current Generation in Surface-Oxidized Copper Films”. In: *Physical Review Letters* 122.21 (May 2019), p. 217701. DOI: 10.1103/PhysRevLett.122.217701. URL: https://link.aps.org/doi/10.1103/PhysRevLett.122.217701 (visited on 08/27/2020) (cit. on pp. 57, 104, 105).

[68] I. Hajzadeh et al. “Theory of the spin Hall effect in metal oxide structures”. In: *Physical Review B* 99.9 (Mar. 2019). DOI: 10.1103/physrevb.99.094414 (cit. on pp. 57, 105).

[69] Hongyu An et al. “Spin–torque generator engineered by natural oxidation of Cu”. In: *Nature Communications* 7.1 (Oct. 2016). DOI: 10.1038/ncomms13069 (cit. on pp. 57, 105).

[70] V. P. Amin et al. “Intrinsic spin currents in ferromagnets”. In: *Physical Review B* 99.22 (June 2019), p. 220405. DOI: 10.1103/physrevb.99.220405. (Visited on 07/06/2020) (cit. on pp. 57, 58, 105, 106, 123).

[71] Wenrui Wang et al. “Anomalous spin–orbit torques in magnetic single-layer films”. In: *Nature Nanotechnology* 14.9 (July 2019), pp. 819–824. DOI: 10.1038/s41565-019-0504-0 (cit. on pp. 58, 105, 106, 115, 119).

[72] V.?P. Amin, J. Zemen, and M.?D. Stiles. “Interface-Generated Spin Currents”. In: *Physical Review Letters* 121.13 (Sept. 2018), p. 136805. DOI: 10.1103/PhysRevLett.121.136805. (Visited on 07/06/2020) (cit. on pp. 58, 59, 105).

[73] Yu A Bychkov and É I Rashba. “Properties of a 2D electron gas with lifted spectral degeneracy”. In: *JETP lett* 39.2 (1984), p. 78 (cit. on p. 59).

[74] V. M. Edelstein. “Spin polarization of conduction electrons induced by electric current in two-dimensional asymmetric electron systems”. en. In: *Solid State Communications* 73.3 (Jan. 1990), pp. 233–235. ISSN: 0038-1098. DOI: 10.1016/0038-1098(90)90963-C. URL: http://www.sciencedirect.com/science/article/pii/003810989090963C (visited on 11/30/2020) (cit. on p. 59).

[75] J. C. Rojas Sánchez et al. “Spin-to-charge conversion using Rashba coupling at the interface between non-magnetic materials”. In: *Nature Communications* 4.1 (Dec. 2013). DOI: 10.1038/ncomms3944 (cit. on p. 59).

[76] G. Zahnd et al. “Spin diffusion length and polarization of ferromagnetic metals measured by the spin-absorption technique in lateral spin valves”. In: *Physical Review B* 98.17 (Nov. 2018), p. 174414. DOI: 10.1103/PhysRevB.98.174414. URL: https://link.aps.org/doi/10.1103/PhysRevB.98.174414 (visited on 11/30/2020) (cit. on p. 63).

[77] Can Onur Avci et al. “Origins of the Unidirectional Spin Hall Magnetoresistance in Metallic Bilayers”. In: *Physical Review Letters* 121.8 (Aug. 2018), p. 087207. DOI: 10.1103/PhysRevLett.121.087207. (Visited on 07/05/2020) (cit. on pp. 65, 82, 104, 105, 117).

[78] I. V. Borisenko et al. “Relation between unidirectional spin Hall magnetoresistance and spin current-driven magnon generation”. In: *Applied Physics Letters* 113.6 (Aug. 2018), p. 062403. DOI: 10.1063/1.5044737 (cit. on p. 65).

[79] B. Raquet et al. “Electron-magnon scattering and magnetic resistivity in $3d$ ferromagnets”. In: *Physical Review B* 66.2 (July 2002), p. 024433. DOI: 10.1103/PhysRevB.66.024433. URL: https://link.aps.org/doi/10.1103/PhysRevB.66.024433 (visited on 12/29/2020) (cit. on p. 65).

[80] Can Onur Avci et al. “Interplay of spin-orbit torque and thermoelectric effects in ferromagnet/normal-metal bilayers”. In: *Physical Review B* 90.22 (Dec. 2014), p. 224427. DOI: 10.1103/PhysRevB.90.224427. (Visited on 07/09/2020) (cit. on pp. 70, 115).

[81] Masamitsu Hayashi et al. “Quantitative characterization of the spin-orbit torque using harmonic Hall voltage measurements”. In: *Physical Review B* 89.14 (Apr. 2014), p. 144425. DOI: 10.1103/PhysRevB.89.144425. (Visited on 07/09/2020) (cit. on p. 70).

[82] Hans Christoph Siegmann Joachim Stöhr. *Magnetism*. Springer-Verlag GmbH, Sept. 15, 2006. ISBN: 3540302824 (cit. on p. 88).

[83] A. Locatelli and E. Bauer. “Recent advances in chemical and magnetic imaging of surfaces and interfaces by XPEEM”. en. In: *Journal of Physics: Condensed Matter* 20.9 (Feb. 2008), p. 093002. ISSN: 0953-8984. DOI: 10.1088/0953-8984/20/9/093002. URL: https://doi.org/10.1088/0953-8984/20/9/093002 (visited on 01/02/2021) (cit. on p. 88).

[84] P. Fischer. “X-Ray Imaging of Magnetic Structures”. In: *IEEE Transactions on Magnetics* 51.2 (Feb. 2015), pp. 1–31. ISSN: 1941-0069. DOI: 10.1109/TMAG.2014.2363054 (cit. on pp. 88, 91).

[85] U. Hartmann. “MAGNETIC FORCE MICROSCOPY”. In: *Annual Review of Materials Science* 29.1 (Aug. 1999), pp. 53–87. DOI: 10.1146/annurev.matsci.29.1.53 (cit. on p. 91).

[86] I. V. Soldatov and R. Schäfer. “Advanced MOKE magnetometry in wide-field Kerr-microscopy”. In: *Journal of Applied Physics* 122.15 (Oct. 2017), p. 153906. DOI: 10.1063/1.5003719 (cit. on p. 91).

[87] Ioan Mihai Miron et al. “Perpendicular switching of a single ferromagnetic layer induced by in-plane current injection”. In: *Nature* 476.7359 (Aug. 2011), pp. 189–193. DOI: 10.1038/nature10309 (cit. on p. 104).

[88] Junyeon Kim et al. “Layer thickness dependence of the current-induced effective field vector in Ta|CoFeB|MgO”. In: *Nature Materials* 12.3 (Dec. 2012), pp. 240–245. DOI: 10.1038/nmat3522 (cit. on pp. 104, 119).

[89] Paul M. Haney et al. “Current induced torques and interfacial spin-orbit coupling: Semiclassical modeling”. In: *Physical Review B* 87.17 (May 2013), p. 174411. DOI: 10.1103/PhysRevB.87.174411. (Visited on 07/06/2020) (cit. on pp. 104, 122, 124).

[90] Satoru Emori et al. “Current-driven dynamics of chiral ferromagnetic domain walls”. In: *Nature Materials* 12.7 (June 2013), pp. 611–616. DOI: 10.1038/nmat3675 (cit. on p. 104).

[91] H. Kurebayashi et al. “An antidamping spin–orbit torque originating from the Berry curvature”. In: *Nature Nanotechnology* 9.3 (Mar. 2014), pp. 211–217. DOI: 10.1038/nnano.2014.15 (cit. on p. 104).

[92] L. Chen et al. “Robust spin-orbit torque and spin-galvanic effect at the Fe/GaAs (001) interface at room temperature”. In: *Nature Communications* 7.1 (Dec. 2016). DOI: 10.1038/ncomms13802 (cit. on pp. 104, 119).

[93] L. Chen et al. “Electric-field control of interfacial spin–orbit fields”. In: *Nature Electronics* 1.6 (June 2018), pp. 350–355. DOI: 10.1038/s41928-018-0085-1 (cit. on p. 104).

[94] L. Liu et al. “Spin-Torque Switching with the Giant Spin Hall Effect of Tantalum”. In: *Science* 336.6081 (May 2012), pp. 555–558. DOI: 10.1126/science.1218197 (cit. on pp. 104, 120).

[95] Kevin Garello et al. "Ultrafast magnetization switching by spin-orbit torques". In: *Applied Physics Letters* 105.21 (Nov. 2014), p. 212402. DOI: 10.1063/1.4902443 (cit. on p. 104).

[96] S. Fukami et al. "A spin–orbit torque switching scheme with collinear magnetic easy axis and current configuration". In: *Nature Nanotechnology* 11.7 (Mar. 2016), pp. 621–625. DOI: 10.1038/nnano.2016.29 (cit. on pp. 104, 138, 149).

[97] Manuel Baumgartner et al. "Spatially and time-resolved magnetization dynamics driven by spin–orbit torques". In: *Nature Nanotechnology* 12.10 (Aug. 2017), pp. 980–986. DOI: 10.1038/nnano.2017.151 (cit. on p. 104).

[98] Miren Isasa et al. "Spin Hall magnetoresistance at Pt/CoFe2O4 interfaces and texture effects". In: *Applied Physics Letters* 105.14 (Oct. 2014), p. 142402. ISSN: 0003-6951. DOI: 10.1063/1.4897544. URL: https://aip.scitation.org/doi/full/10.1063/1.4897544 (visited on 08/27/2020) (cit. on p. 104).

[99] F. L. Zeng et al. "Strong current-direction dependence of anisotropic magnetoresistance in single crystalline Fe/GaAs(1 1 0) films". In: *Journal of Magnetism and Magnetic Materials* 499 (Apr. 2020), p. 166204. ISSN: 0304-8853. DOI: 10.1016/j.jmmm.2019.166204. URL: http://www.sciencedirect.com/science/article/pii/S0304885319330057 (visited on 07/05/2020) (cit. on p. 104).

[100] Steven S-L Zhang and Giovanni Vignale. "Theory of unidirectional spin Hall magnetoresistance in heavy-metal/ferromagnetic-metal bilayers". In: *Physical Review B* 94.14 (2016), p. 140411. DOI: 10.1103/physrevb.94.140411 (cit. on p. 105).

[101] Can Onur Avci et al. “A multi-state memory device based on the unidirectional spin Hall magnetoresistance”. In: *Applied Physics Letters* 110.20 (May 2017), p. 203506. ISSN: 0003-6951. DOI: 10.1063/1.4983784. URL: https://aip.scitation.org/doi/10.1063/1.4983784 (visited on 08/27/2020) (cit. on p. 105).

[102] Satoru Emori et al. “Interfacial spin-orbit torque without bulk spin-orbit coupling”. In: *Physical Review B* 93.18 (May 2016). DOI: 10.1103/physrevb.93.180402 (cit. on p. 105).

[103] Ziyan Luo et al. “Spin-Orbit Torque in a Single Ferromagnetic Layer with Large Spin-Orbit Coupling”. In: *arXiv:1905.11565 [cond-mat]* (May 2019). arXiv: 1905.11565. URL: http://arxiv.org/abs/1905.11565 (visited on 09/09/2020) (cit. on p. 105).

[104] Ziyan Luo et al. “Spin-Orbit Torque in a Single Ferromagnetic Layer Induced by Surface Spin Rotation”. In: *Physical Review Applied* 11.6 (June 2019), p. 064021. DOI: 10.1103/PhysRevApplied.11.064021. (Visited on 07/05/2020) (cit. on pp. 105, 115).

[105] Guanxiong Qu, Kohji Nakamura, and Masamitsu Hayashi. “Magnetization direction dependent spin Hall effect in 3d ferromagnets”. In: *arXiv:1901.10740* (Jan. 30, 2019). arXiv: 1901.10740 [cond-mat] (cit. on p. 105).

[106] T. T. Chen and V. A. Marsocci. “Transverse Magnetoresistivity Anisotropy Measurements and the Geometrical Size Effect in Nickel Thin Films”. In: *Journal of Applied Physics* 43.4 (Apr. 1972), pp. 1554–1558. ISSN: 0021-8979. DOI: 10.1063/1.1661360. (Visited on 07/09/2020) (cit. on p. 105).

[107] R. P. Cowburn et al. “Magnetic switching and in-plane uniaxial anisotropy in ultrathin Ag/Fe/Ag(100) epitaxial films”. In: *Journal of Applied Physics* 78.12 (Dec. 1995), pp. 7210–7219. ISSN: 0021-8979. DOI: 10.1063/1.360431. URL: https://aip.scitation.org/doi/10.1063/1.360431 (visited on 12/24/2020) (cit. on p. 109).

[108] Qing-feng Zhan et al. “Manipulation of in-plane uniaxial anisotropy in Fe/MgO(001) films by ion sputtering”. In: *Applied Physics Letters* 91.12 (Sept. 2007), p. 122510. ISSN: 0003-6951. DOI: 10.1063/1.2789396. URL: https://aip.scitation.org/doi/full/10.1063/1.2789396 (visited on 12/24/2020) (cit. on p. 109).

[109] Qing-feng Zhan et al. “Magnetic anisotropies of epitaxial Fe/MgO(001) films with varying thickness and grown under different conditions”. en. In: *New Journal of Physics* 11.6 (June 2009), p. 063003. ISSN: 1367-2630. DOI: 10.1088/1367-2630/11/6/063003. URL: https://doi.org/10.1088/1367-2630/11/6/063003 (visited on 12/24/2020) (cit. on p. 109).

[110] D. S. Eastwood et al. “In-situ grazing incidence X-ray diffraction measurements of relaxation in Fe/MgO/Fe epitaxial magnetic tunnel junctions during annealing”. In: *Journal of Magnetism and Magnetic Materials* 348 (Dec. 2013), pp. 128–131. ISSN: 0304-8853. DOI: 10.1016/j.jmmm.2013.08.018. URL: http://www.sciencedirect.com/science/article/pii/S0304885313005830 (visited on 07/09/2020) (cit. on p. 110).

[111] B. M. Lairson et al. “In situ x-ray measurements of the initial epitaxy of Fe(001) films on MgO(001)”. In: *Journal of Applied Physics* 78.7 (Oct. 1995), pp. 4449–4455. ISSN: 0021-8979. DOI: 10.1063/1.359853. (Visited on 07/09/2020) (cit. on p. 119).

[112] C. Lidig et al. "Unidirectional Spin Hall Magnetoresistance as a Tool for Probing the Interfacial Spin Polarization of Co_2MnSi". In: *Physical Review Applied* 11.4 (Apr. 2019), p. 044039. DOI: 10.1103/PhysRevApplied.11.044039. (Visited on 07/05/2020) (cit. on p. 120).

[113] Nguyen Huynh Duy Khang and Pham Nam Hai. "Giant unidirectional spin Hall magnetoresistance in topological insulator – ferromagnetic semiconductor heterostructures". In: *Journal of Applied Physics* 126.23 (Dec. 2019), p. 233903. ISSN: 0021-8979. DOI: 10.1063/1.5134728. (Visited on 07/05/2020) (cit. on p. 120).

[114] Isidoro Martinez et al. "Symmetry broken spin reorientation transition in epitaxial MgO/Fe/MgO layers with competing anisotropies". In: *Scientific Reports* 8.1 (June 2018). DOI: 10.1038/s41598-018-27720-7 (cit. on p. 121).

[115] A. Hallal et al. "Anatomy of perpendicular magnetic anisotropy in Fe/MgO magnetic tunnel junctions: First-principles insight". In: *Physical Review B* 88.18 (Nov. 2013), p. 184423. DOI: 10.1103/PhysRevB.88.184423. URL: https://link.aps.org/doi/10.1103/PhysRevB.88.184423 (visited on 12/14/2020) (cit. on p. 121).

[116] C.-H. Lambert et al. "Quantifying perpendicular magnetic anisotropy at the Fe-MgO(001) interface". In: *Applied Physics Letters* 102.12 (Mar. 2013), p. 122410. ISSN: 0003-6951. DOI: 10.1063/1.4798291. URL: https://aip.scitation.org/doi/full/10.1063/1.4798291 (visited on 12/14/2020) (cit. on p. 121).

[117] H. X. Yang et al. "First-principles investigation of the very large perpendicular magnetic anisotropy at Fe/MgO and Co/MgO interfaces". In: *Physical Review B* 84.5 (Aug. 2011), p. 054401. DOI: 10.1103/PhysRevB.84.054401. URL:

https://link.aps.org/doi/10.1103/PhysRevB.84.054401 (visited on 12/14/2020) (cit. on p. 121).

[118] B. Dieny and M. Chshiev. "Perpendicular magnetic anisotropy at transition metal/oxide interfaces and applications". In: *Reviews of Modern Physics* 89.2 (June 2017), p. 025008. DOI: 10.1103/RevModPhys.89.025008. URL: https://link.aps.org/doi/10.1103/RevModPhys.89.025008 (visited on 12/16/2020) (cit. on p. 121).

[119] Yang Lv et al. "Unidirectional spin-Hall and Rashba-Edelstein magnetoresistance in topological insulator-ferromagnet layer heterostructures". In: *Nature communications* 9.1 (2018), pp. 1–7. DOI: 10.1038/s41467-017-02491-3 (cit. on p. 122).

[120] T. Guillet et al. "Observation of Large Unidirectional Rashba Magnetoresistance in Ge(111)". In: *Physical Review Letters* 124.2 (Jan. 2020), p. 027201. DOI: 10.1103/PhysRevLett.124.027201. (Visited on 07/05/2020) (cit. on p. 122).

[121] Jianhui Zhou, Wen-Yu Shan, and Di Xiao. "Spin responses and effective Hamiltonian for the two-dimensional electron gas at the oxide interface LaAlO3/SrTiO3". In: *Physical Review B* 91.24 (June 2015), p. 241302. DOI: 10.1103/PhysRevB.91.241302. URL: https://link.aps.org/doi/10.1103/PhysRevB.91.241302 (visited on 12/26/2020) (cit. on p. 123).

[122] S. Döhrmann et al. "Anomalous Spin Dephasing in (110) GaAs Quantum Wells: Anisotropy and Intersubband Effects". In: *Physical Review Letters* 93.14 (Sept. 2004), p. 147405. DOI: 10.1103/PhysRevLett.93.147405. URL: https://link.aps.org/doi/10.1103/PhysRevLett.93.147405 (visited on 12/26/2020) (cit. on p. 123).

[123] Mahdi Jamali et al. “Spin-Orbit Torques in Co/Pd Multilayer Nanowires”. In: *Physical Review Letters* 111.24 (Dec. 2013), p. 246602. DOI: 10.1103/PhysRevLett.111.246602. URL: https://link.aps.org/doi/10.1103/PhysRevLett.111.246602 (visited on 12/26/2020) (cit. on p. 124).

[124] Serban Lepadatu. “Unified treatment of spin torques using a coupled magnetisation dynamics and three-dimensional spin current solver”. In: *Scientific Reports* 7.1 (Oct. 2017). DOI: 10.1038/s41598-017-13181-x (cit. on p. 124).

[125] V. P. Amin and M. D. Stiles. “Spin transport at interfaces with spin-orbit coupling: Phenomenology”. In: *Physical Review B* 94.10 (Sept. 2016), p. 104420. DOI: 10.1103/PhysRevB.94.104420. (Visited on 07/06/2020) (cit. on p. 124).

[126] B. Dieny et al. “Giant magnetoresistive in soft ferromagnetic multilayers”. In: *Physical Review B* 43.1 (Jan. 1991), pp. 1297–1300. DOI: 10.1103/PhysRevB.43.1297. URL: https://link.aps.org/doi/10.1103/PhysRevB.43.1297 (visited on 12/15/2020) (cit. on p. 130).

[127] S. S. P. Parkin et al. “Exchange-biased magnetic tunnel junctions and application to nonvolatile magnetic random access memory (invited)”. In: *Journal of Applied Physics* 85.8 (Apr. 1999), pp. 5828–5833. ISSN: 0021-8979. DOI: 10.1063/1.369932. URL: https://aip.scitation.org/doi/abs/10.1063/1.369932 (visited on 12/15/2020) (cit. on p. 130).

[128] J Nogués and Ivan K Schuller. “Exchange bias”. en. In: *Journal of Magnetism and Magnetic Materials* 192.2 (Feb. 1999), pp. 203–232. ISSN: 0304-8853. DOI: 10.1016/S0304-8853(98)00266-2. URL: http://www.sciencedirect.

com/science/article/pii/S0304885398002662 (visited on 12/15/2020) (cit. on p. 130).

[129] L. J. Heyderman and R. L. Stamps. "Artificial ferroic systems: novel functionality from structure, interactions and dynamics". en. In: *Journal of Physics: Condensed Matter* 25.36 (Aug. 2013), p. 363201. ISSN: 0953-8984. DOI: 10.1088/0953-8984/25/36/363201. URL: https://doi.org/10.1088%2F0953-8984%2F25%2F36%2F363201 (visited on 12/15/2020) (cit. on p. 131).

[130] A. Imre et al. "Majority Logic Gate for Magnetic Quantum-Dot Cellular Automata". en. In: *Science* 311.5758 (Jan. 2006), pp. 205–208. ISSN: 0036-8075, 1095-9203. DOI: 10.1126/science.1120506. URL: https://science.sciencemag.org/content/311/5758/205 (visited on 12/15/2020) (cit. on p. 131).

[131] R. P. Cowburn and M. E. Welland. "Room Temperature Magnetic Quantum Cellular Automata". en. In: *Science* 287.5457 (Feb. 2000), pp. 1466–1468. ISSN: 0036-8075, 1095-9203. DOI: 10.1126/science.287.5457.1466. URL: https://science.sciencemag.org/content/287/5457/1466 (visited on 12/15/2020) (cit. on p. 131).

[132] R. F. Wang et al. "Artificial 'spin ice' in a geometrically frustrated lattice of nanoscale ferromagnetic islands". In: *Nature* 439.7074 (Jan. 2006), pp. 303–306. DOI: 10.1038/nature04447 (cit. on p. 131).

[133] R. Hyndman et al. "Modification of Co/Pt multilayers by gallium irradiation—Part 1: The effect on structural and magnetic properties". In: *Journal of Applied Physics* 90.8 (Oct. 2001), pp. 3843–3849. DOI: 10.1063/1.1401803 (cit. on pp. 131, 141).

[134] P. Warin et al. “Modification of Co/Pt multilayers by gallium irradiation—Part 2: The effect of patterning using a highly focused ion beam”. In: *Journal of Applied Physics* 90.8 (Oct. 2001), pp. 3850–3855. DOI: 10.1063/1.1401794 (cit. on pp. 131, 141).

[135] T. Devolder et al. “Magnetic properties of He+-irradiated Pt/Co/Pt ultrathin films”. In: *Physical Review B* 64.6 (July 2001), p. 064415. DOI: 10.1103/physrevb.64.064415 (cit. on pp. 131, 141).

[136] R. Lavrijsen et al. “Controlled domain-wall injection in perpendicularly magnetized strips”. In: *Applied Physics Letters* 96.22 (May 2010), p. 222502. DOI: 10.1063/1.3432703 (cit. on pp. 131, 141).

[137] J. H. Franken et al. “Tunable chiral spin texture in magnetic domain-walls”. In: *Scientific Reports* 4.1 (June 2014). DOI: 10.1038/srep05248 (cit. on pp. 131, 142).

[138] P. P. J. Haazen et al. “Domain wall depinning governed by the spin Hall effect”. In: *Nature Materials* 12.4 (Feb. 2013), pp. 299–303. DOI: 10.1038/nmat3553 (cit. on pp. 131, 142).

[139] Masamitsu Hayashi et al. “Spatial control of magnetic anisotropy for current induced domain wall injection in perpendicularly magnetized CoFeB|MgO nanostructures”. In: *Applied Physics Letters* 100.19 (May 2012), p. 192411. DOI: 10.1063/1.4711016 (cit. on pp. 131, 142).

[140] M. Weisheit et al. “Electric Field-Induced Modification of Magnetism in Thin-Film Ferromagnets”. In: *Science* 315.5810 (Jan. 2007), pp. 349–351. DOI: 10.1126/science.1136629 (cit. on p. 131).

[141] T. Maruyama et al. “Large voltage-induced magnetic anisotropy change in a few atomic layers of iron”. In: *Nature Nanotechnology* 4.3 (Jan. 2009), pp. 158–161. DOI: 10.1038/nnano.2008.406 (cit. on p. 131).

[142] Fumihiro Matsukura, Yoshinori Tokura, and Hideo Ohno. “Control of magnetism by electric fields”. In: *Nature Nanotechnology* 10.3 (Mar. 2015), pp. 209–220. DOI: 10.1038/nnano.2015.22 (cit. on p. 131).

[143] Marine Schott et al. “The Skyrmion Switch: Turning Magnetic Skyrmion Bubbles on and off with an Electric Field”. In: *Nano Letters* 17.5 (Apr. 2017), pp. 3006–3012. DOI: 10.1021/acs.nanolett.7b00328 (cit. on pp. 131, 132).

[144] S. Monso et al. “Crossover from in-plane to perpendicular anisotropy in Pt/CoFe/AlOx sandwiches as a function of Al oxidation: A very accurate control of the oxidation of tunnel barriers”. In: *Applied Physics Letters* 80.22 (June 2002), pp. 4157–4159. DOI: 10.1063/1.1483122 (cit. on p. 132).

[145] B. Rodmacq et al. “Crossovers from in-plane to perpendicular anisotropy in magnetic tunnel junctions as a function of the barrier degree of oxidation”. In: *Journal of Applied Physics* 93.10 (May 2003), pp. 7513–7515. DOI: 10.1063/1.1555292 (cit. on p. 132).

[146] A. Manchon et al. “Analysis of oxygen induced anisotropy crossover in Pt/Co/MOx trilayers”. In: *Journal of Applied Physics* 104.4 (Aug. 2008), p. 043914. DOI: 10.1063/1.2969711 (cit. on p. 132).

[147] D. Lacour et al. “Magnetic properties of postoxidized Pt/Co/Al layers with perpendicular anisotropy”. In: *Ap-*

plied Physics Letters 90.19 (May 2007), p. 192506. DOI: 10.1063/1.2734378 (cit. on p. 132).

[148] B. Dieny and M. Chshiev. "Perpendicular magnetic anisotropy at transition metal/oxide interfaces and applications". In: *Reviews of Modern Physics* 89.2 (June 2017), p. 025008. DOI: 10.1103/revmodphys.89.025008 (cit. on p. 132).

[149] I. G. Rau et al. "Reaching the magnetic anisotropy limit of a 3d metal atom". In: *Science* 344.6187 (May 2014), pp. 988–992. DOI: 10.1126/science.1252841 (cit. on p. 132).

[150] E. Jué et al. "Domain wall dynamics in ultrathin Pt/Co/AlOx microstrips under large combined magnetic fields". In: *Physical Review B* 93.1 (Jan. 2016). DOI: 10.1103/physrevb.93.014403 (cit. on p. 133).

[151] Dan A Allwood et al. "Magnetic domain-wall logic". In: *Science* 309.5741 (2005), pp. 1688–1692. DOI: 10.1002/9783527628155.nanotech039 (cit. on pp. 141, 162).

[152] S. S. P. Parkin, M. Hayashi, and L. Thomas. "Magnetic Domain-Wall Racetrack Memory". In: *Science* 320.5873 (Apr. 2008), pp. 190–194. DOI: 10.1126/science.1145799 (cit. on p. 141).

[153] Oscar Alejos et al. "Efficient and controlled domain wall nucleation for magnetic shift registers". In: *Scientific reports* 7.1 (2017), p. 11909. DOI: https://doi.org/10.1038/s41598-017-12230-9 (cit. on p. 141).

[154] K. Shigeto, T. Shinjo, and T. Ono. "Injection of a magnetic domain wall into a submicron magnetic wire". In: *Applied Physics Letters* 75.18 (Nov. 1999), pp. 2815–2817. DOI: 10.1063/1.125159 (cit. on p. 141).

[155] R. P. Cowburn et al. “Domain wall injection and propagation in planar Permalloy nanowires”. In: *Journal of Applied Physics* 91.10 (2002), p. 6949. DOI: 10.1063/1.1447500 (cit. on p. 141).

[156] Judith Kimling et al. “Tuning of the nucleation field in nanowires with perpendicular magnetic anisotropy”. In: *Journal of Applied Physics* 113.16 (Apr. 2013), p. 163902. DOI: 10.1063/1.4802687 (cit. on p. 141).

[157] Yuxiang Yin et al. “Chiral magnetoresistance in Pt/Co/Pt zigzag wires”. In: *Applied Physics Letters* 110.12 (Mar. 2017), p. 122401. DOI: 10.1063/1.4979031 (cit. on p. 141).

[158] J. H. Franken, H. J. M. Swagten, and B. Koopmans. “Shift registers based on magnetic domain wall ratchets with perpendicular anisotropy”. In: *Nature Nanotechnology* 7.8 (July 2012), pp. 499–503. DOI: 10.1038/nnano.2012.111 (cit. on p. 141).

[159] O. Boulle et al. “Nonadiabatic Spin Transfer Torque in High Anisotropy Magnetic Nanowires with Narrow Domain Walls”. In: *Physical Review Letters* 101.21 (Nov. 2008), p. 096602. DOI: 10.1103/physrevlett.101.216601 (cit. on p. 141).

[160] A. Fernández-Pacheco et al. “Domain wall conduit behavior in cobalt nanowires grown by focused electron beam induced deposition”. In: *Applied Physics Letters* 94.19 (May 2009), p. 192509. DOI: 10.1063/1.3139068 (cit. on p. 141).

[161] P. Laczkowski et al. “Experimental evidences of a large extrinsic spin Hall effect in AuW alloy”. In: *Applied Physics Letters* 104.14 (Apr. 2014), p. 142403. DOI: 10.1063/1.4870835 (cit. on p. 141).

[162] Luis Serrano-Ramón et al. “Modification of domain-wall propagation in Co nanowires via Ga+ irradiation”. In: *The European Physical Journal B* 86.3 (2013), p. 97. DOI: https://doi.org/10.1140/epjb/e2013-30926-5 (cit. on p. 141).

[163] M. Hayashi et al. “Current-Controlled Magnetic Domain-Wall Nanowire Shift Register”. In: *Science* 320.5873 (Apr. 2008), pp. 209–211. DOI: 10.1126/science.1154587 (cit. on p. 141).

[164] D. Ravelosona et al. “Domain Wall Creation in Nanostructures Driven by a Spin-Polarized Current”. In: *Physical Review Letters* 96.18 (May 2006). DOI: 10.1103/physrevlett.96.186604 (cit. on p. 141).

[165] Timothy Phung et al. “Highly efficient in-line magnetic domain wall injector”. In: *Nano Letters* 15.2 (2015), pp. 835–841. DOI: 10.1021/nl503391k (cit. on pp. 141, 142, 158).

[166] Ioan Mihai Miron et al. “Perpendicular switching of a single ferromagnetic layer induced by in-plane current injection”. In: *Nature* 476.7359 (Aug. 2011), pp. 189–193. DOI: 10.1038/nature10309 (cit. on p. 141).

[167] Can Onur Avci et al. “Magnetization switching of an MgO/Co/Pt layer by in-plane current injection”. In: *Applied Physics Letters* 100.21 (May 2012), p. 212404. DOI: 10.1063/1.4719677 (cit. on p. 141).

[168] Luqiao Liu et al. “Current-Induced Switching of Perpendicularly Magnetized Magnetic Layers Using Spin Torque from the Spin Hall Effect”. In: *Physical Review Letters* 109.9 (Aug. 2012), p. 096602. DOI: 10.1103/physrevlett.109.096602 (cit. on p. 141).

[169] Kevin Garello et al. “Symmetry and magnitude of spin–orbit torques in ferromagnetic heterostructures”. In: *Nature Nanotechnology* 8.8 (July 2013), pp. 587–593. DOI: 10.1038/nnano.2013.145 (cit. on p. 141).

[170] Junyeon Kim et al. “Layer thickness dependence of the current-induced effective field vector in Ta| CoFeB| MgO”. In: *Nature materials* 12.3 (2013), p. 240 (cit. on p. 141).

[171] See-Hun Yang, Kwang-Su Ryu, and Stuart Parkin. “Domain-wall velocities of up to 750 m s-1 driven by exchange-coupling torque in synthetic antiferromagnets”. In: *Nature Nanotechnology* 10.3 (Feb. 2015), pp. 221–226. DOI: 10.1038/nnano.2014.324 (cit. on pp. 141, 163).

[172] Lucas Caretta et al. “Fast current-driven domain walls and small skyrmions in a compensated ferrimagnet”. In: *Nature Nanotechnology* 13.12 (2018), p. 1154 (cit. on p. 141).

[173] SV Aradhya. “SV Aradhya, GE Rowlands, J. Oh, DC Ralph, and RA Buhrman, Nanosecond-timescale low energy switching of in-plane magnetic tunnel junctions through dynamic Oersted-field-assisted spin Hall effect, Nano Lett. 16, 5987 (2016).” In: *Nano Letters* 16 (2016), p. 5987 (cit. on p. 141).

[174] Kwang-Su Ryu et al. “Chiral spin torque at magnetic domain walls”. In: *Nature Nanotechnology* 8.7 (June 2013), pp. 527–533. DOI: 10.1038/nnano.2013.102 (cit. on p. 142).

[175] O. Boulle et al. “Domain Wall Tilting in the Presence of the Dzyaloshinskii-Moriya Interaction in Out-of-Plane Magnetized Magnetic Nanotracks”. In: *Physical Review Letters* 111.21 (Nov. 2013), p. 217203. DOI: 10.1103/physrevlett.111.217203 (cit. on p. 142).

[176] Eduardo Martinez et al. “Current-driven dynamics of Dzyaloshinskii domain walls in the presence of in-plane fields: Full micromagnetic and one-dimensional analysis”. In: *Journal of Applied Physics* 115.21 (June 2014), p. 213909. DOI: 10.1063/1.4881778 (cit. on p. 142).

[177] N. Mikuszeit et al. “Spin-orbit torque driven chiral magnetization reversal in ultrathin nanostructures”. In: *Physical Review B* 92.14 (Oct. 2015), p. 144424. DOI: 10.1103/physrevb.92.144424 (cit. on p. 142).

[178] S. Pizzini et al. “Chirality-Induced Asymmetric Magnetic Nucleation in Pt/Co/AlOx Ultrathin Microstructures”. In: *Physical Review Letters* 113.4 (July 2014), p. 047203. DOI: 10.1103/physrevlett.113.047203 (cit. on p. 142).

[179] M. J. Donahue and D. G. Porter. *OOMMF user's guide, version 1.0*. Tech. rep. Interagency Report NISTIR 6376, 1999. DOI: 10.6028/nist.ir.6376. URL: https://math.nist.gov/oommf/oommf.html (cit. on p. 151).

[180] Y. Sakuraba et al. “Giant tunneling magnetoresistance in Co2MnSi / AlO / Co2MnSi magnetic tunnel junctions”. In: *Applied Physics Letters* 88.19 (May 2006), p. 192508. DOI: 10.1063/1.2202724 (cit. on p. 161).

[181] Zhaochu Luo et al. “Chirally coupled nanomagnets”. In: *Science* 363.6434 (Mar. 2019), pp. 1435–1439. DOI: 10.1126/science.aau7913 (cit. on p. 161).

[182] Titiksha Srivastava et al. “Large-Voltage Tuning of Dzyaloshinskii– Moriya Interactions: A Route toward Dynamic Control of Skyrmion Chirality”. In: *Nano Letters* 18.8 (June 2018), pp. 4871–4877. DOI: 10.1021/acs.nanolett.8b01502 (cit. on p. 163).